

Electronic Thesis and Dissertation Repository

9-28-2017 10:00 AM

Influence of Turbulence on the Aerodynamics of Low-Rise Buildings

Fakhruzzaman Arif, *The University of Western Ontario*

Supervisor: Kopp, Gregory A., *The University of Western Ontario*

A thesis submitted in partial fulfillment of the requirements for the Master of Engineering Science degree in Civil and Environmental Engineering

© Fakhruzzaman Arif 2017

Follow this and additional works at: <https://ir.lib.uwo.ca/etd>



Part of the [Civil and Environmental Engineering Commons](#), and the [Mechanical Engineering Commons](#)

Recommended Citation

Arif, Fakhruzzaman, "Influence of Turbulence on the Aerodynamics of Low-Rise Buildings" (2017).
Electronic Thesis and Dissertation Repository. 4910.
<https://ir.lib.uwo.ca/etd/4910>

This Dissertation/Thesis is brought to you for free and open access by Scholarship@Western. It has been accepted for inclusion in Electronic Thesis and Dissertation Repository by an authorized administrator of Scholarship@Western. For more information, please contact wlsadmin@uwo.ca.

Abstract

During extreme wind events, roofing failures may lead to damage of the whole structure. In order to alleviate the effect, surface pressure coefficients on the roofs have been extensively investigated. This research aims to determine the roof pressures acting on low-rise buildings with consideration of the effects of turbulence (terrain). Pressure measurements, as well as wind speed data, were taken at the Boundary Layer Wind Tunnel Laboratory (BLWTL) of the University of Western Ontario (UWO) to examine the influence of turbulence level (i.e., terrain condition) on the critical wind directions corresponding to the largest surface roof pressure coefficients for various upstream boundary layer conditions. In addition, plan dimensions and eave heights of the building were also varied. Generally, corner vortices play a vital role in generating larger suction pressures on the roof surface in flat terrain. Moreover, separation bubble at the leading edge of low-rise buildings is also significant to take into consideration for winds normal to the walls. Our objective is to examine these points in terms of area-averages used in design. The results indicate that corner vortices control larger area on the roof surface among all angles of attack in lower turbulence flow (i.e., flat terrain), whereas this effect is reduced in higher turbulence level (i.e., suburban terrain) for all plan shapes. In addition, the size of the corner vortices along both edges of the roof increases with building height for low-rise buildings, consistent with the new requirements in ASCE 7 – 16. It is also found that the critical wind directions depend significantly on the turbulence level and building height. The critical wind directions for the corner zones of low-rise building roofs are primarily due to oblique angles (i.e., corner vortices), while they are normal wind directions (i.e., bubble separation) for the edge, and interior zones, when the tributary areas are small. The magnitude of peak pressure coefficients, $G C_p$, depend more on the integral

length scales compared to the turbulence intensity, which may be important in some design scenarios.

Keywords

Building aerodynamics, Wind loads, Peak pressure coefficients, Critical wind directions, Low-rise buildings, Turbulence.

Acknowledgments

First and foremost, I would like to express my heartiest gratitude and sincere thanks to Dr, Gregory Alan Kopp for his extraordinary supervision, constant guidance and valuable advice during the whole research work. His generosity, patience, and support are greatly appreciated. I am also indebted to him for providing me necessary information, motivation and, encouragement, otherwise, this research could not be carried out successfully.

Thanks a lot to all my colleagues at Wind Engineering group, especially Dr. Fahad, Dr. Chieh-Hsun, Rahul, and Emilio for their kind assistance during my experiment and technical discussions. I am also grateful to Anant Gairola for helping me in MATLAB programming. I sincerely appreciate the help I received from the staff and technicians of the Boundary Layer Wind Tunnel Laboratory in my experiment.

And last but not the least, I owe everything to my loving parents Abdur Rab Mia and Jayeda Parvin for their prayers, dedication, and inspiration. Without their tremendous support, this journey would not have been possible.

Table of Contents

Abstract	i
Acknowledgments.....	iii
Table of Contents	iv
List of Tables	vi
List of Figures	vii
List of Appendices	xi
Nomenclature	xii
Chapter 1	1
1 Introduction	1
1.1 Motivation.....	2
1.2 Literature Review.....	10
1.3 Objectives	16
1.4 Overview of Thesis	16
Chapter 2.....	17
2 Experimental Setup	17
2.1 Introduction.....	17
2.2 Building Models.....	18
2.3 Terrain Simulation	23
2.4 Testing Parameters.....	28
2.5 Analysis Process	30
2.5.1 Area Averaging.....	30
2.5.2 Extreme Value Analysis	30
2.5.3 Reference Height Velocity.....	33
Chapter 3.....	34

3	Results	34
3.1	Comparisons with Previously Published Data	34
3.2	Critical Wind directions	40
3.2.1	Overall Observations	40
3.2.2	Effects of Upstream Condition on Length of Corner Vortices for Fixed Geometries	52
3.2.3	Effects of Building Height on Length of Corner Vortices.....	60
3.3	Worst (Enveloped) GCp Values	63
3.4	Discussion	69
	Chapter 4.....	71
4	Conclusions and Recommendations	71
4.1	Conclusions.....	71
4.2	Recommendations.....	72
	References.....	74
	Appendices.....	78
	Appendix A: Critical Wind Directions	78
	Appendix B: Worst GCp.....	85
	Curriculum Vitae	92

List of Tables

Table 1: Different configurations of plan dimensions and heights of the models in the experiment.....	21
Table 2: Tested wind directions.....	23
Table 3: Properties of the upstream boundary layer simulations.....	28
Table 4: Factors used in Lieblein BLUE method.	32
Table 5: Comparison of different factors between the models of Kopp and Morrison (2017) and the current experiment at model scale.....	37
Table 6: Different lengths of critical wind directions for all cases.....	55

List of Figures

Figure 1: Streamwise velocity spectra for full-scale and wind tunnel data (after Irwin, 2008).	3
Figure 2: Selected scale model of solar array in boundary layer wind tunnel (from Browne et al., 2013).	5
Figure 3: Comparison of turbulence intensity and velocity ratio between Akon and Kopp (2016) and Browne et al. (2013).	6
Figure 4: (a) Turbulence intensity; (b) mean tunnel and von Karman spectra of the streamwise velocity fluctuations (images courtesy of Banks, 2017).	7
Figure 5: Worst pressure coefficients on solar panel from 0° to 90° relative to the building. ..	8
Figure 6: (a) Mean velocity and turbulence intensity profiles; (b) measured and theoretical spectra of the streamwise velocity fluctuations (Kopp, 2014).	9
Figure 7: Schematic representation of the peak wind loads on solar panel array.	10
Figure 8: Dual conical vortices in cornering wind (from Banks and Meroney, 2001b).	13
Figure 9: Various plan shapes of the model: (a) Building 1 (B1), (b) Building 2 (B2), (c) Building 3 (B3), and (d) Building 4 (B4), where 950 pressure taps were uniformly spaced in one block and dummy blocks were attached for different configurations. Dimensions are given in mm.	19
Figure 10: Height variations of the model: (a) Height 1 (H_1), and (b) Height 2 (H_2).	20
Figure 11: Wind directions for each of the models: (a) B1, (b) B2, (c) B3, and (d) B4.	22
Figure 12: Mean velocity profiles for various upstream conditions.	24
Figure 13: Streamwise turbulence intensity profiles for different upstream conditions.	25
Figure 14: Vertical turbulence intensity profiles for different upstream conditions.	25

Figure 15: Streamwise velocity spectra at model height, H_1 .	26
Figure 16: Streamwise velocity spectra at model height, H_2 .	27
Figure 17: Photograph of the experimental setup of a model in wind tunnel.	29
Figure 18: Comparison of Mean C_p vs. distance from the leading edge, x/H_1 for Building 1 between our experiment and, Akon and Kopp (2016): (a) with barrier, and (b) no barrier. ..	35
Figure 19: Comparison of worst GC_p values for roof zones between Kopp & Morrison paper (a) 0.84 cm^2 , and the current experiment with areas of (b) 0.49 cm^2 , and (c) 2.22 cm^2 , and for distance from leading edge (d) and (e).	39
Figure 20: Size of the roof zones in ASCE 7 – 16 (2017).	41
Figure 21: Critical wind directions and different zones of 1S B1H1 and 3L B1H1 for different tributary areas.	43
Figure 22: Critical wind directions and different zones of B3H1 and B3H2 for different tributary areas in suburban terrain.	45
Figure 23: Critical wind directions for the worst GC_p as a function of tributary area for corner zones of 1S B1H1 and 3L B1H1.	47
Figure 24: Critical wind directions for the worst GC_p as a function of tributary area for edge zones of 1S B1H1 and 3L B1H1.	47
Figure 25: Critical wind directions for the worst GC_p as a function of tributary area for interior zones of 1S B1H1 and 3L B1H1.	48
Figure 26: Critical wind directions for the worst GC_p as a function of tributary area for corner zones of B1H1 and B3H1 in suburban terrain (3L).	48
Figure 27: Critical wind directions for the worst GC_p as a function of tributary area for edge zones of B1H1 and B3H1 in suburban terrain (3L).	49

Figure 28: Critical wind directions for the worst G_{Cp} as a function of tributary area for interior zones of B1H1 and B3H1 in suburban terrain (3L). 49

Figure 29: Critical wind directions for the worst G_{Cp} as a function of tributary area for corner zones of B3H1 and B3H2 in suburban terrain (3L). 50

Figure 30: Critical wind directions for the worst G_{Cp} as a function of tributary area for edge zones of B3H1 and B3H2 in suburban terrain (3L). 50

Figure 31: Critical wind directions for the worst G_{Cp} as a function of tributary area for interior zones of B3H1 and B3H2 in suburban terrain (3L). 51

Figure 32: Critical wind directions over B2H1 and B2H2 models from 0 to 90 degree. 53

Figure 33: Critical wind directions for the 3S upstream condition on Building 1 (H2). 54

Figure 34: Effect of turbulence intensity on L1 and L2 (normalized by height) for B2H2 and B3H2. 56

Figure 35: Effect of turbulence intensity on L1 and L2 (normalized by $\sqrt{\text{Area}}$) for B2H2 and B3H2. 57

Figure 36: Effect of turbulence intensity on L1 and L2 (normalized by height) for B1H2 and B4H2. 57

Figure 37: Effect of turbulence intensity on L1 and L2 (normalized by $\sqrt{\text{Area}}$) for B1H2 and B4H2. 58

Figure 38: Effect of turbulence intensity on L1 and L2 (normalized by height) for B1H1 and B2H1. 58

Figure 39: Effect of turbulence intensity on L1 and L2 (normalized by $\sqrt{\text{Area}}$) for B1H1 and B2H1. 59

Figure 40: Effect of turbulence intensity on L1 and L2 (normalized by height) for B3H1 and B4H1. 59

Figure 41: Effect of turbulence intensity on L1 and L2 (normalized by $\sqrt{\text{Area}}$) for B3H1 and B4H1.	60
Figure 42: Effect of height on critical wind directions for windward wall of all buildings. ..	61
Figure 43: Effect of height on critical wind directions for side wall of all buildings.	62
Figure 44: Critical wind directions: (a), and (b), and worst GCp: (c), and (d) over B1H1 for flat (1S), and suburban (3L) terrain, respectively.	64
Figure 45: Comparison of worst GCp over B1H1 vs. distance from the edge for 0° and 90° between flat and suburban terrain.	65
Figure 46: Comparison of worst GCp over B1H1 vs. distance from the corner for 40° and 60° between flat and suburban terrain.	66
Figure 47: Comparison of worst suction GCp over B1H1 and B2H2 models for different length scales.	67
Figure 48: Comparison of worst suction GCp over B1H1 and B2H2 models for the same terrain.	68

List of Appendices

Appendix A: Critical Wind Directions	78
Appendix B: Worst GCp.....	85

Nomenclature

Notations and symbols

A	Total tributary area
a_{ij}	Tributary area for each tap
a_i	Factor used in Lieblein analysis
b_i	Factor used in Lieblein analysis
b_n'	Parameter used in Lieblein analysis
C_p	Pressure coefficient
f	Frequency
GC_p	Peak pressure coefficient
H	Height of building
I_u	Streamwise turbulence intensity
I_w	Vertical turbulence intensity
J_e	Jensen number
L	Length of building
$L1$	Primary axis of the ellipse along the long wall
$L2$	Primary axis of the ellipse along the short wall
L_u	Longitudinal integral length scale
p	Recorded pressure
p_o	Static pressure

$S_{uu}(f)$	Spectral density function of the longitudinal component
U	Mean velocity
U_{H1}	Mean velocity at roof height H1
u_n'	Parameter used in Lieblein analysis
W	Width of building
x	Horizontal distance
y	Vertical distance
y_o	Roughness length
z	Height from ground
σ	Standard deviation

Chapter 1

1 Introduction

An investigation of the pressure coefficients on the roofs of low-rise buildings (those with Height/Width < 1) has been carried out to obtain the effects of turbulence in this study. Most of the structures built in North America for residential, industrial, and other purposes, can be classified as low-rise buildings. It is important to investigate roof pressures on these buildings, because they are usually prone to wind damage by hurricanes, typhoons, etc., as described in the study of Uematsu and Isyumov (1999). For example, Hurricane Andrew, which was the most devastating hurricane in Florida, produced insured property losses estimated at US\$17.7 billion in 1992 (Lee and Rosowsky, 2005). Various studies were performed to understand the wind pressures acting on low-rise buildings, for example, Krishna (1995), Uematsu and Isyumov (1999). According to the damage survey of Uematsu et al. (1998), most wind damage was found on the cladding of buildings, especially the roof sheathing. During a strong windstorm, when a sheathing panel has been blown away, the losses can increase significantly due to rain water intrusion, as described by IntraRisk (2002). In addition, when these failed panels fly through the air, they can damage adjacent structures. A comprehensive description of this type of damage (due to wind-borne debris) can be found in Minor (1994). Therefore, it is essential to study pressures acting on roofs or roof-mounted structures of low-rise buildings.

As will be shown in Section 1.1, the motivation of the present study is the inconsistency of terrain definitions in wind tunnel studies, and how the difference in the turbulence can impact on the aerodynamics of low-rise buildings. The previously published studies available in the literature are primarily focused on two-dimensional bluff bodies placed in uniform upstream flows, which are discussed in Section 1.2. There has been less analysis of changes in the aerodynamics of low-rise buildings for different upstream boundary layer conditions.

The aim of this study is to understand the influence of turbulence of the upstream flow to the low-rise buildings of different sizes. To obtain this goal, experiments were conducted in a boundary layer wind tunnel for several configurations with various plan dimensions. Pressure coefficients obtained from the experiment allow us to examine the effects of turbulence on the aerodynamics of low-rise buildings.

1.1 Motivation

For the purpose of investigating wind-induced pressures on structures like air-permeable multi-layer cladding systems, solar panels, etc., large model scales are often required in order to replicate the small geometric details. Different approaches are used by various wind tunnel labs when large model scales are required. Thus, understanding all of the effects of turbulence, i.e., terrain, on wind loads on buildings of different sizes is required.

Figure 1 shows a typical scenario of velocity spectra for large model-scale testing. Non-dimensional streamwise velocity spectra ($fS_{uu}(f)/V^2$) vs. frequency (fH/V) are plotted in this figure. The power spectral density, $S_{uu}(f)$, is normalized with the mean velocity, V , such that differences caused by altering the turbulence intensity are visible. The frequency, f , is normalized by the mean velocity and the roof height, H . The non-dimensional frequency, fH/V represents the scale of the wind gusts, V/f , relative to the size of the building, H . The power spectral density, $fS_{uu}(f)/V^2$ represents the energy of the gusts as a function of the non-dimensional frequency.

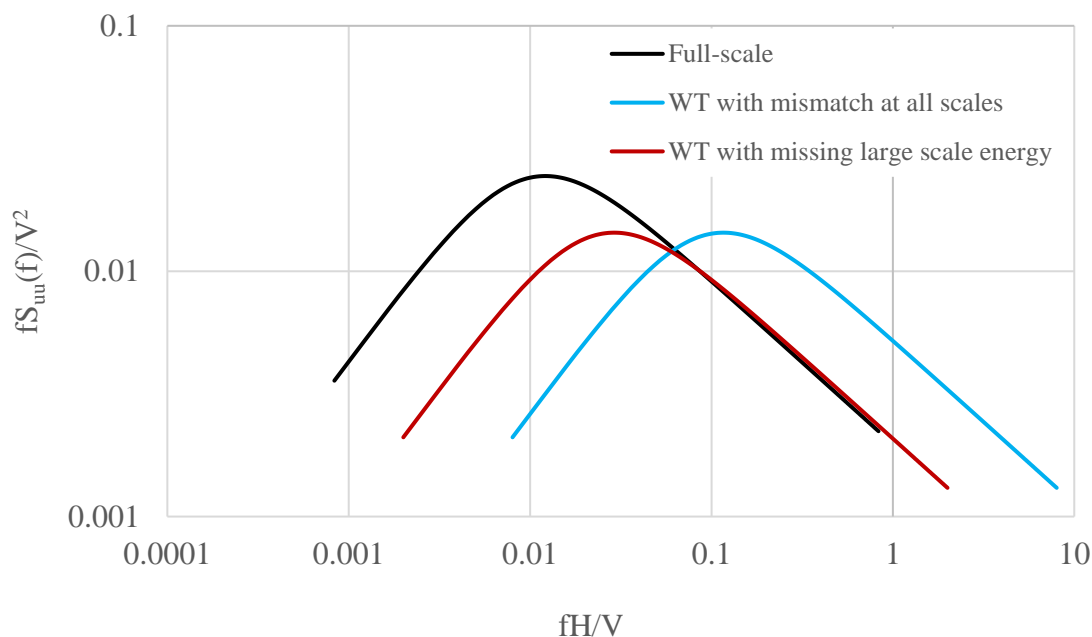


Figure 1: Streamwise velocity spectra for full-scale and wind tunnel data (after Irwin, 2008).

When large model-scales are used in traditional boundary layer wind tunnels, it is typical that there is insufficient energy at the large scales (i.e., low frequencies). This is illustrated in Figure 1, which shows the typical mismatch between a full-scale spectrum and that from the wind tunnel. Irwin (2008) has explained this problem in detail.

Tieleman (2003) suggested the approach of adding turbulence, such that the turbulence intensities (I_u) of model-scale and full-scale are same. However, this leads to mismatches at all scales. Irwin (2008) and Asghari-Mooneghi (2016) suggested not to use this approach, but rather correct the missing large scales using quasi-steady theory and match the energy level at the scales of the separated shear layer. The challenge is that there is no agreement on this issue and the added turbulence could be viewed as entirely different terrain.

The effects of model-scale also play a role. The two wind tunnel spectra in Figure 1 have the same turbulence intensities but the model-scale is varied so the normalizing parameter, H , is altered. The value of H shifts the spectra to the right or left depending on its value. Of course, changing H can also be viewed as changing the building size, which implies that differences in the spectra are due to terrain differences. Figure 2 shows the example of a large model used in the study of Browne et al. (2013). In this case, they used a scale of 1/25 in a wind tunnel that would more typically be used at a scale of 1/300 to 1/500. These authors indicated that the terrain was suburban even though $I_u \approx 0.16$ at the roof height. This interpretation will have a clear impact on resulting pressure coefficients, given the important effects of integral scales (Saathoff and Melbourne, 1997).

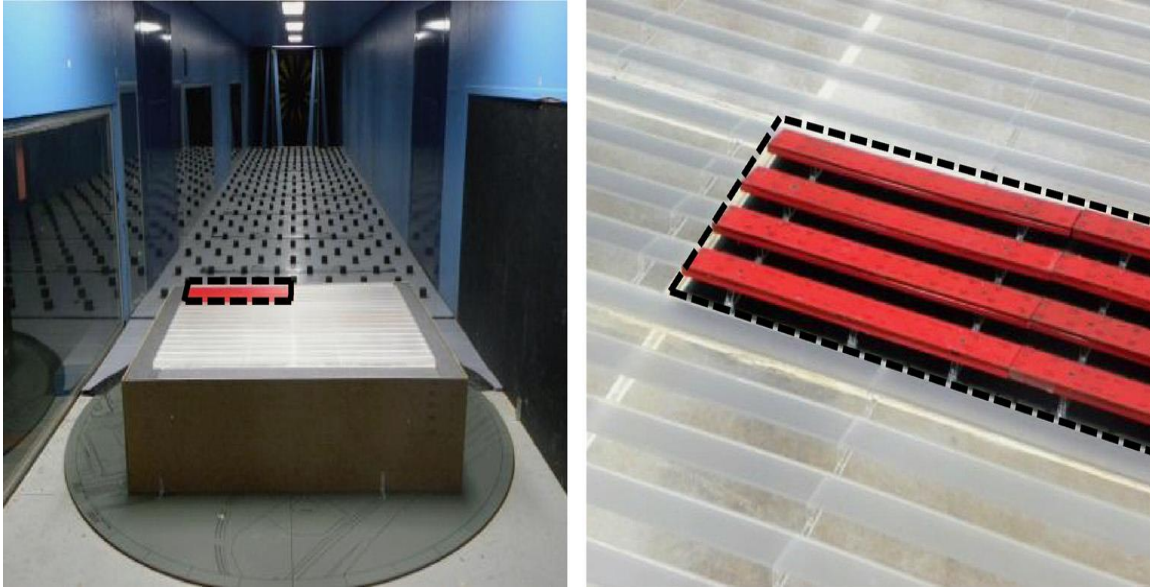


Figure 2: Selected scale model of solar array in boundary layer wind tunnel (from Browne et al., 2013).

An example of differences in interpretation of the terrain can be seen via the turbulence intensity (I_u) and velocity ratio (U/U_{ref}) with respect to height (Z) plots found in Akon and Kopp (2016) and Browne et al. (2013). These are shown in Figure 3. Model roof heights for both studies are also shown. The terrain used in Akon and Kopp (2016) is considered to be open, while for Browne et al. (2013) they consider the terrain to be suburban. Though the terrains are different, if the turbulence intensity and velocity ratio at the corresponding roof heights are compared, they are almost the same suggesting a lack of consistency in terrain definition, noting that the roof heights are quite different between the two studies. One could argue that the terrains could be interpreted as being identical but the building sizes are different, as explained above.

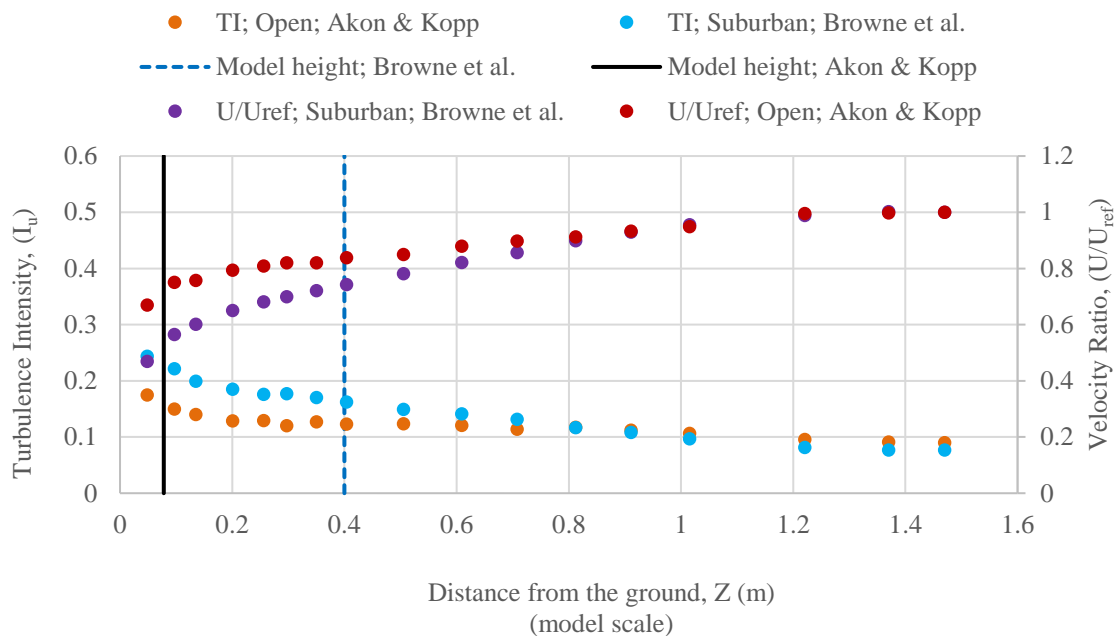


Figure 3: Comparison of turbulence intensity and velocity ratio between Akon and Kopp (2016) and Browne et al. (2013).

Aerodynamic differences caused by these two approaches (i.e., added turbulence to compensate for missing large scales, versus correcting by quasi-steady theory) are unknown. There may be some subtle, but important, effects caused by the differences in the turbulence intensities and integral scales. For example, Banks (2013) and Kopp (2014) both conducted studies related to roof-mounted solar panel arrays, which led to the provisions in SEAOC (2012) and ASCE 7-16 (2017). Reasonably similar pressure coefficients were found, but the critical wind angles and aerodynamic mechanisms were subtly different.

Banks (2013) used similarly-sized building models, but a smoother terrain. Figure 4 shows that turbulence intensity (I_u) was 13% at model roof height (0.15m to 0.3m) and integral length scale to building height ratio (L_u/H) was 4~5. Figure 5 refers to the value

of the worst pressure coefficients on solar panel for wind directions from 0° to 90° relative to the building, as shown by Banks (2013). In this study, the corner vortices dominated the design pressure coefficients.

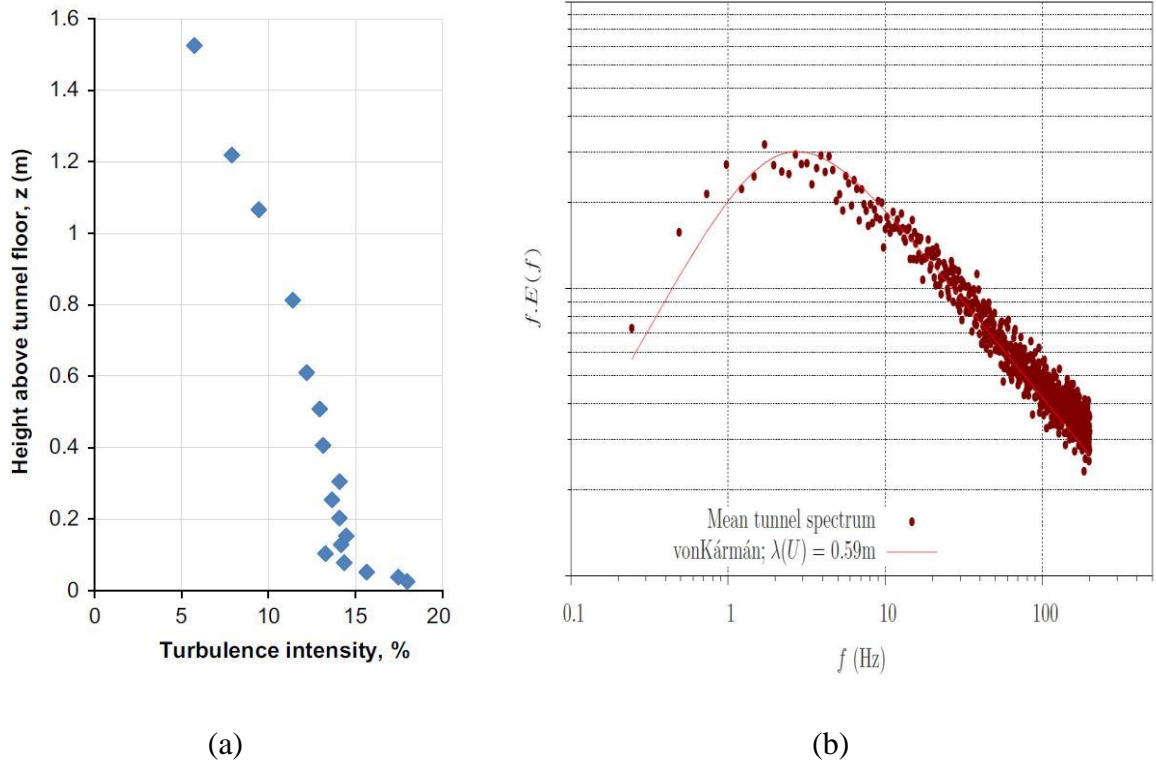


Figure 4: (a) Turbulence intensity; (b) mean tunnel and von Karman spectra of the streamwise velocity fluctuations (images courtesy of Banks, 2017).

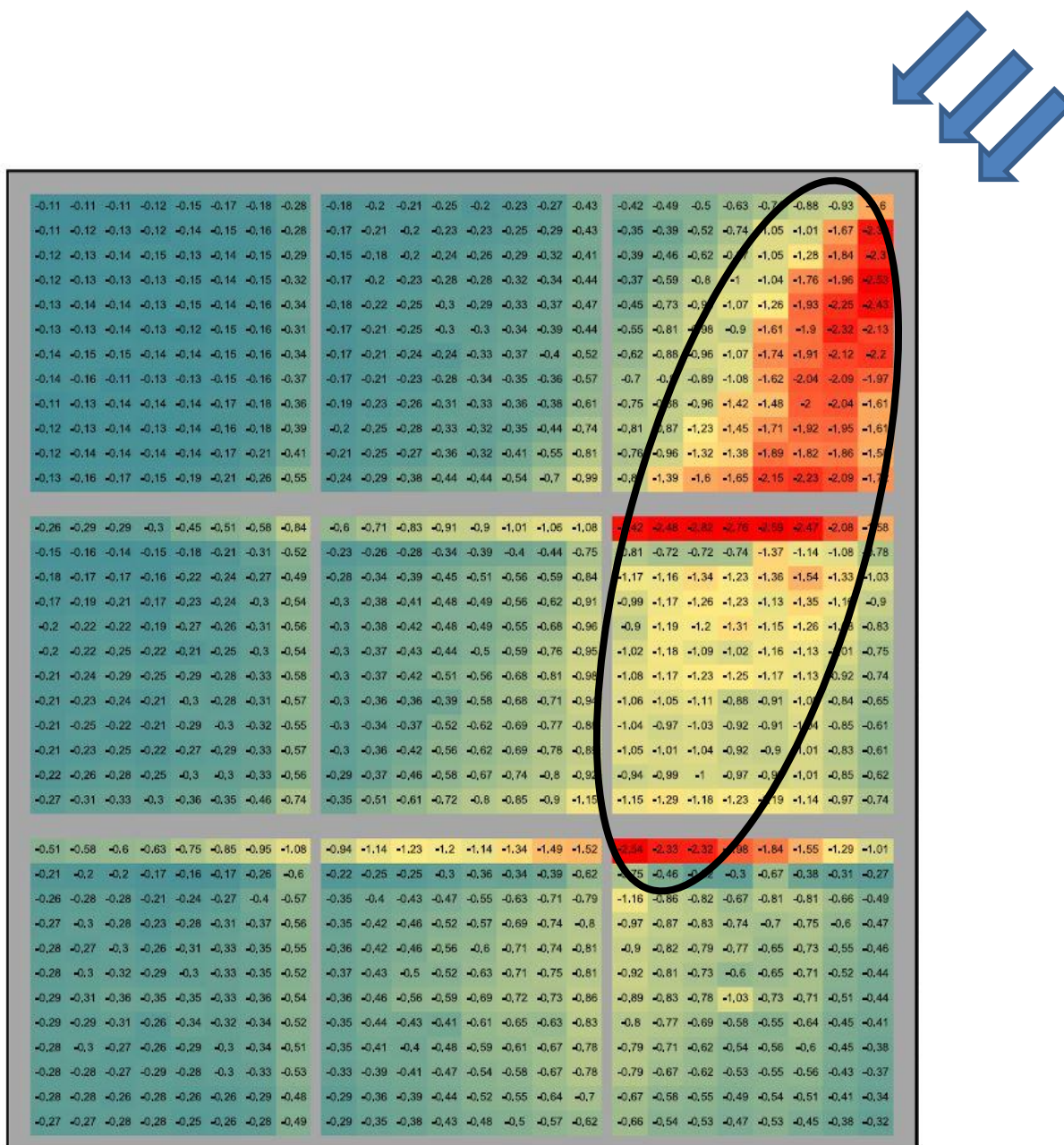


Figure 5: Worst pressure coefficients on solar panel from 0° to 90° relative to the building.

On the other hand, Kopp (2014) used higher turbulence levels in his study. The turbulence intensity and mean velocity profiles, and the streamwise velocity spectra used in his tests are shown in Figure 6. The figure indicates that turbulence intensity (I_u) was

18% at model roof height and integral length scale to building height ratio (L_w/H) was 11. Figure 7 represents the peak wind loads on solar panel found by Kopp (2014). The critical wind directions are shown in the parenthesis. Kopp found that the critical wind directions were for wind normal to the wall. There were subtle differences in turbulence intensity and length scales in these studies. For this scenario, one can ask that what the influence of turbulence (i.e., terrain) on critical wind directions actually is.

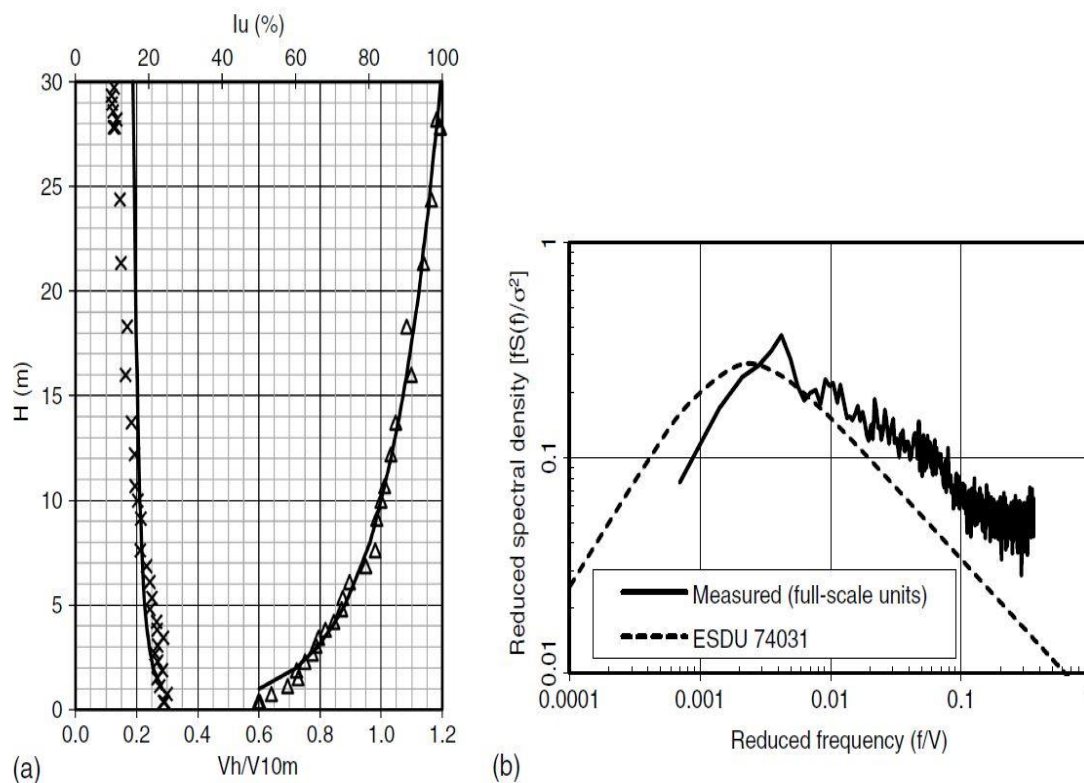


Figure 6: (a) Mean velocity and turbulence intensity profiles; (b) measured and theoretical spectra of the streamwise velocity fluctuations (Kopp, 2014).

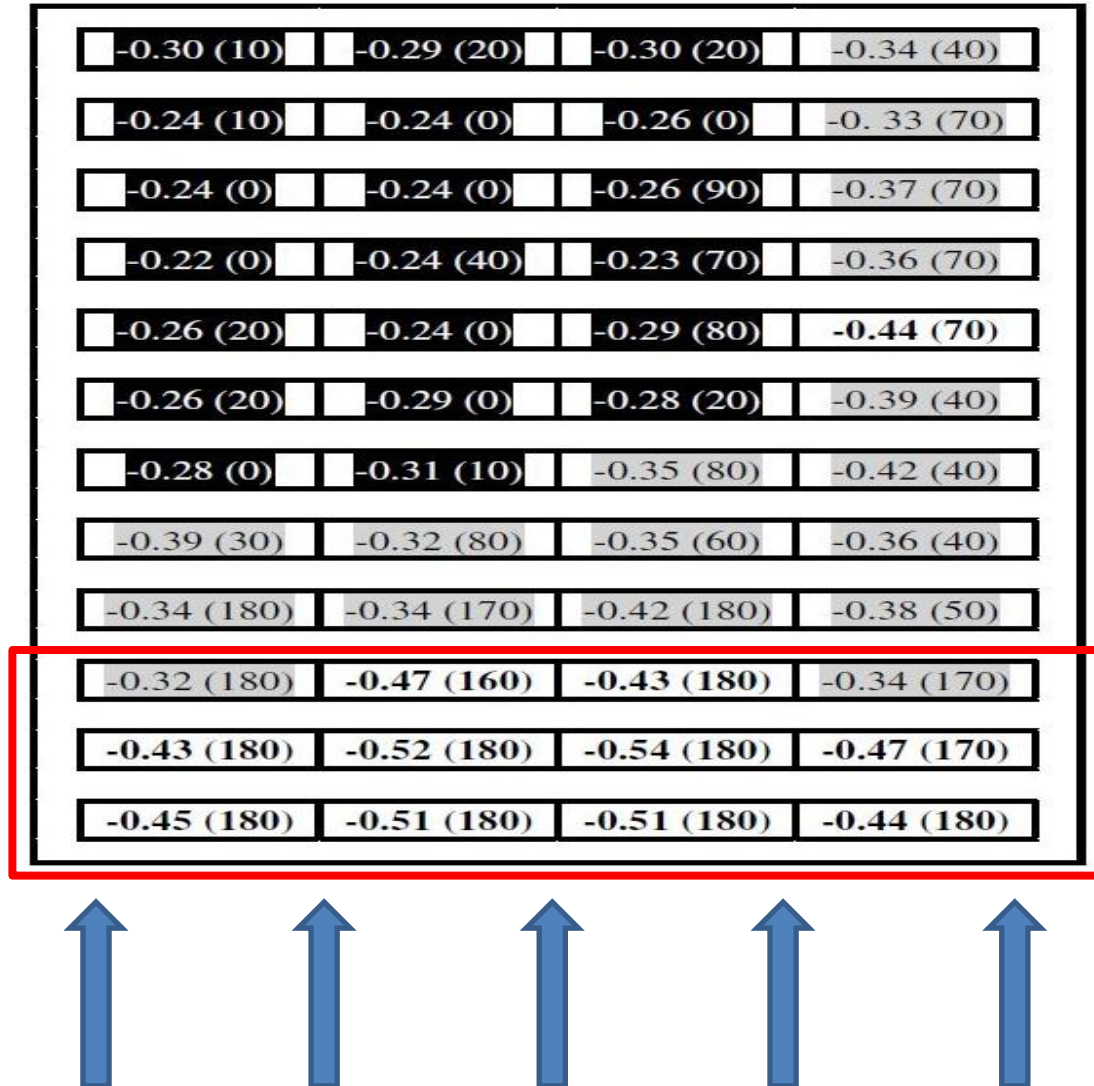


Figure 7: Schematic representation of the peak wind loads on solar panel array.

1.2 Literature Review

The purpose of this section is to introduce the previous studies related to the roof pressure coefficients when wind flows around low-rise buildings. As mentioned in the introduction, severe wind damage is often observed for these type of buildings. Numerous studies have been conducted to understand the mean pressure distributions on

the roofs of low-rise buildings. The mechanism of mean flow and pressure fields in the separated shear region is elaborately described in the literature, for example, Castro and Robins (1977), Tieleman et al. (2003) and Kim et al. (2003). Apart from mean roof pressures, Hillier and Cherry (1981), Bienkiewicz and Sun (1992) and, Saathoff and Melbourne (1997) explained that fluctuating roof pressures depend on both turbulence intensity and integral length scale. However, investigation of peak pressures also plays a vital role due to the importance in the estimation of design roof pressures of low-rise buildings. Several studies in the literature are found to address the influence of turbulence intensity or integral length scale on peak pressures including Melbourne (1979) and, Saathoff and Melbourne (1989, 1997). Saathoff and Melbourne (1989) observed the effects of turbulence intensity (i.e. ratio of the standard deviation of velocity fluctuation to mean velocity) and integral length scale (i.e. a measure of the size of the largest energy containing eddies) on the mean, fluctuating and peak pressures in the separation bubble (the region near the leading edge where flow separates to a wall) for both smooth and turbulent flow. They found that the locations of maximum pressure fluctuations and peak suction within the separation bubble are dependent on turbulence intensity, while the maximum values increase for larger integral length scales. In addition, larger peak pressures are associated with stronger spanwise correlations in the separation bubble, as described in Saathoff and Melbourne (1997). However, it is not clear in the literature whether these similar effects are observed on roof surfaces where the buildings are exposed to various turbulent boundary layers. Pratt and Kopp (2014) expanded these effects to a low-rise building in a simulated open-country terrain. They found that peak suction are associated with locally accelerated flow above the separated shear layer

originating near the leading edge of the building, which scale with the size and location of the roof surface area over which the pressures are integrated. However, there has been far less discussion about the effect of turbulence intensity or terrain condition on peak pressures acting on the roofs of low-rise buildings.

Case and Isyumov (1998) conducted their experiments for two terrains and found that larger wind loads occurred in open terrain compared to suburban due to changes in the wind speeds (with higher mean wind speeds in open terrain). Although the wind loads acting on the roofs are not the same as roof pressures, the influence terrain on the peak pressures of low-rise buildings is clearly important to investigate. Therefore, to obtain the effects of turbulence levels, tests over a three-dimensional bluff body should be carried out by creating appropriate terrain simulation in the wind tunnel. In order to conduct these experiments for different upstream boundary layer conditions, detailed explanations and requirements were described in the study of Tieleman (2003).

When wind approaches at an angle to a wall, vortices are formed from the corner and high suctions occur. Various studies investigating the effects of corner vortices on low-rise building roofs have been found in the literature. An illustration of a typical corner vortex is given in Figure 8, as shown in Banks and Meroney (2001b). The vortex core axis can also be seen in the figure.

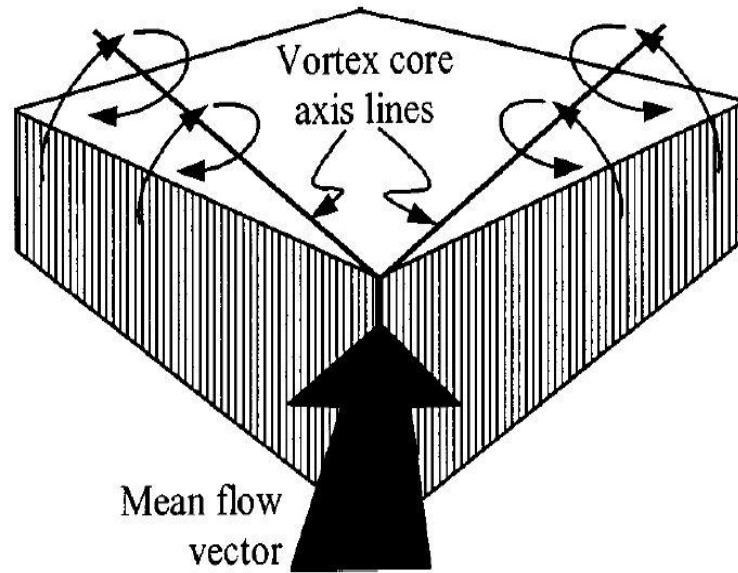


Figure 8: Dual conical vortices in cornering wind (from Banks and Meroney, 2001b).

Corner vortices have the most dominant impact on the roof surface beneath the conical vortex core among all angles of attack for point pressures and small areas, as found by Banks et al. (2000) and Richards and Hoxey (2008). However, due to higher correlation in the flow for larger roof areas, directions orthogonal to the wall are more important than oblique angle for design purposes (Richards and Hoxey, 2008). To estimate the roof surface pressures produced by conical vortices, Banks and Meroney (2001b) developed a model, which describes how the curving vortex flow causes extremely low pressures in the vortex core. In addition, several studies were conducted to mitigate the effect of corner vortices. For example, Kopp et al. (2005) found that the effects of corner vortices can be reduced considerably for all zones over the roof surface by using spoilers and porous perimetric parapets. In addition, Mahmood (2011) conducted experiments for both smooth and turbulent boundary layer flow and found that

the size of corner vortices decreases with an increased radius of curvature of the roof edges. Alrawashdeh and Stathopoulos (2015) recommended that the sizes of edge and corner zones of buildings having larger roofs and lower heights are smaller than those of ASCE7–10 code, in contrast to the results of Kopp and Morrison (2017), who found large zone sizes. This may be due to scaling choices but also the sharpness of roof corners with different model scales.

Bubble separation forms when wind approaches normal to a wall and is known to depend significantly on turbulence levels (i.e., the terrain condition), as shown by Akon and Kopp (2016). These authors found that reattachment lengths on the roof surface depend mainly on turbulence level and the building aspect ratio. Hence, it is important to investigate the critical wind directions, which represent the wind angles at which the highest loads occur under different turbulence levels. An approach of analyzing the critical wind directions was first introduced by Kopp and Morrison (2017) and it was found that the critical wind directions were normal to the walls for the building models having smaller plan dimensions in open-country terrain. However, the effects of turbulence intensity (i.e., terrain differences) on critical wind directions on the roof of low-rise buildings has not been studied in the literature.

Irwin (2008) showed how full-scale spectra could not be attained for large model-scales since the larger scales of turbulence cannot be simulated in the wind tunnel due to the limitations in the size of the test sections. Different wind tunnel laboratories follow various procedures to resolve this scale mismatch, especially for large models as discussed in section 1.1 with respect to Figure 1. To resolve this issue, Tieleman (2003) proposed to increase the turbulence intensity in the wind tunnel for low-rise building

models. This approach can mitigate the problem of matching the turbulence intensity between the full-scale and model-scale to some extent, but the spectra are then not fully matched. In addition, this added turbulence could be considered as different terrain, as pointed out by Irwin. In contrast, Asghari-Mooneghi et al. (2016) recommended to divide the turbulence into two different parts. These authors proposed that higher frequency levels can be simulated in the wind tunnel, while lower frequencies can be estimated by the assumption of quasi-steady theory. Supporting this, Wu and Kopp (2016) found that for larger integral length scales, quasi-steady theory performs better in the estimation of peak pressure prediction. The problem is that there is no agreement in the literature with respect to fixing this issue to date.

The two approaches, described in Tieleman (2003), and Asghari-Mooneghi et al. (2016) can affect the large-scale testing aerodynamically, which is discussed in the previous section in detail. The problem is that different critical wind directions were obtained on the roof-mounted solar panel arrays. Banks (2013) found the design pressure coefficients for angular wind directions or corner vortices, while Kopp (2014) reported the same for normal wind directions to the wall. In these studies, the turbulence levels or terrain conditions and normalized integral length scales were not similar. The reasons of the difference in the critical wind directions and aerodynamics have not been resolved yet in the literature.

1.3 Objectives

The objective of this study is to examine how magnitudes and critical wind directions of the area- averaged pressure coefficients change with terrain (turbulence) differences and building size. The hypothesis is that lower turbulence levels and relatively larger building may lead to corner vortices dominating to a greater extent, while higher turbulence level and smaller buildings may lead to bubble separation dominating to a greater extent.

1.4 Overview of Thesis

A study based on experimental data obtained from a boundary layer wind tunnel will be presented in this thesis. Experimental set-up and the analysis procedures will be described in Chapter 2. The building models and terrain simulation will be discussed, along with the details of the methodology. Chapter 3 deals with the results of the roof pressure coefficients. Validation of the data and discussion about the findings will also be described. Chapter 4 will discuss the conclusions and recommendations of this study.

Chapter 2

2 Experimental Setup

2.1 Introduction

In order to investigate the terrain influences on the roof pressure coefficients on low-rise buildings, a high-resolution of pressure taps was used on several models. The specification of the wind tunnel, model geometry, terrain simulation, and testing parameters for the experiments are described in detail in this chapter. One of the models had a similar geometry as tested earlier (i.e., Akon and Kopp, 2016) and the data obtained from the present study is validated with that previous study.

The testing was conducted in Boundary Layer Wind Tunnel (BLWT) II at the University of Western Ontario. Many experiments have been performed in this wind tunnel in the past. It has a high-speed test section, which is nominally 3.4 m wide with a height of 2.4 m. The upstream fetch of the test section is 39 m. The wind tunnel floor has many rows of surface roughness blocks. The roughness blocks can be raised from the floor to different heights, up to a maximum height of 0.2 m, by a pneumatically-controlled system. Spires and barriers of different sizes can be used at the entrance of the high-speed test section to obtain desired upstream boundary layer conditions.

2.2 Building Models

Wind tunnel tests were performed on several buildings, one of which was a scaled model of Texas Tech University “WERFL” building (TTU building). A detailed description of the TTU building can be found in Levitan and Mehta (1992a, 1992b). On the roof surface, 950 pressure taps were uniformly distributed in 25 rows by 38 columns in a removable panel. Figure 9(a) shows the arrangement of the high-resolution pressure tap layout. Plan dimensions and eave heights of the models were varied to obtain buildings with different aspect ratios. Four different plan shapes were achieved by attaching identical dummy blocks with the main block containing the pressure taps. Model-scale plan dimensions of these configurations are shown in Figure 9. Figure 10(a) depicts the height of the first case, whereas Figure 10(b) shows the second case, which is 3 times the height of first one. In total, tests were carried out for eight different building models. Table 1 presents all combinations of plan shapes and heights from the experiments. Both wall aspect ratios are shown in this table.

It is important to note that the range of aspect ratios spans both low-rise, i.e., those with $H/W < 1$, and mid-rise, i.e., $H/W > 1$. Since corner vortex strength is expected to scale, to some extent, with the wall area (e.g., Banks, 2013; SEAOC, 2012), the buildings with $H/W > 1$ do have $H/L < 1$, such that the corner vortex on one side of the building has a low-rise shape, while on the other it does not. This will provide additional information on the role of building geometry as it pertains to the thesis objectives.

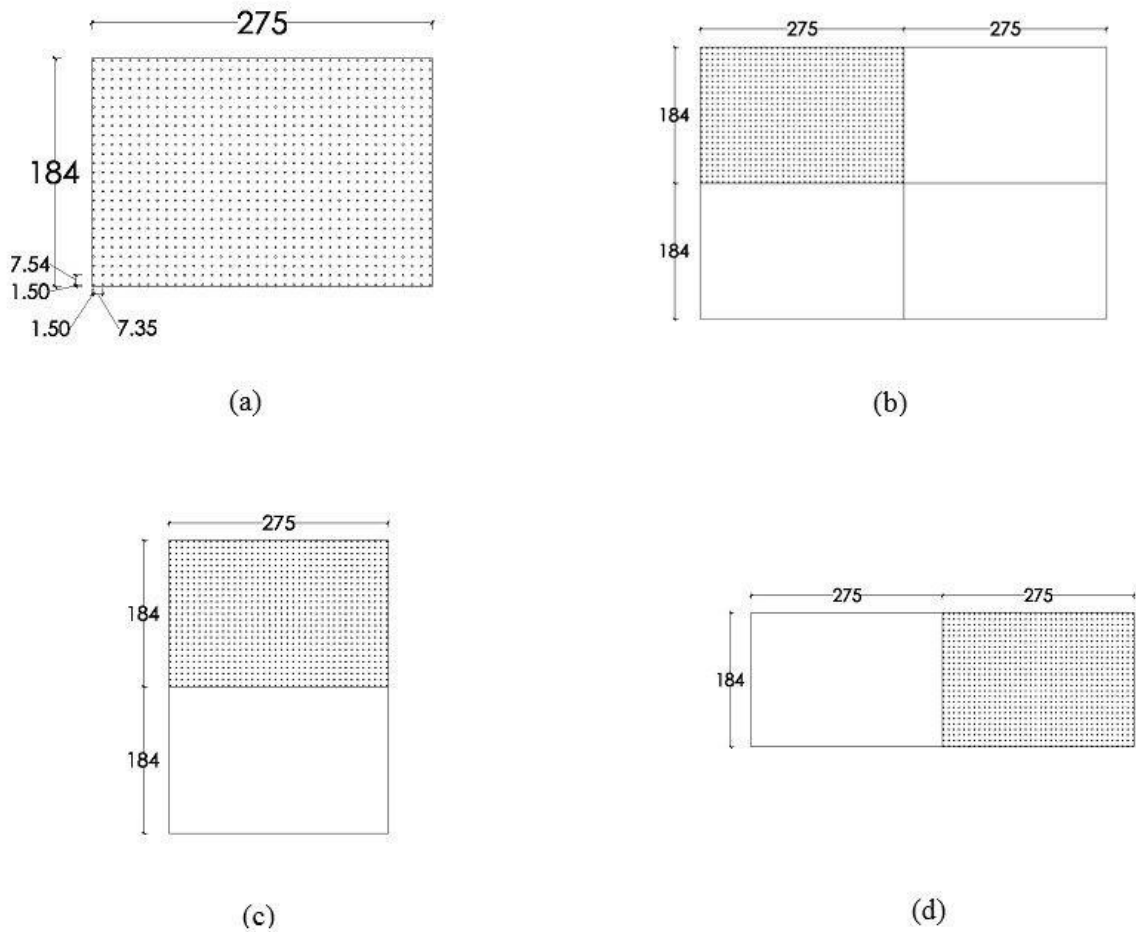


Figure 9: Various plan shapes of the model: (a) Building 1 (B1), (b) Building 2 (B2), (c) Building 3 (B3), and (d) Building 4 (B4), where 950 pressure taps were uniformly spaced in one block and dummy blocks were attached for different configurations.

Dimensions are given in mm.

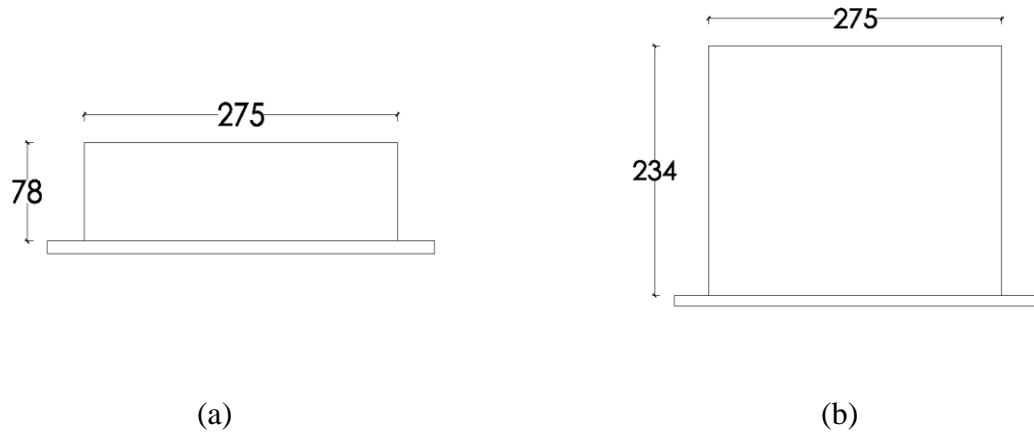


Figure 10: Height variations of the model: (a) Height 1 (H_1), and (b) Height 2 (H_2).

Table 1: Different configurations of plan dimensions and heights of the models in the experiment.

Label	Plan dimensions (mm)		Height (mm) (H)	Aspect ratios			Data availability		
	Length, L (Larger)	Width, W (Smaller)		H/W	H/L	W/L	Terrain With Barrier (L)	Terrain Without Barrier (S)	
B1H1	275	184	78	0.42	0.28	0.67	Yes		
B1H2			234	1.27	0.85				
B2H1	550	368	78	0.21	0.14	0.67			Yes
B2H2			234	0.64	0.43				
B3H1	368	275	78	0.28	0.21	0.75			N/A
B3H2			234	0.85	0.64				Yes
B4H1	550	184	78	0.42	0.14	0.33			N/A
B4H2			234	1.27	0.43				Yes

The range of wind directions chosen depends on the symmetry of the plan shape of the model. The entire range of wind directions was chosen in such a way that the pressure coefficients over the entire roof surface could be obtained for any combination of 0° to 90° wind directions. In all configurations, the increment of the wind angles was

10°. Wind directions over the model are shown in Figure 11. Table 2 refers to various ranges of wind directions for each plan shape during the experiment.

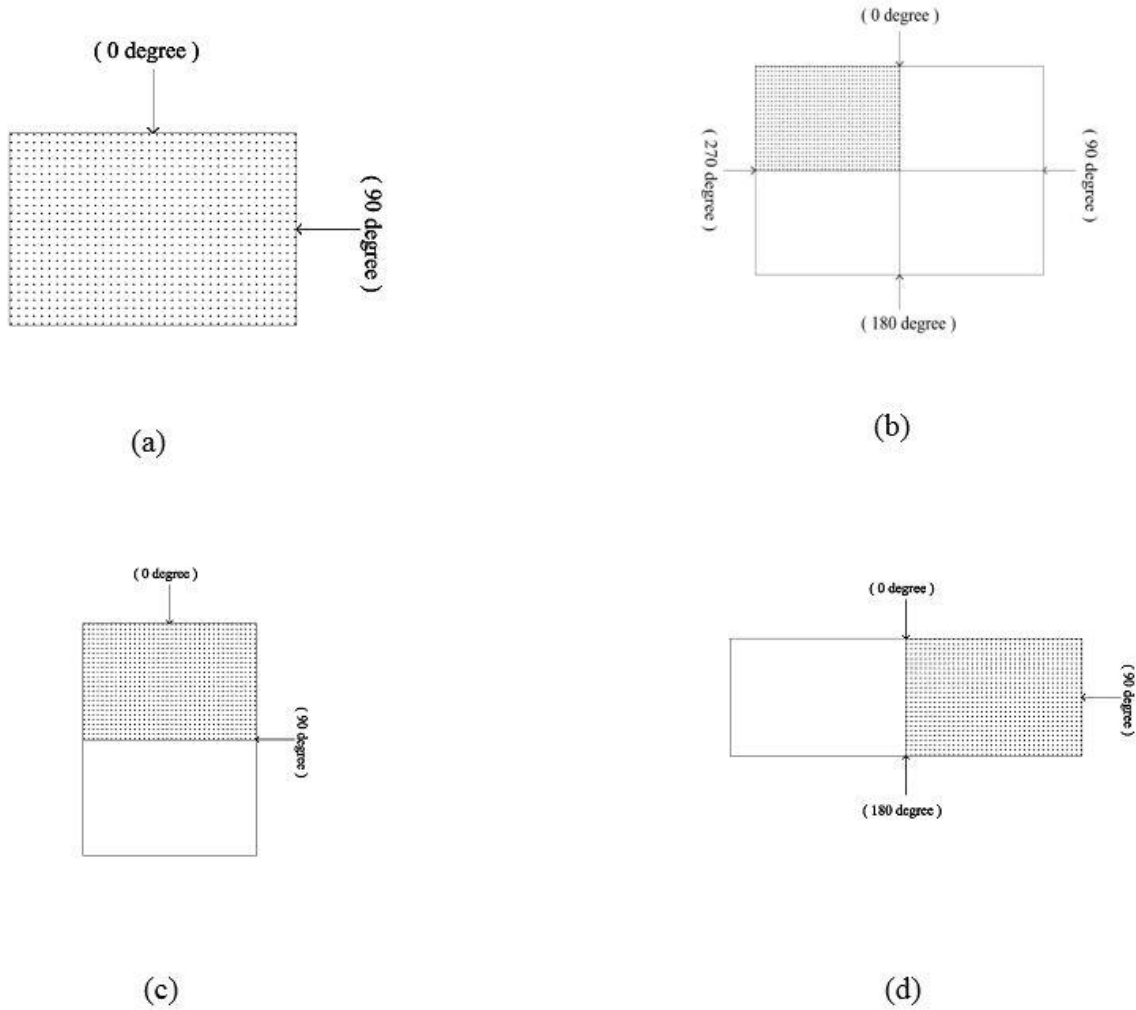


Figure 11: Wind directions for each of the models: (a) B1, (b) B2, (c) B3, and (d) B4.

Table 2: Tested wind directions.

Wind directions for different plan shapes			
B1H1 & B1H2	B2H1 & B2H2	B3H1 & B3H2	B4H1 & B4H2
0°-90° ; every 10°	0°-360° ; every 10°	0°-90° ; every 10°	0°-180° ; every 10°

2.3 Terrain Simulation

The experiments were carried out for six distinct upstream boundary layer conditions. There were three different terrains, which are indicated as 1 (Flat), 2 (Open), and 3 (Suburban). The three configurations having 0.38 m tall barrier at the entrance of the upstream are denoted as 1L, 2L, and 3L, whereas the three having no barrier at the inlet are denoted as 1S, 2S, and 3S. This means the number represents the nature of the terrain whereas L refers to the existence of the barrier with larger turbulence length scales and S refers to the no barrier condition with smaller turbulence length scales. The different characteristics of six upstream boundary layer conditions, such as mean velocity profile, streamwise turbulence intensity, and vertical turbulence intensity, performed in Akon and Kopp (2016), were similar in this experiment. Figures 12, 13, and 14 represent the profiles of the mean streamwise velocity (normalized by the mean velocity at roof height

H_1), U/U_{H1} , streamwise turbulence intensity, I_u , and vertical turbulence intensity, I_w , respectively, with respect to the distance from the ground, y/H_1 .

Figure 12 indicates that mean velocity profiles in the immediate vicinity of the roof surface are almost same, irrespective of the terrain roughness. However, from Figures 13 and 14, it is shown that turbulence intensity, which is the ratio of the standard deviation of the streamwise velocity fluctuations to the mean velocity, depends mainly on the terrain roughness.

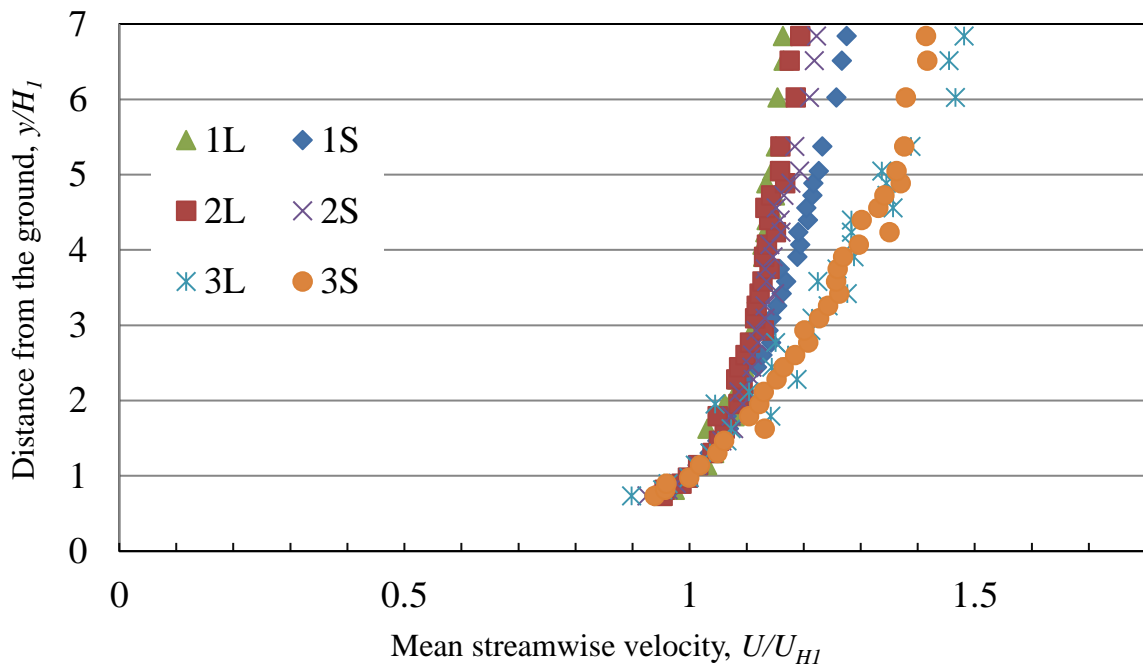


Figure 12: Mean velocity profiles for various upstream conditions.

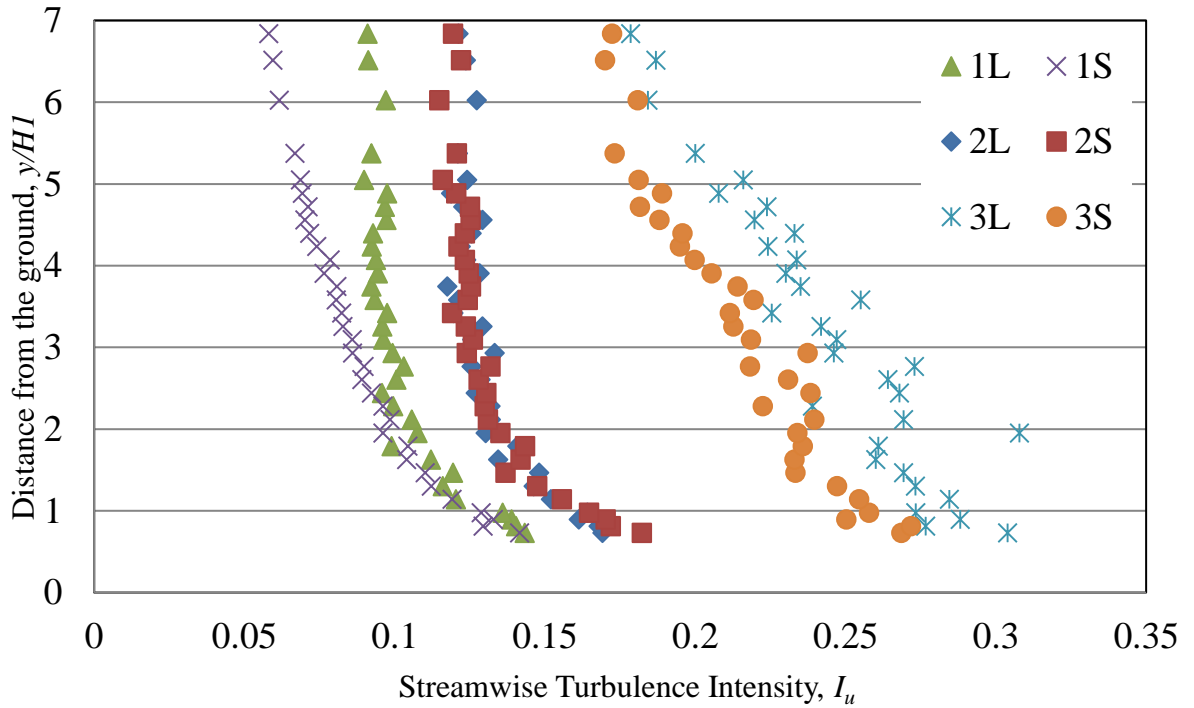


Figure 13: Streamwise turbulence intensity profiles for different upstream conditions.

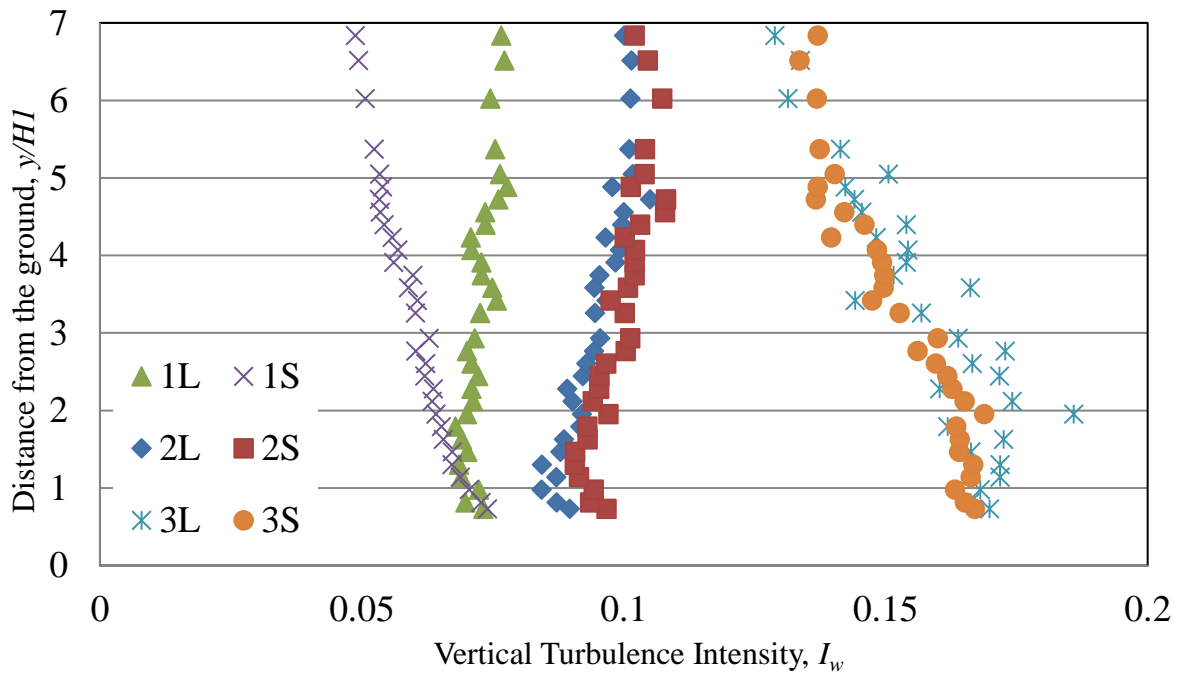


Figure 14: Vertical turbulence intensity profiles for different upstream conditions.

From Figures 15 and 16, it can be concluded that turbulence length scales, L_x , which are a measure of the sizes of the largest energy containing eddies, depends primarily on the existence of the barrier, whereas turbulence intensity depends on the roughness blocks.

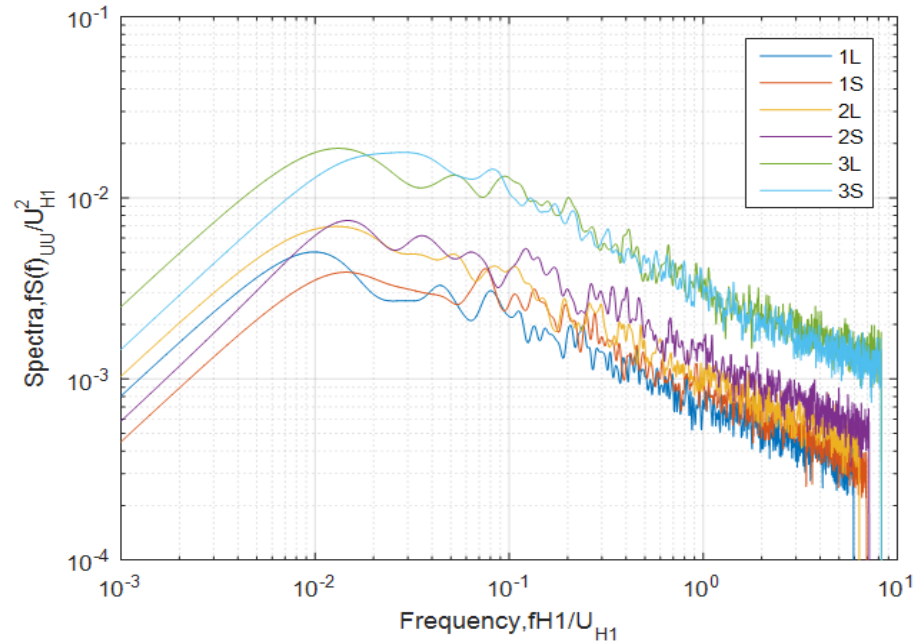


Figure 15: Streamwise velocity spectra at model height, H_1 .

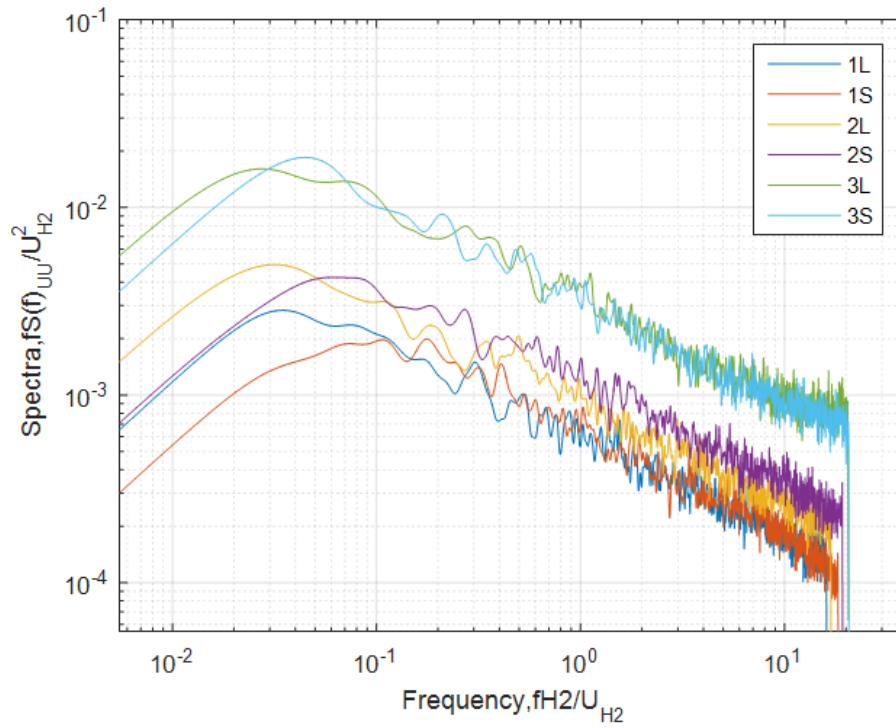


Figure 16: Streamwise velocity spectra at model height, H_2 .

Table 3 refers to various features of six atmospheric boundary layer upstream cases for two different heights, H_1 and H_2 , which are also similar to those used in Akon and Kopp (2016). Here, the roughness lengths (y_o) comes from a log-law fit, which assumes that the boundary layer is in equilibrium. The Jensen number ($J_e = H/y_o$) refers to the ratio of building height to roughness length. This scaling parameter is described in Holmes and Carpenter (1990) for low-rise buildings.

Table 3: Properties of the upstream boundary layer simulations.

Terrain	Barrier (m)	Roughness Length, y_o (m)	Turbulence Intensity, I_u		Integral Scale, L_x		Jensen Number, J_e	
			$y = H_1$	$y = H_2$	L_x/H_1	L_x/H_2	H_1/y_o	H_2/y_o
1L	0.38	0.00013	14	10	13	4	600	1840
1S	0	0.00014	13	9	6	2	540	1710
2L	0.38	0.00014	17	13	11	5	600	1840
2S	0	0.00027	17	13	8	2	290	890
3L	0.38	0.0011	27	25	12	3.5	71	220
3S	0	0.0014	26	22	7	3	56	170

2.4 Testing Parameters

Pressure data were obtained at 625 Hz for 120 seconds at each angle of wind in the experiment. As a consequence, for each pressure tap, time histories of 75000 pressure coefficients were taken for each mean wind direction. To obtain pressure data, pressure taps were connected to the pressure scanners by a tubing system. A detailed description of the tubing system can be found in Ho et al. (2005). In total, 61 16-channel pressure scanners were used in the experiments. Pitot-static tubes were fixed at a standard height of 147 cm from the wind tunnel floor where the wind speed was measured to be about 10.35 m/s. Wind speed data were taken by two cobra probes at roof height (H_1) and at

twice this height. The Reynolds number for the experiments, based on the mean wind speeds at the mean roof heights, are in the range from 35,500 to 117,000. Synchronization of pressure and wind speed was done in the experiment, although the simultaneous wind speed and pressure were not used in the analysis. Very few pressure taps malfunctioned during the test. In total, 48 cases, which include 6 terrains and 8 building shapes, were obtained during the testing. Figure 17 displays a photograph of the experimental setup of a model during the experiment in wind tunnel. Pitot-static tube, Cobra probe, barriers, spires, roughness block, and scattered nuts that were used during the tests can be seen in the photograph.



Figure 17: Photograph of the experimental setup of a model in wind tunnel.

2.5 Analysis Process

2.5.1 Area Averaging

In this analysis, an area-averaging approach was implemented to investigate the pressure distribution on the roof surface of the low-rise buildings. This method has been used in several previous studies, for example, Lin et al. (1995). In order to provide the same weight to all equally spaced pressure taps, the following equation (1) was applied:

$$C_p(t) = \sum_{i=1}^m \sum_{j=1}^n C_{p_{ij}}(t) \frac{a_{ij}}{A} \quad (1)$$

where $C_p(t)$ refers to the area-averaged pressure coefficient to the corresponding tributary area. Various sizes of square areas such as 1x1, 2x2, 3x3, 4x4, 5x5, 6x6, 7x7, and 8x8 were taken for the analysis. For example, 3x3 matrix refers to 9 pressure taps in a square layout. Then, the average of these 9 pressure coefficients was taken. This average value will represent the overall pressure coefficient of that square area as a function of time. Both overlapping and non-overlapping configurations of pressure taps were used in this study.

2.5.2 Extreme Value Analysis

There are fluctuations in the measured pressure coefficients during the test due to the turbulent characteristics of wind. In order to estimate reliable peak pressures from the wind tunnel data, an extreme value analysis is required. In this analysis, the Lieblein Best Linear Unbiased Estimator (BLUE) method (Lieblein, 1974) is applied to determine the extreme value distribution.

To implement the Lieblein BLUE method (Lieblein, 1974), each time history in the complete data set was divided into ten equal segments. Each segment comprised 12 seconds of the testing time in wind tunnel. From each segment, the maximum and minimum value were taken and then sorted from the lowest to highest (or highest to lowest) value. To obtain the distribution, several factors were multiplied with these values.

The following equations (2) and (3) were applied in calculating the extreme value distribution.

$$u'_n = \sum_{i=1}^{10} a_i \cdot x_i \quad (2)$$

$$b'_n = \sum_{i=1}^{10} b_i \cdot x_i \quad (3)$$

where u'_n and b'_n are the slope and intercept, respectively, when the distribution is linear.

Table 4 shows the factors a_i and b_i , used in this estimation.

Table 4: Factors used in Lieblein BLUE method.

a_i	b_i
0.222867	-0.347830
0.1623088	-0.091158
0.133845	-0.019210
0.112868	0.022179
0.095636	0.048671
0.080618	0.066064
0.066988	0.077021
0.054193	0.082771
0.041748	0.083552
0.028929	0.077940

The cumulative distribution function used in this distribution is given in the following:

$$Prob\{X \leq x\} = e^{-e^{-(x-u'_n)/b'_n}} \quad (4)$$

In this distribution, values were taken for 50th percentile, unless noted otherwise. This procedure was implemented for each single pressure tap at each individual wind direction. The pressure coefficients obtained from this procedure were used to perform the analysis in this study. This approach is consistent with many other studies conducted at UWO (e.g., St. Pierre et al., 2005; Kopp, 2014, and others).

2.5.3 Reference Height Velocity

The pressure coefficients recorded in the pressure measurement system are denoted as $C_{p_{measured}}$. Here, $C_{p_{measured}}$ is referenced to the dynamic pressure at the Pitot-static tube height and \bar{V}_{pitot} is the mean velocity at the Pitot-static tube height. The equation is:

$$C_{p_{measured}} = \frac{\hat{p} - p_o}{\frac{1}{2}\rho\bar{V}_{pitot}^2} \quad (5)$$

The pressure coefficients, C_{P_H} which are referenced to the mean dynamic pressure at the roof height of the model, can be obtained from $C_{p_{measured}}$ as:

$$C_{P_H} = C_{p_{measured}} \left(\frac{\bar{V}_{pitot}}{\bar{V}_H} \right)^2 \quad (6)$$

where \bar{V}_H is the mean velocity at the model roof height. Equation 6 provides least variability over many low-rise building dimensions, which is discussed in Ho et al. (2005). It is assumed that the 3-sec gust speed is approximately $\bar{V}_H + 3\sigma$, where σ is the standard deviation of the streamwise velocity fluctuations. Then, the ASCE 7 – equivalent pressure coefficient is given by:

$$\begin{aligned} GC_p &= C_{p_{measured}} \left(\frac{\bar{V}_{pitot}}{\bar{V}_H + 3\sigma} \right)^2 \\ &= C_{P_H} \left(\frac{\bar{V}_H}{\bar{V}_H + 3\sigma} \right)^2 \end{aligned} \quad (7)$$

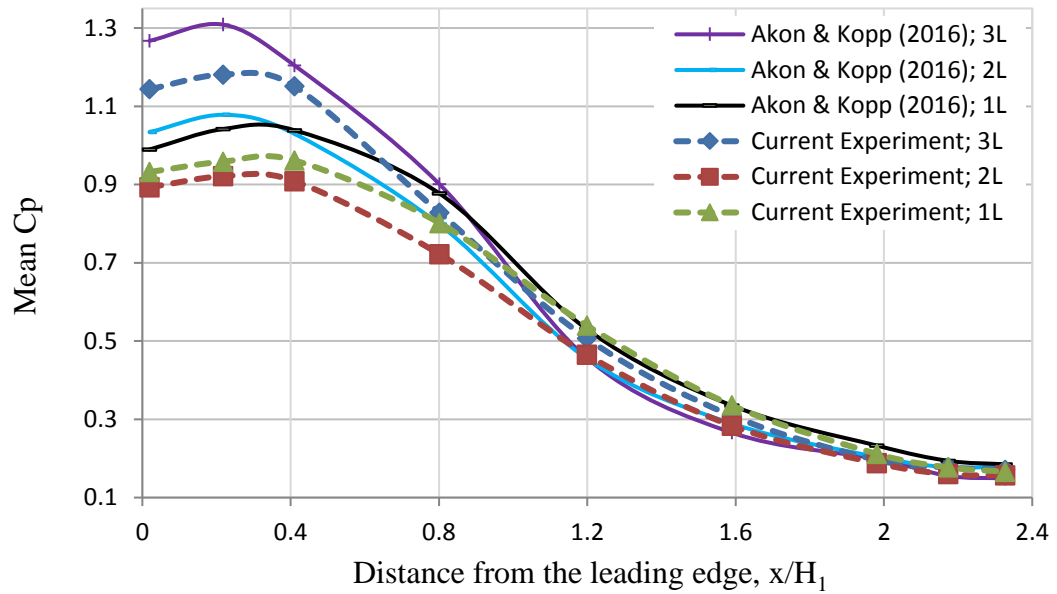
using the same approach as Kopp and Morrison (2017).

Chapter 3

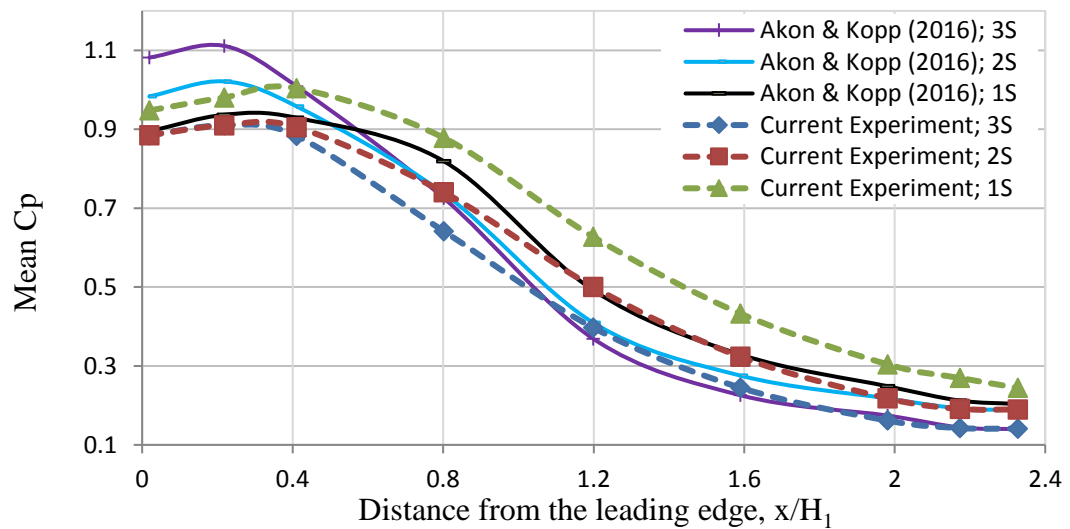
3 Results

3.1 Comparisons with Previously Published Data

Firstly, the current data are compared with the results of Akon and Kopp (2016) to validate the experimental data. Figure 18 shows the distribution of mean pressure coefficients (C_p) along roof centerline with respect to the distance from the leading edge for the model B1 (similar to TTU model but with a flat roof) of the current experiment, and Akon and Kopp (2016) for six upstream conditions. One can see that the shapes of mean pressure coefficients are different for various upstream boundary layer conditions. Both figures depict that the highest magnitude of mean suction C_p occurs near the leading edge and then decreases with the distance from the edge. In addition, the position of maximum C_p varies slightly with upstream conditions in both cases. Although the patterns of the current experiment are similar to the results of Akon and Kopp (2016), there are some differences near the leading edge on the roof surface. The reason of these dissimilarities is due to the slight slope difference between the roofs of the models. Moreover, there was a slight difference in the radius of curvature of the roof edge between the models, which was caused by a different manufacturing process, although this has not been quantified. However, the data are within the measurement uncertainty of about 0.1 C_p (Quiroga, 2006). Based on this, it can be concluded that the data obtained from the current experiment are matched sufficiently well with the study of Akon and Kopp (2016).



(a)



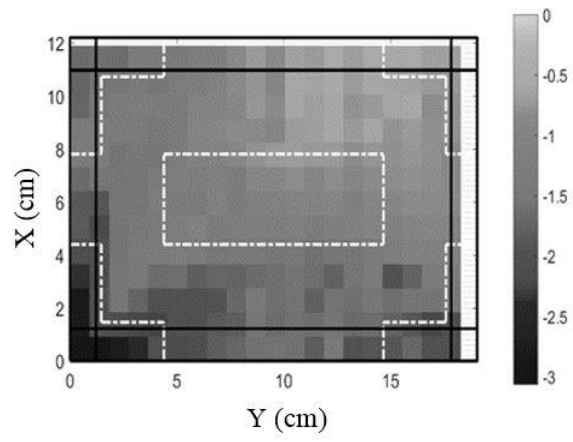
(b)

Figure 18: Comparison of Mean Cp vs. distance from the leading edge, x/H_1 for Building 1 between our experiment and, Akon and Kopp (2016): (a) with barrier, and (b) no barrier.

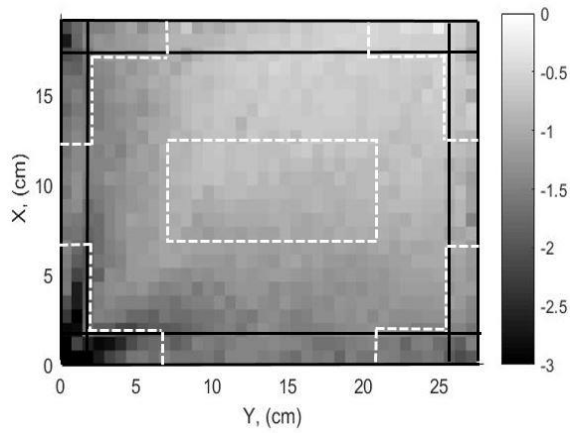
Again, in order to validate our experimental data with the results of Kopp and Morrison (2017), several factors were considered at model scale. Table 5 presents different factors in these two experiments at model scale. Firstly, as building height is a significant parameter on roof zones, a model which is 7.3 cm in height is chosen from Kopp and Morrison (2017), while it is 7.8 cm in our case. Secondly, the tributary area of their experiment is 0.84 cm², while in our case they are 0.49 cm² (single pressure tap), and 2.22 cm² (4 pressure taps in a square pattern). Thirdly, there is a slight difference in aspect ratios. In both cases, the terrain was open (i.e., 2L) and turbulence intensity was almost same at model roof height. In addition, time histories were divided into four segments and Lieblein BLUE method was applied to obtain peaks for both models at 78th percentile; however, the Kopp and Morrison (2017) were extrapolated to a longer duration. The sampling periods were almost same. Figure 19(a) indicates the worst GC_p values for tributary areas of 0.84 cm² on buildings from Kopp and Morrison (2017), while Figure 19(b) and 19(c) are from the current experiment having tributary areas of 0.49 cm², and 2.22 cm², respectively. In these figures, the black lines refer to the ASCE 7-10 definition for the roof zones, while the white dashed lines correspond to the roof zones. One can see that the patterns of the pressure coefficients in both studies are similar. In addition, Figures 19(d) and 19(e) indicate that the worst GC_p values, close to the edge, are higher than those of Kopp and Morrison (2017) for smaller tributary areas, while they are lower for larger tributary areas. When one considers the variations with respect to the distance from the leading edge all three have similar distributions. Thus, one can conclude that the current experiments are sufficiently similar to past data and can be used for further analysis.

Table 5: Comparison of different factors between the models of Kopp and Morrison (2017) and the current experiment at model scale.

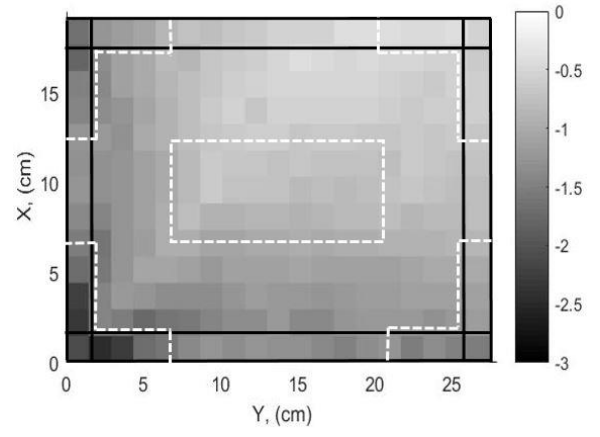
Factors		Kopp and Morrison	Current Experiment
Height, H		7.3 cm	7.8 cm
Aspect Ratio	H/L	0.38	0.28
	H/W	0.59	0.42
Tributary area		0.84 cm ²	0.49 cm ² , 2.22 cm ²
Sampling Period		25 s	24 s
Percentile		78 th	78 th
Terrain		Open	Open (2L)
Turbulence Intensity		0.175	0.17



(a)



(b)



(c)

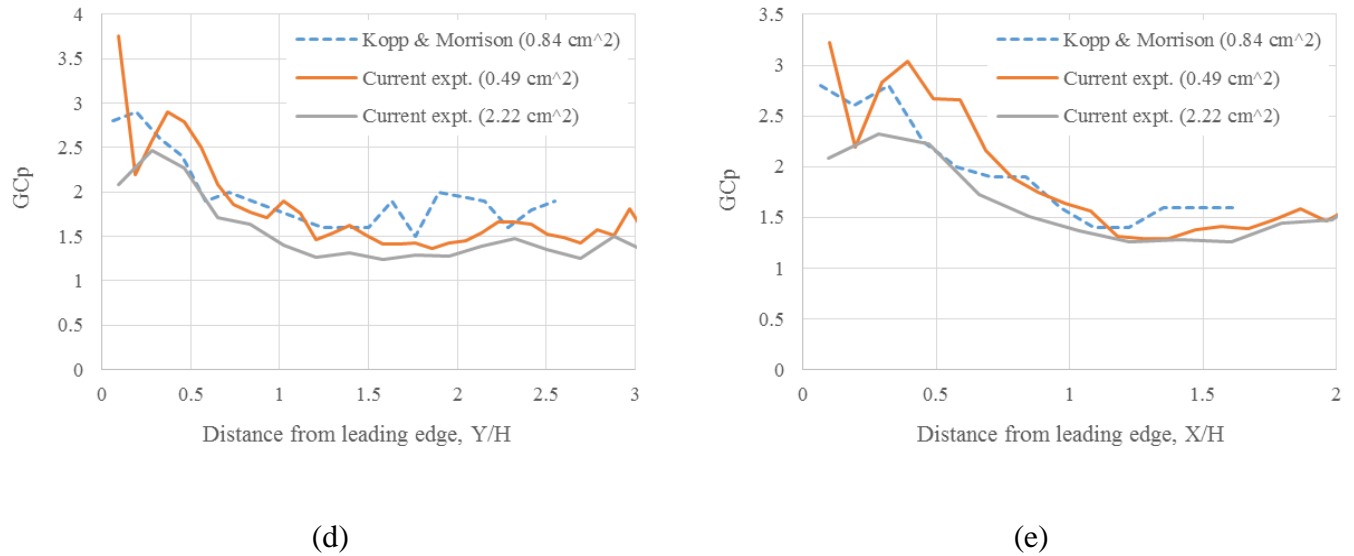


Figure 19: Comparison of worst GCp values for roof zones between Kopp & Morrison paper (a) 0.84 cm², and the current experiment with areas of (b) 0.49 cm², and (c) 2.22 cm², and for distance from leading edge (d) and (e).

The measurement uncertainties in the current experiments are associated with the measurement of surface pressure coefficients, referenced to the roof-height, C_{P_H} , which is calculated by the following equation:

$$C_{P_H} = C_{p_{measured}} \left(\frac{\bar{V}_{pitot}}{\bar{V}_H} \right)^2 \quad (8)$$

where $C_{p_{measured}}$ is referenced to the dynamic pressure at the Pitot-static tube height, and \bar{V}_{pitot} and \bar{V}_H are the mean velocity at the Pitot-static tube height and the model roof height, respectively. Thus, the overall uncertainty in the measurement of C_{P_H} are the combination of the uncertainties of $C_{p_{measured}}$ and the velocity ratio squared. Quiroga (2006) calculated the measurement uncertainties of pressure coefficients referenced to

model roof height (C_{P_H}) in the Boundary Layer Wind Tunnel-II at UWO. Quiroga found that the uncertainties in the measurement of C_{P_H} were mainly due to the uncertainties associated with the measurement of velocity. The measurement uncertainties calculated by Quiroga (2006) were due to hot-wire error, while Akon (2017) calculated the cobra probe error. If the values of the measurement uncertainties obtained from these two studies are compared, then it is observed that cobra probe performs better than hot-wire. In this study, the velocity measurements taken by the cobra probe from Akon (2017) are used. Thus, the pressure coefficients calculated in this study is reasonable for analysis and the measurement uncertainty does not play a vital role here. Akon (2017) estimated the error to be 6.95%.

3.2 Critical Wind directions

3.2.1 Overall Observations

In this study, area-averaged pressure coefficients were calculated among all the pressure taps. Non-overlapping square patterns (2x2, 4x4, and 8x8) were selected for this analysis. Thus, each area-averaged GC_p corresponds to the pressure taps, covering every square on the roof surface. Here, the critical wind direction refers to that wind direction in which the largest magnitude value of the area-averaged pressure coefficient occurs, among all angles of attack from 0° to 90° . According to ASCE 7 – 16 (2017), the roof zones are divided in four different zones. These zones are divided based on the building height, H .

Figure 20 shows the sizes of the roof zones according to ASCE 7 – 16 (2017) and Kopp and Morrison (2017). Similar sizes of the roof zones are shown in this study.

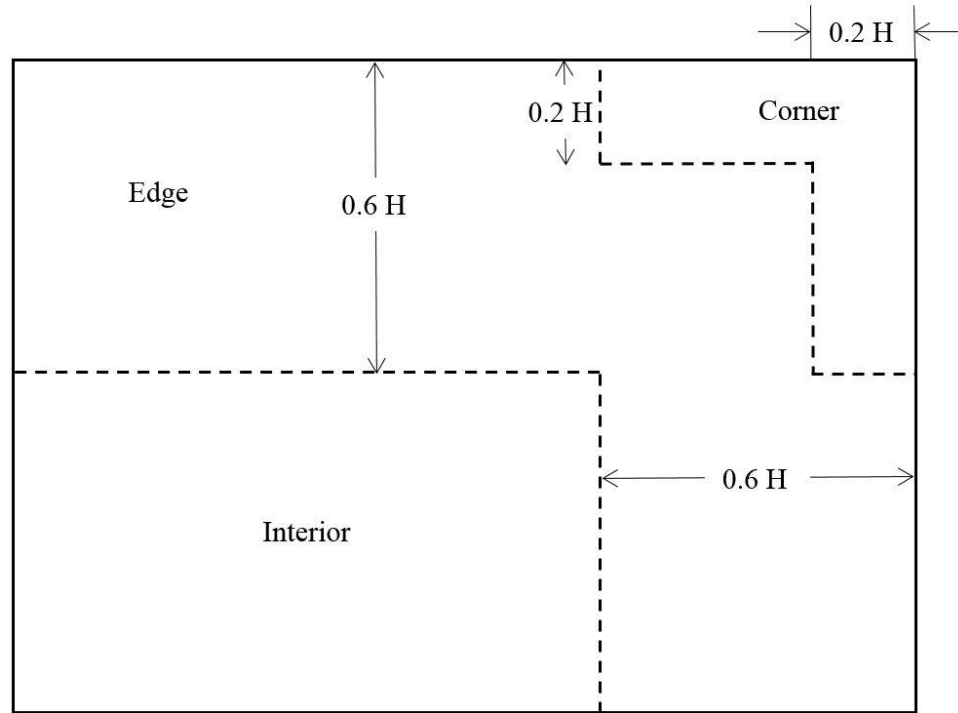


Figure 20: Size of the roof zones in ASCE 7 – 16 (2017).

Figures 21 and 22 indicate the critical wind directions of various building models for different tributary areas over the range of wind directions, 0° to 90° . The entire roof was divided into three zones which are denoted as corner, edge, and interior, similar to the study of Kopp and Morrison (2017), and ASCE 7–16 (2017). In these figures, white dashed lines represent the sizes of the roof zones. Figure 21 shows the critical wind directions of B1H1 for the 1S and 3L upstream conditions. One can see that critical wind directions vary with the terrain differences for corner, edge, and interior zones. That means turbulence intensity plays a role on the critical wind directions over the roof surface. It can also be seen that the area covered by the oblique angles (i.e., $20^\circ - 70^\circ$) are larger in flat terrain (1S) than that of suburban terrain (3L) for the smaller tributary areas

in Figures 21(a) and 21(d). This also holds for the larger tributary areas. Thus, it appears that critical wind directions change with turbulence level and that the corner vortex has greater significance in flat terrain (i.e., lower turbulence) than suburban one (i.e., higher turbulence). While the magnitudes of the pressure coefficients will be examined later, it appears the higher turbulence levels may disrupt the corner vortices more than bubble separations or that bubble separation is enhanced with higher turbulence levels.

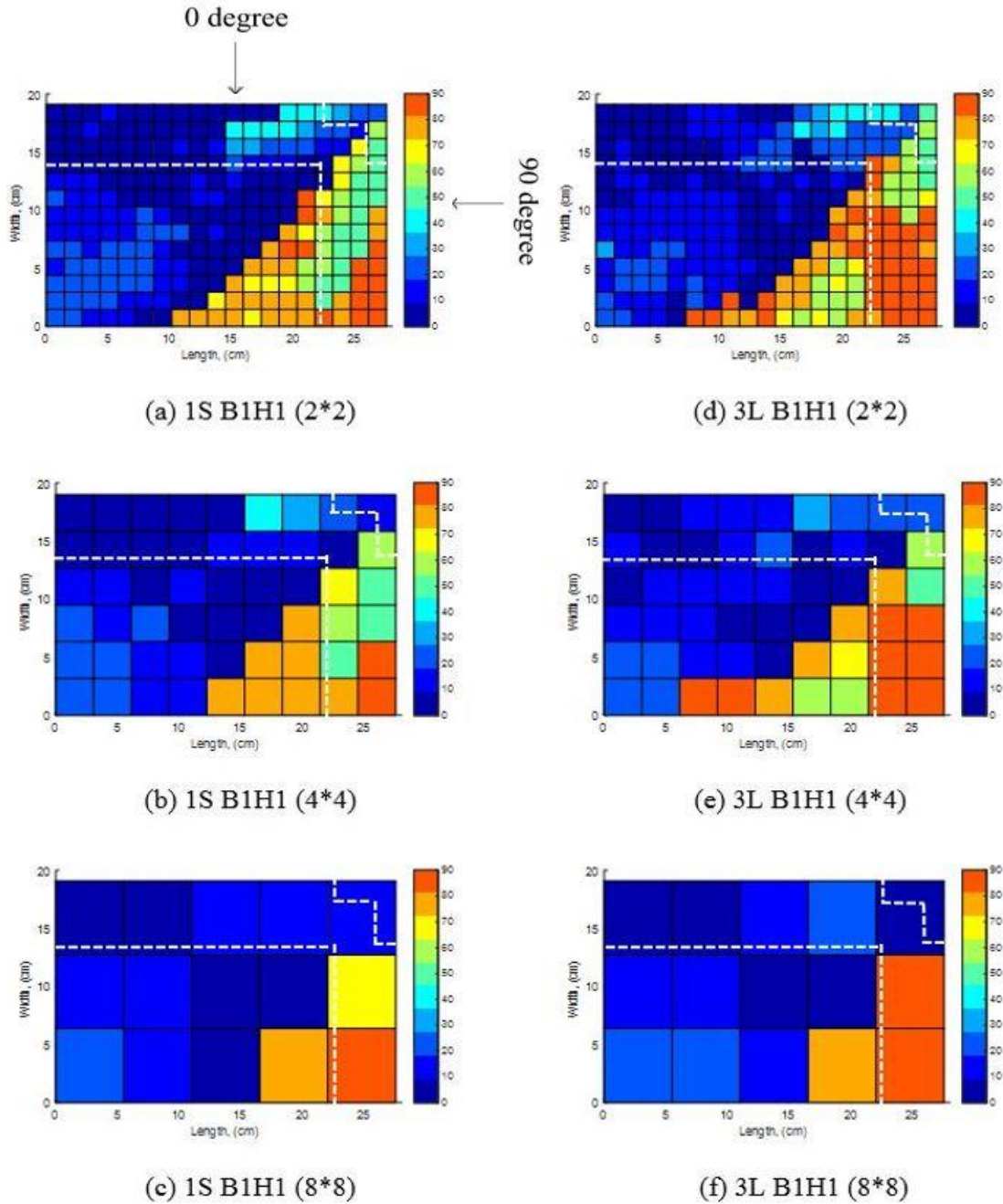


Figure 21: Critical wind directions and different zones of 1S B1H1 and 3L B1H1 for different tributary areas.

To examine the effects of height, each of Figure 22 is for a fixed plan size (B3). Figure 22(a), 22(b), and 22(c) are for $H_1 = 7.8$ cm, while Figure 22(d), 22(e), and 22(f) are for $H_2 = 23.4$ cm. With the change in building height, the size of the roof zones also change, being larger for the larger heights. Again, the ASCE 7–16 zone sizes are included as white dashed lines in the figures. It can be seen that there are differences in the critical wind directions for altered building heights. Figure 22 also indicates that the corner zones are closely related to the regions where oblique wind directions control, consistent with the results of Kopp and Morrison (2017) and the dependence of zone size on height (H) in ASCE 7–16. Based on this, one can conclude that building height is an important parameter on the critical wind directions.

To examine the effects of plan dimensions, Figures 21(d), 21(e), and 21(f) have horizontal dimensions of 27.5 X 18.4, while Figures 22(a), 22(b), and 22(c) are of 36.8 X 27.5, for fixed roof height of $H_1 = 7.8$ cm and fixed suburban terrain (3L). Figures indicate that size of plan dimension does not play a vital role on the critical wind directions over the roof surface on low-rise buildings. Therefore, it can be concluded that plan shape is not sensitive on the critical wind directions over the roof surface.

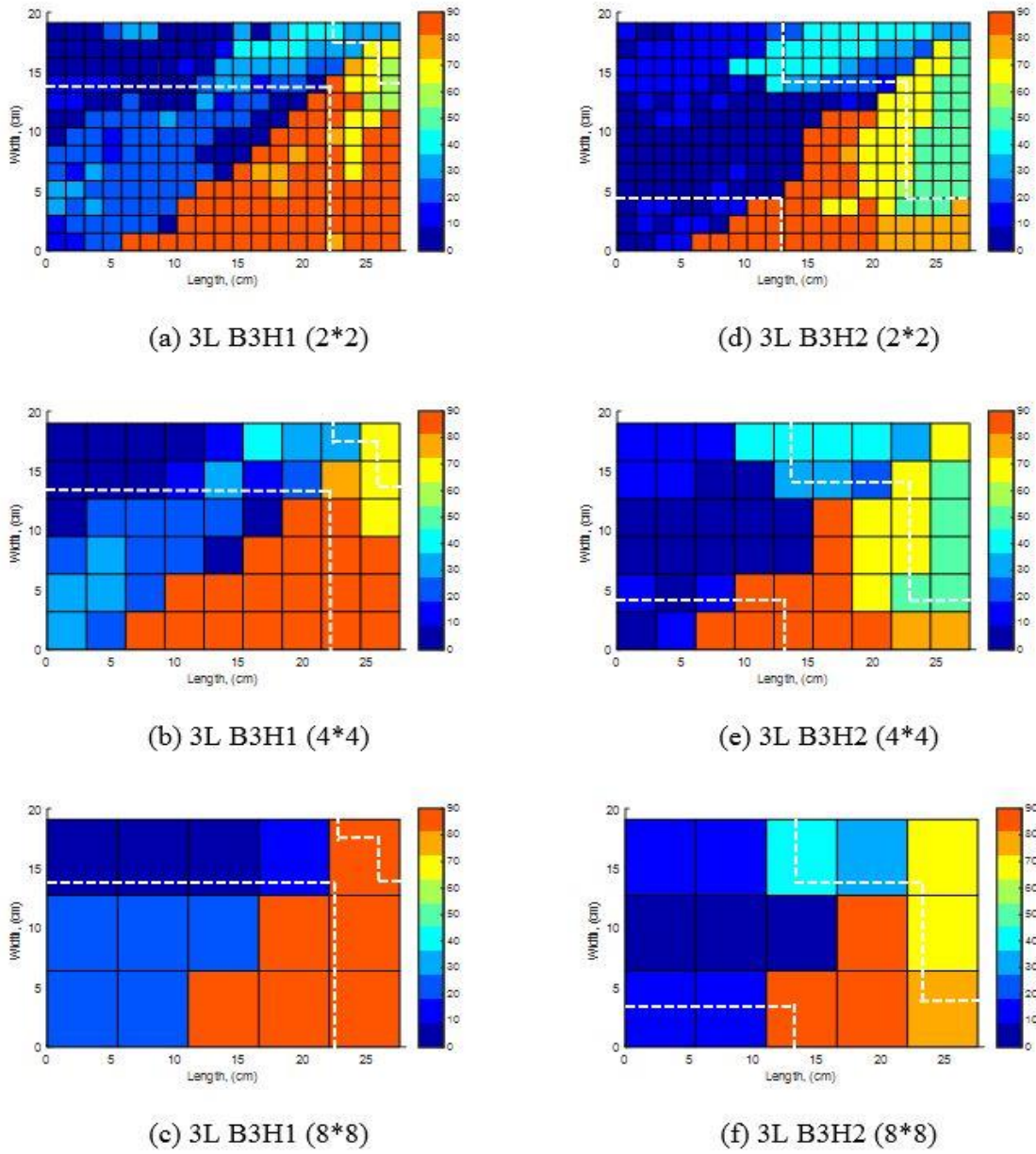


Figure 22: Critical wind directions and different zones of B3H1 and B3H2 for different tributary areas in suburban terrain.

Figures 23 – 31 depict the critical wind directions for the largest magnitude (i.e., enveloped) area-averaged pressure coefficients (GCp) on the roof surface as a function of tributary area for corner, edge, and interior zones of different building models. In these figures, frequency refers to the total number of areas for a particular wind direction. Figures 23 – 25, 26 – 28, and 29 – 31 are for the comparison of the effects of terrain, plan dimension and height, respectively, on the critical wind directions for the three different roof zones. One can see that the oblique wind directions ($20^\circ - 70^\circ$) are important for corner zones, while normal wind directions ($0^\circ - 10^\circ$ and $80^\circ - 90^\circ$) play vital role for edge and interior zones. That means the oblique angles control the corner zones, while normal wind directions dominate the edge and interior. For example, it is observed from Figures 23, 26, and 29 that corner zones mainly correspond to the angles from $20^\circ - 70^\circ$, while Figures 24, 27, and 30 and Figures 25, 28, and 31 show that the normal wind directions are dominated by the edge and interior zones, respectively, for smaller tributary areas. In addition, the effects of tributary area are clearly seen on the critical wind directions from Figures 23 – 31. These figures indicate that larger tributary areas are primarily controlled by normal wind directions. Therefore, it can be concluded that critical wind directions of the corner zones are due to oblique angles, while for the edge and interior zones, normal wind directions are observed for smaller tributary areas.

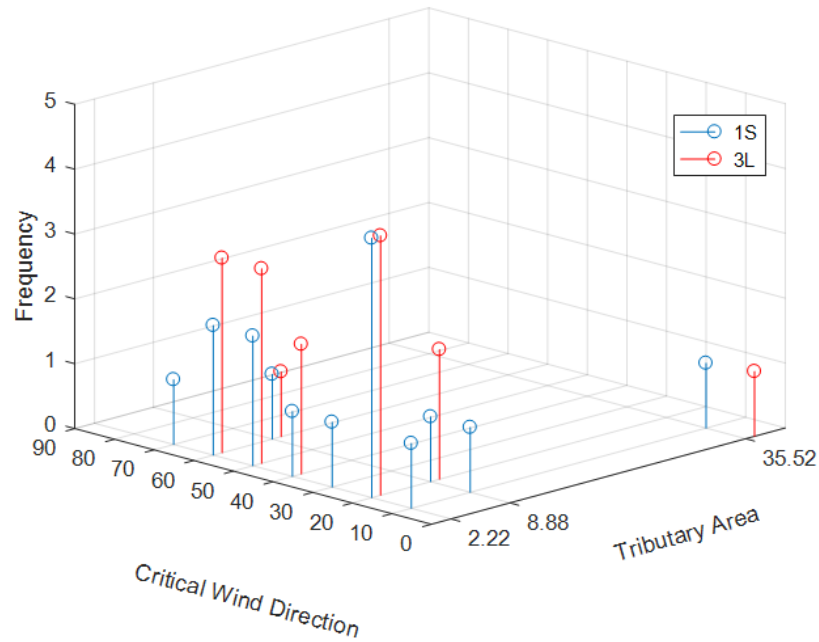


Figure 23: Critical wind directions for the worst GCp as a function of tributary area for corner zones of 1S B1H1 and 3L B1H1.

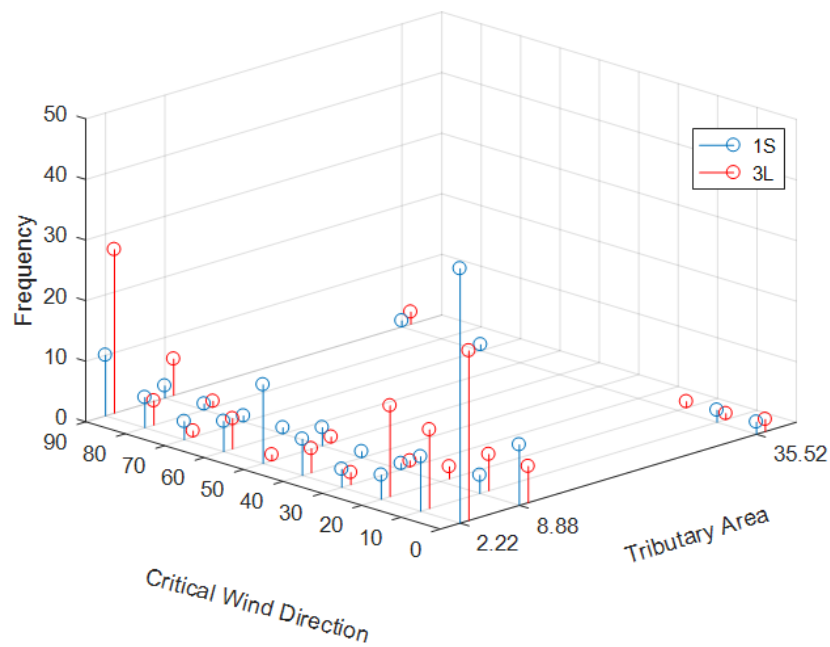


Figure 24: Critical wind directions for the worst GCp as a function of tributary area for edge zones of 1S B1H1 and 3L B1H1.

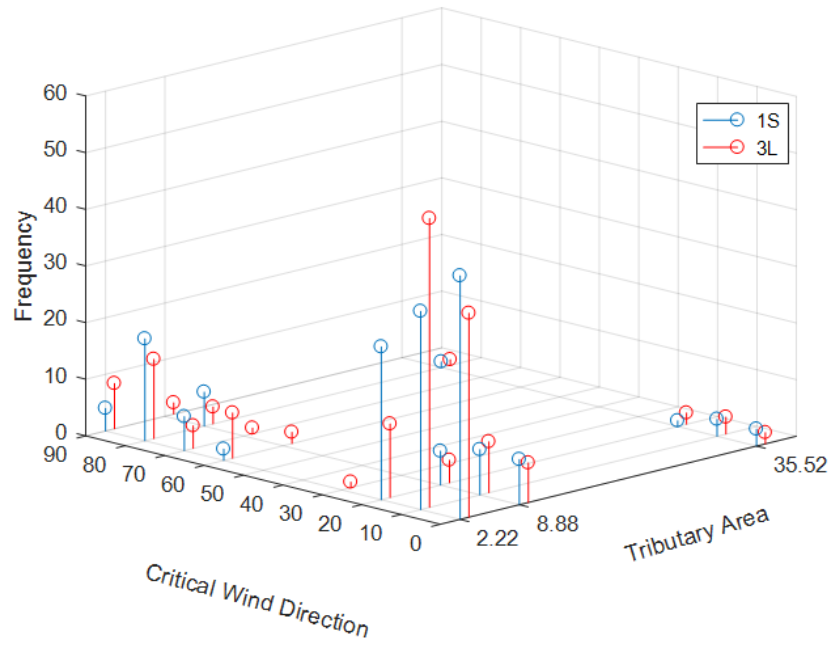


Figure 25: Critical wind directions for the worst GCp as a function of tributary area for interior zones of 1S B1H1 and 3L B1H1.

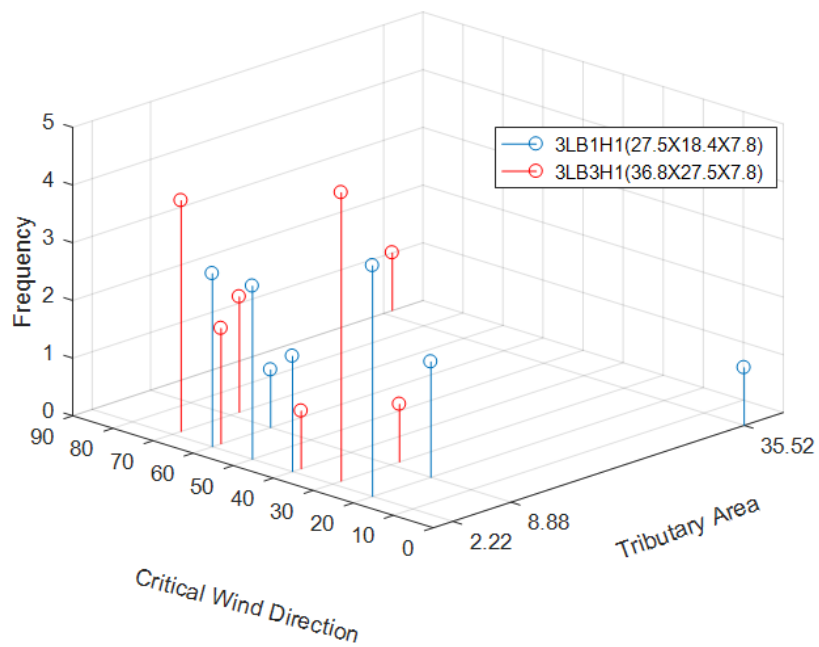


Figure 26: Critical wind directions for the worst GCp as a function of tributary area for corner zones of B1H1 and B3H1 in suburban terrain (3L).

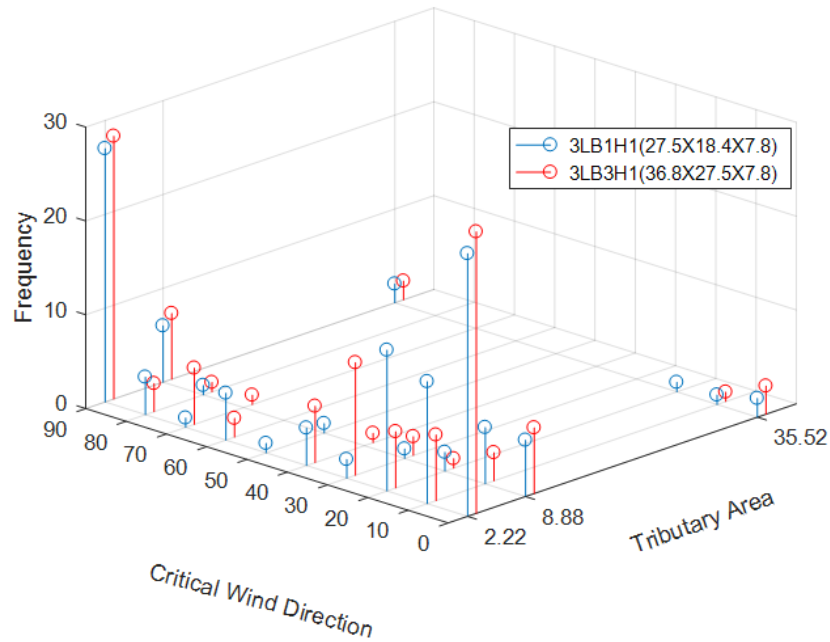


Figure 27: Critical wind directions for the worst GCp as a function of tributary area for edge zones of B1H1 and B3H1 in suburban terrain (3L).

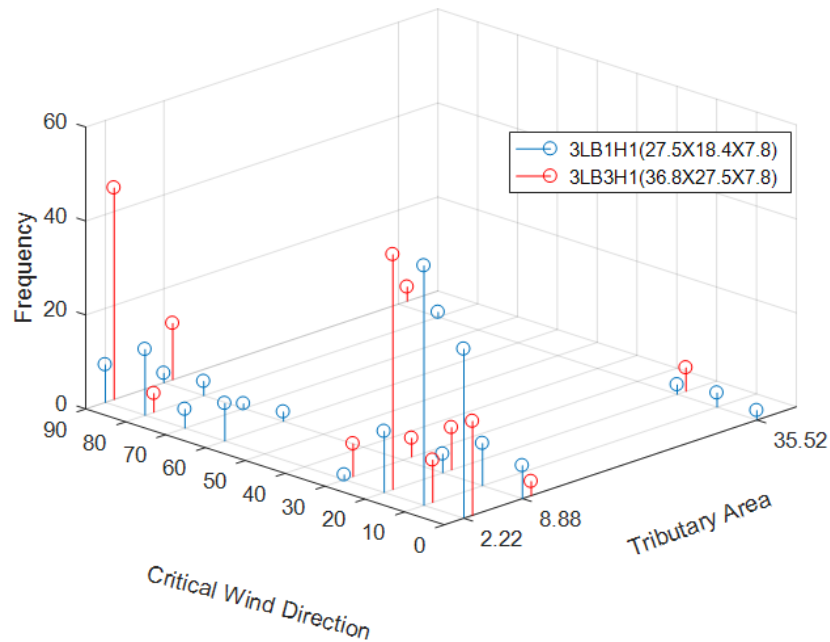


Figure 28: Critical wind directions for the worst GCp as a function of tributary area for interior zones of B1H1 and B3H1 in suburban terrain (3L).

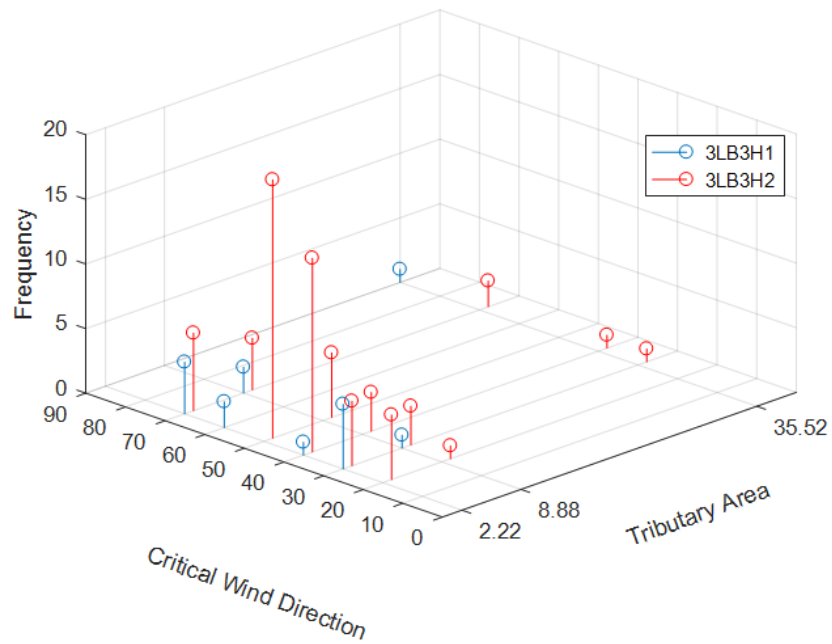


Figure 29: Critical wind directions for the worst GCp as a function of tributary area for corner zones of B3H1 and B3H2 in suburban terrain (3L).

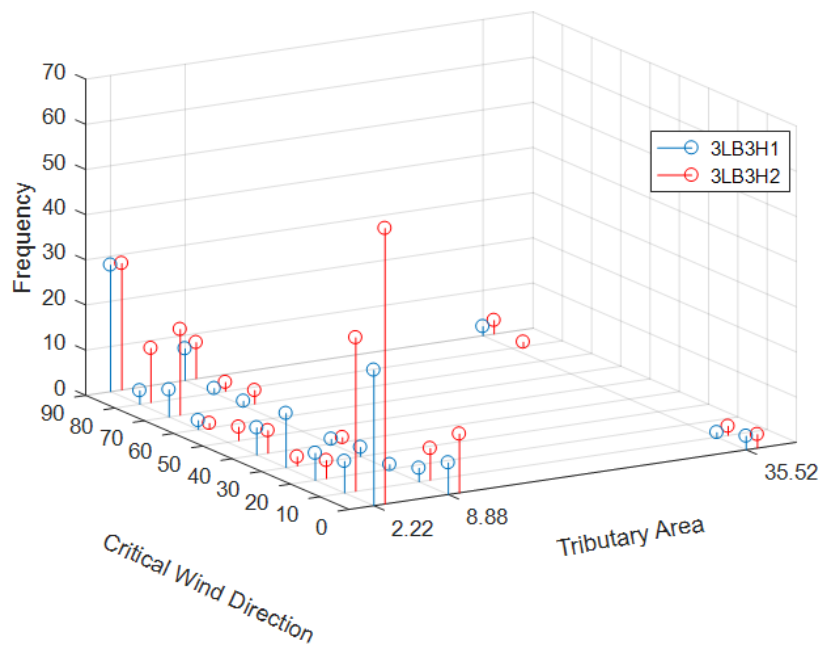


Figure 30: Critical wind directions for the worst GCp as a function of tributary area for edge zones of B3H1 and B3H2 in suburban terrain (3L).

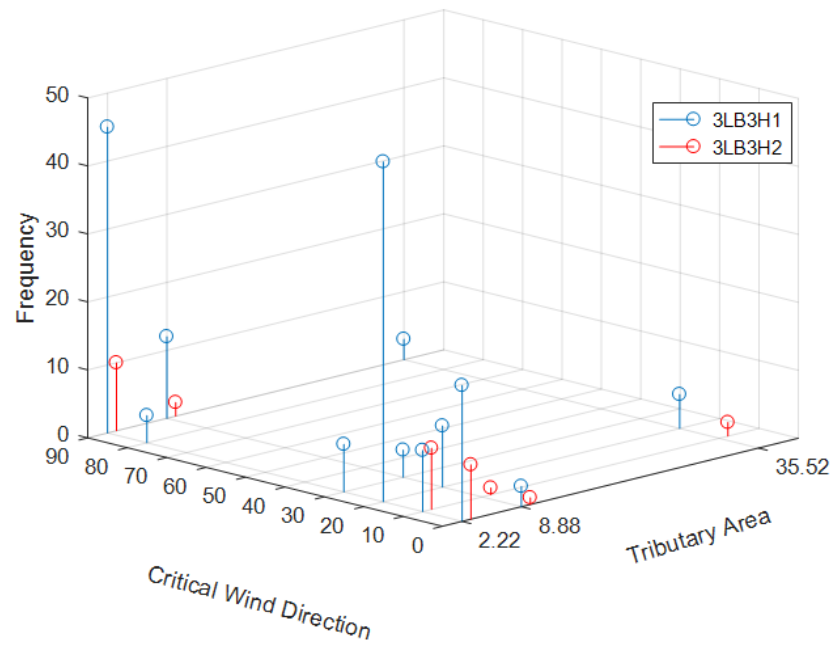


Figure 31: Critical wind directions for the worst G_{Cp} as a function of tributary area for interior zones of B3H1 and B3H2 in suburban terrain (3L).

3.2.2 Effects of Upstream Condition on Length of Corner Vortices for Fixed Geometries

Tests were carried out for six different upstream boundary layer conditions for all plan dimensions. The critical wind conditions for the 1S and 3L upstream conditions over the roof surfaces of B2H1 and B2H2 building models are plotted in Figure 32. It provides that corner vortex has an impact on the roofs for both cases. From the figure, it is clear that in case of flat terrain, corner vortices have the larger area on the corner of the roof surface among all angles of attack. But this effect becomes weaker in suburban terrain. It appears that this is mainly due to disruptions of the corner vortices under higher turbulence conditions since there are intermittent positions where the corner vortex controls. In any case, the critical wind direction clearly has greater variability under higher turbulence conditions. This effect is also observed for all other building models which are given in Appendix A. Moreover, it depicts that excluding the area of corner vortices, worst suction GC_p occurs along the longer wall at windward direction and it happens along the shorter wall at wind direction normal to the shorter one. This is also consistent with the results of Kopp and Morrison (2017), as they found that the critical wind directions are normal to the walls for open-country terrain. In addition, the zone controlled by the corner vortices are mainly due to the oblique angles over the roof corner. However, normal winds are important over the bulk of the roof for the building models shown in these figures.

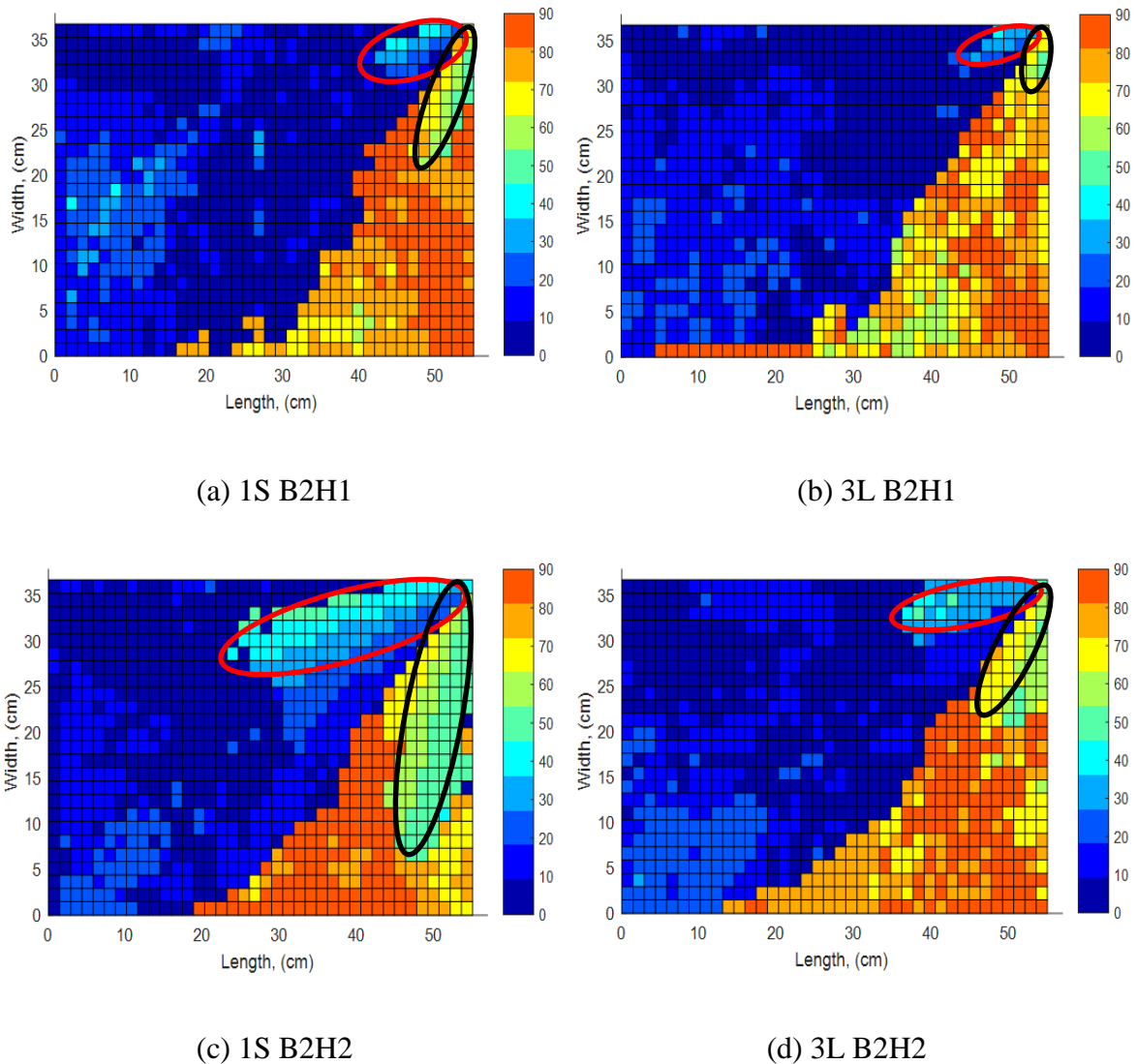


Figure 32: Critical wind directions over B2H1 and B2H2 models from 0 to 90 degree.

A typical figure of critical wind directions over the roof of Building 1 from 0° to 90° is shown in Figure 33. A non-overlapping square pattern of 2×2 taps was selected for all configurations. It can be seen that there are two regions where the corner vortices control the pressure distribution, which is mainly over the range from 30° to 60° . Although they are not elliptical in shape, for simplicity they are marked by two different

ellipses. The primary axis of the ellipse along the long wall is denoted by L1, while it is L2 for shorter wall. Here, in order to investigate the influence of critical wind direction, they are measured by the primary axes L1 (longer wall) and L2 (shorter wall) for wind directions over the range of angles of attack from 30° to 60° . The lengths of the primary axes are measured geometrically by the number of squares and the angle with the corresponding wall. Table 6 shows the lengths (L1 and L2) for all configurations, as measured in this way.

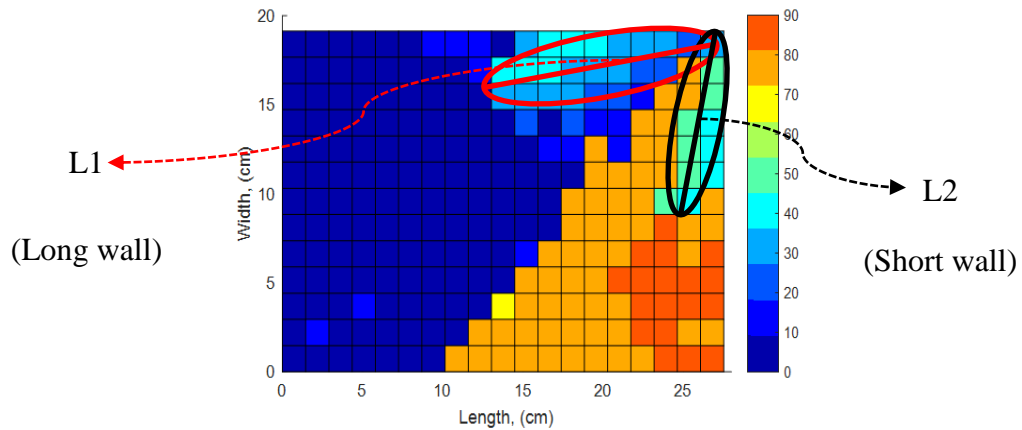


Figure 33: Critical wind directions for the 3S upstream condition on Building 1 (H2).

Table 6: Different lengths of critical wind directions for all cases.

Building (L x W) (cm)	Upstream Conditions	Height, H ₁ (7.8 cm)		Height, H ₂ (23.4 cm)	
		L1 cm (Longer)	L2 cm (Shorter)	L1 cm (Longer)	L2 cm (Shorter)
Building 1 (27.5 x 18.4)	1S	15.00	18.80	24.00	15.66
	1L	15.00	18.10	23.40	15.66
	2S	15.00	17.70	22.20	14.00
	2L	15.00	11.96	21.73	13.71
	3S	13.40	10.50	15.90	10.67
	3L	13.40	10.50	15.41	10.67
Building 2 (55 x 36.8)	1S	14.38	17.23	36.79	32.89
	1L	14.38	17.23	36.79	31.33
	2S	12.78	15.00	35.00	29.76
	2L	12.78	15.00	35.00	28.19
	3S	11.20	13.30	23.40	17.94
	3L	11.20	6.00	21.74	17.00
Building 3 (27.5 x 36.8)	1S	N/A	N/A	28.42	26.63
	1L	18.39	17.84	26.00	25.00
	2S	N/A	N/A	25.00	23.50
	2L	18.39	17.00	23.40	21.90
	3S	N/A	N/A	22.00	18.70
	3L	16.72	9.35	21.73	18.70
Building 4 (55 x 18.4)	1S	N/A	N/A	32.36	19.00
	1L	19.23	22.10	32.36	18.28
	2S	N/A	N/A	30.81	16.76
	2L	16.72	21.25	28.50	16.76
	3S	N/A	N/A	27.73	14.20
	3L	13.38	20.39	21.57	13.71

Figures 34, 36, 38, and 40 represent the lengths, L1 and L2 normalized by corresponding height with respect to turbulence intensity for building models 1, 2, 3, and 4, while they are normalized by corresponding wall area, $A^{1/2}$, where $(LH)^{1/2}$ for longer wall or $(WH)^{1/2}$ for shorter wall in Figure 35, 37, 39, and 41. All figures depict that there is a gradual decrease in the lengths, L1 and L2 from flat terrain to suburban terrain for each plan shape and height. It is also observed that lengths normalized by wall area ($A^{1/2}$) are less scattered than those of height (H) for all building models. As a result, one can conclude from these figures that, corner vortex is larger in flat terrain, while it is smaller in suburban terrain, irrespective of the plan dimensions and building heights. Also, wall area is more important than height in controlling the length of corner vortices.

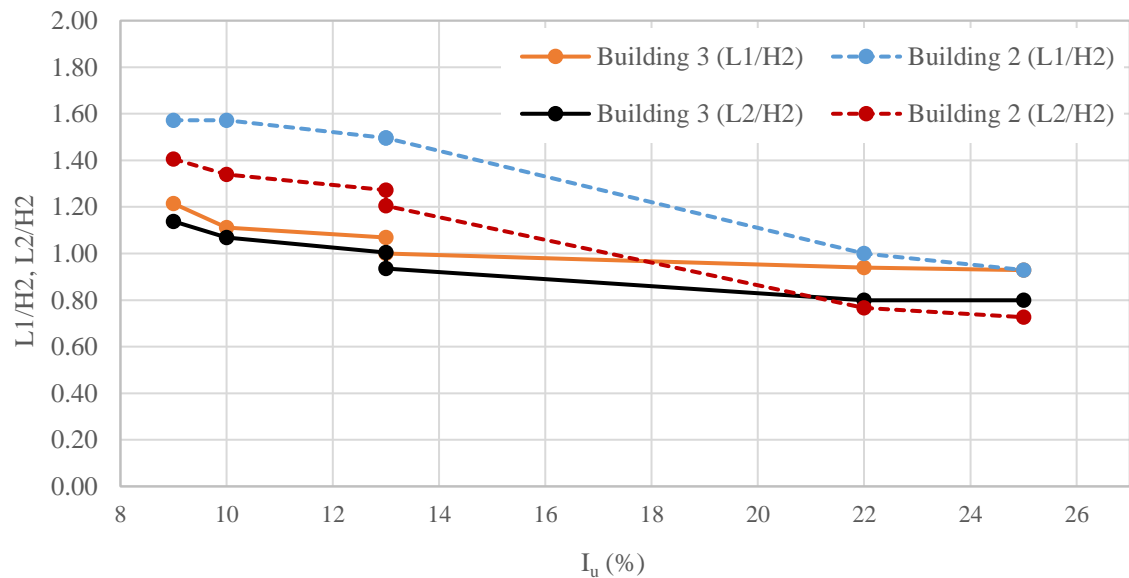


Figure 34: Effect of turbulence intensity on L1 and L2 (normalized by height) for B2H2 and B3H2.

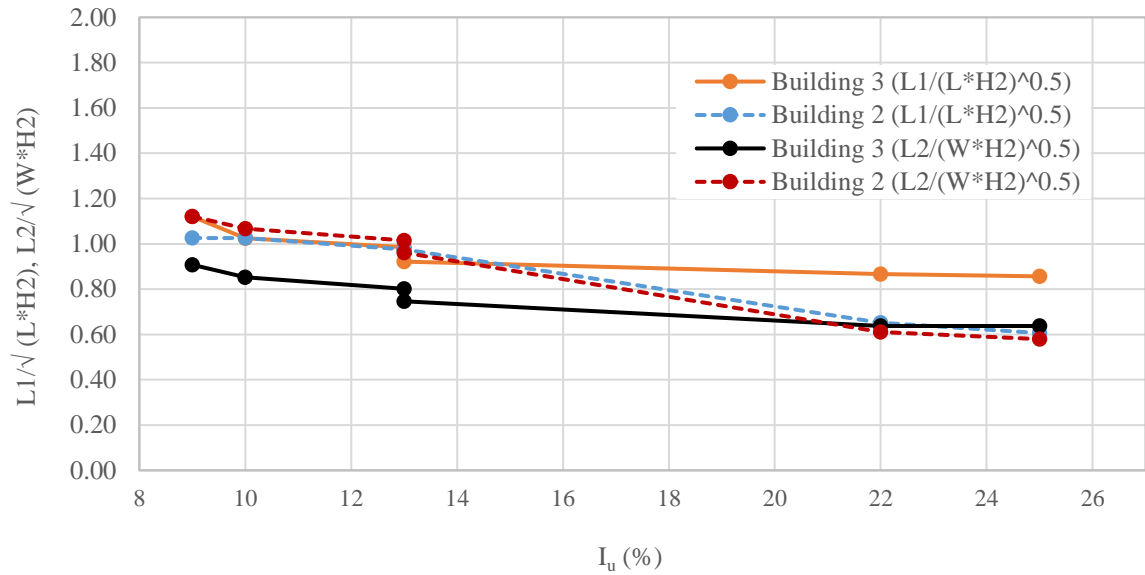


Figure 35: Effect of turbulence intensity on L1 and L2 (normalized by $\sqrt{\text{Area}}$) for B2H2 and B3H2.

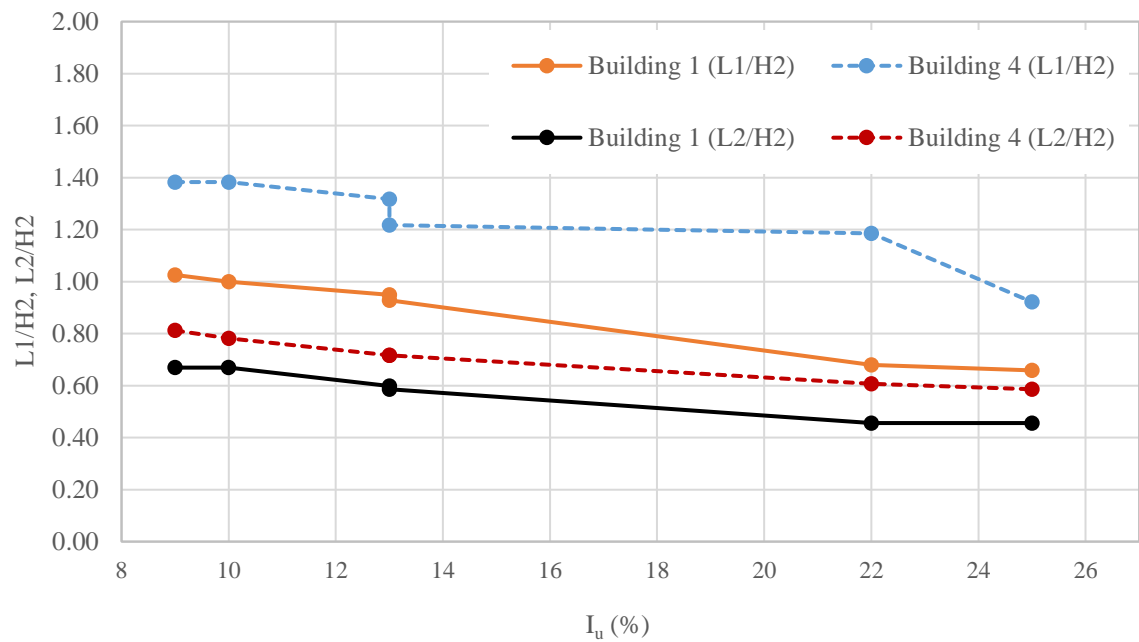


Figure 36: Effect of turbulence intensity on L1 and L2 (normalized by height) for B1H2 and B4H2.

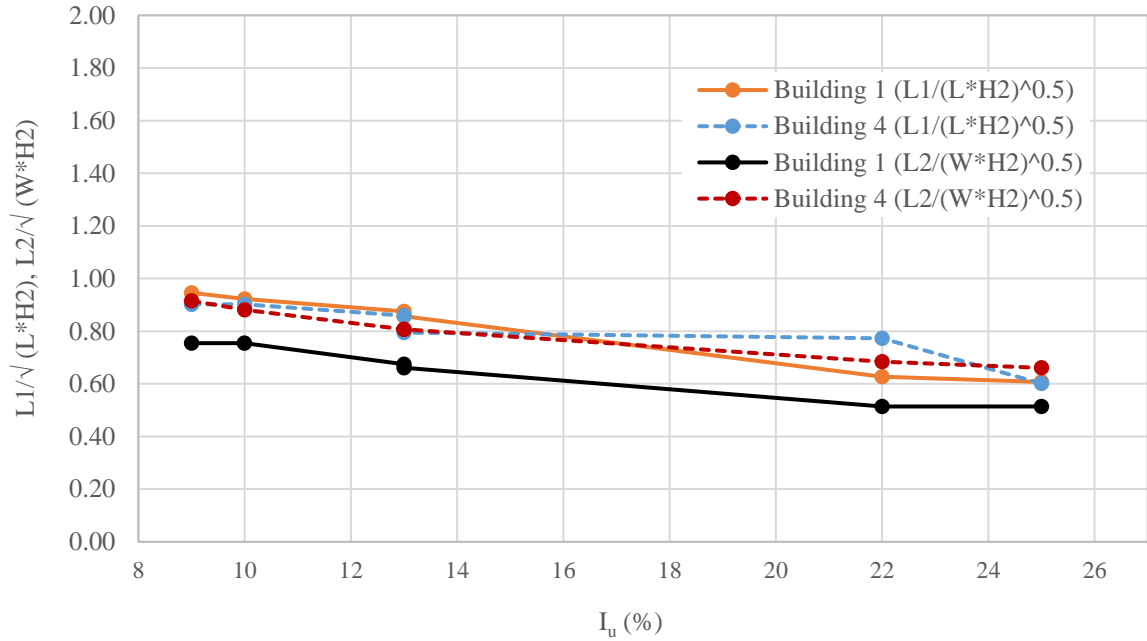


Figure 37: Effect of turbulence intensity on L1 and L2 (normalized by $\sqrt{\text{Area}}$) for B1H2 and B4H2.

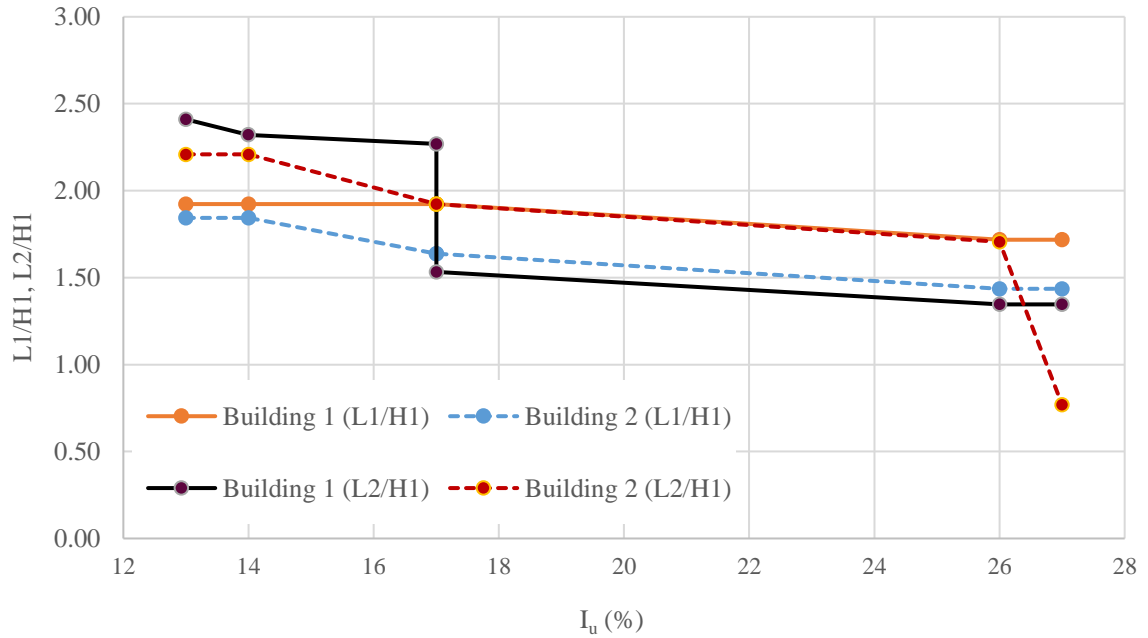


Figure 38: Effect of turbulence intensity on L1 and L2 (normalized by height) for B1H1 and B2H1.

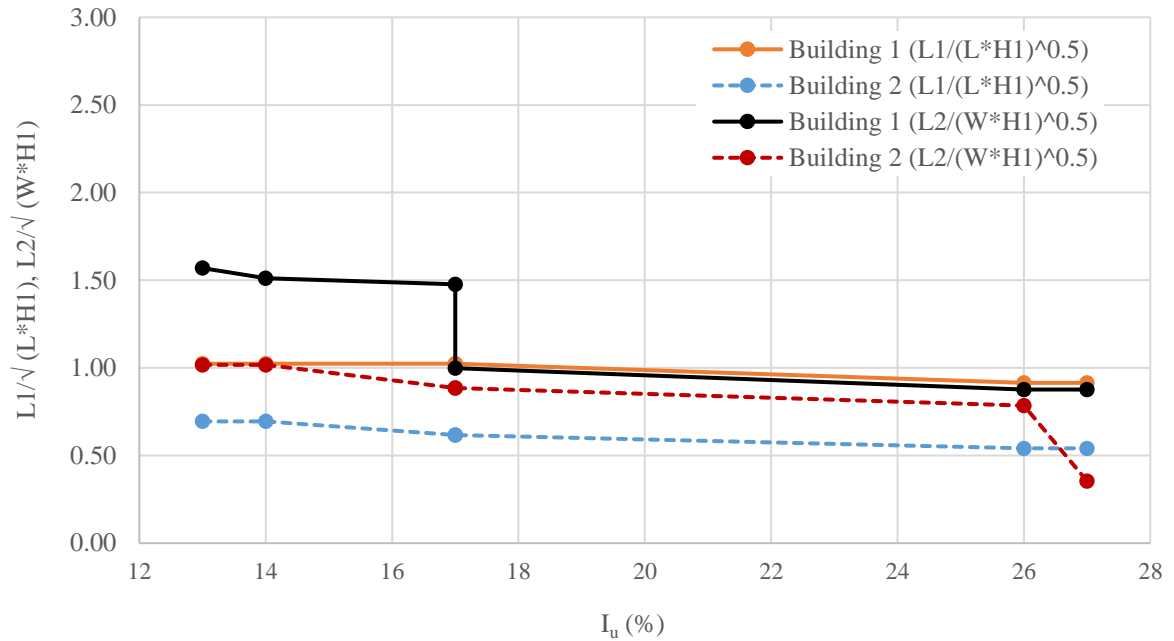


Figure 39: Effect of turbulence intensity on L1 and L2 (normalized by $\sqrt{\text{Area}}$) for B1H1 and B2H1.

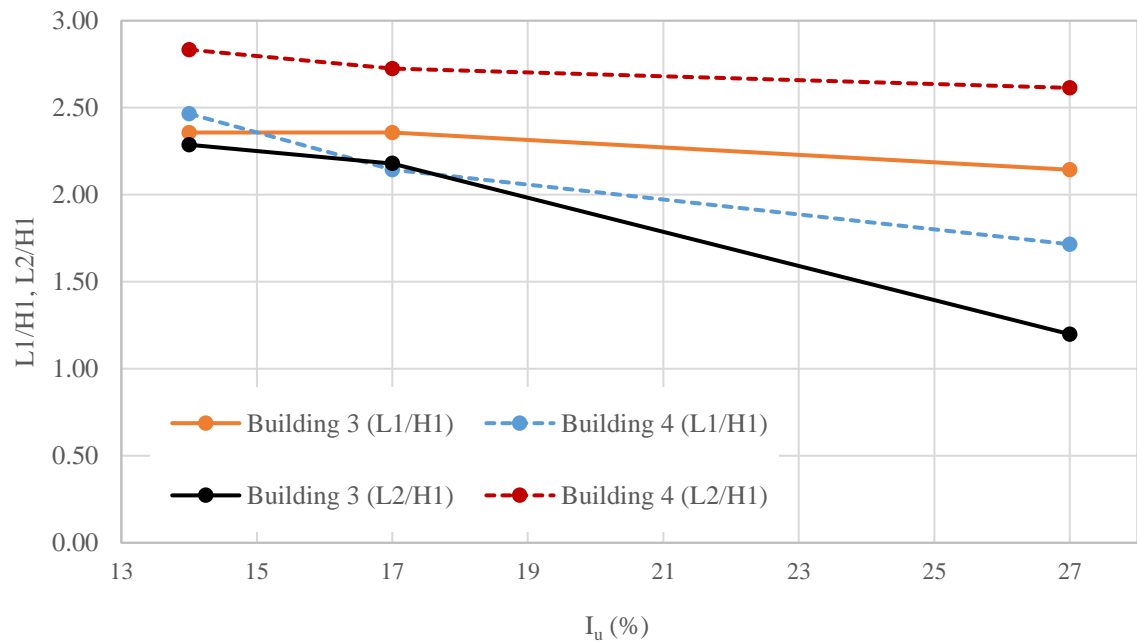


Figure 40: Effect of turbulence intensity on L1 and L2 (normalized by height) for B3H1 and B4H1.

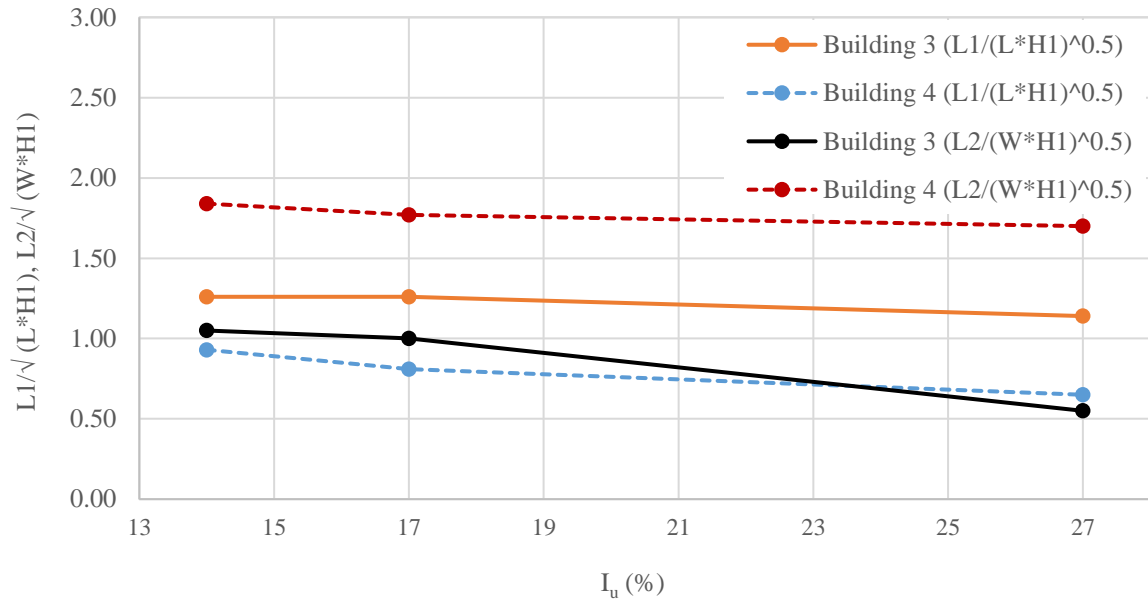


Figure 41: Effect of turbulence intensity on L1 and L2 (normalized by $\sqrt{\text{Area}}$) for B3H1 and B4H1.

3.2.3 Effects of Building Height on Length of Corner Vortices

As described earlier, data were taken for two different heights for four different building models. Height is a significant parameter for wind loads on low-rise building roofs, as shown by Kopp and Morrison (2017). Effects of height are also examined in this study. Figure 42 shows the lengths of primary axis of ellipses along the long walls for two different heights and 1L and 3L upstream conditions of all models. It indicates that the length of the elliptical shape is dependent on building height. It is observed that the length is larger for higher buildings when compared to smaller ones for each cases. Here, for height H_2 , building models B1 and B4 are not low-rise, but mid-rise buildings. It is well known that aerodynamics are different for low-rise, mid-rise, and high-rise buildings. If a building is smaller than cube in height, then it can be considered as a low-

rise building. Wind causes higher pressures on the roofs for low-rise buildings than side walls, while it has a greater effect on the side walls for mid-rise and high-rise buildings than the roofs. The slopes are higher for flat terrain than suburban one. Thus, based on the figure, it can be easily concluded that the length of corner vortex influence is larger for higher buildings along the longer wall for both low-rise and mid-rise building, irrespective of plan shape.

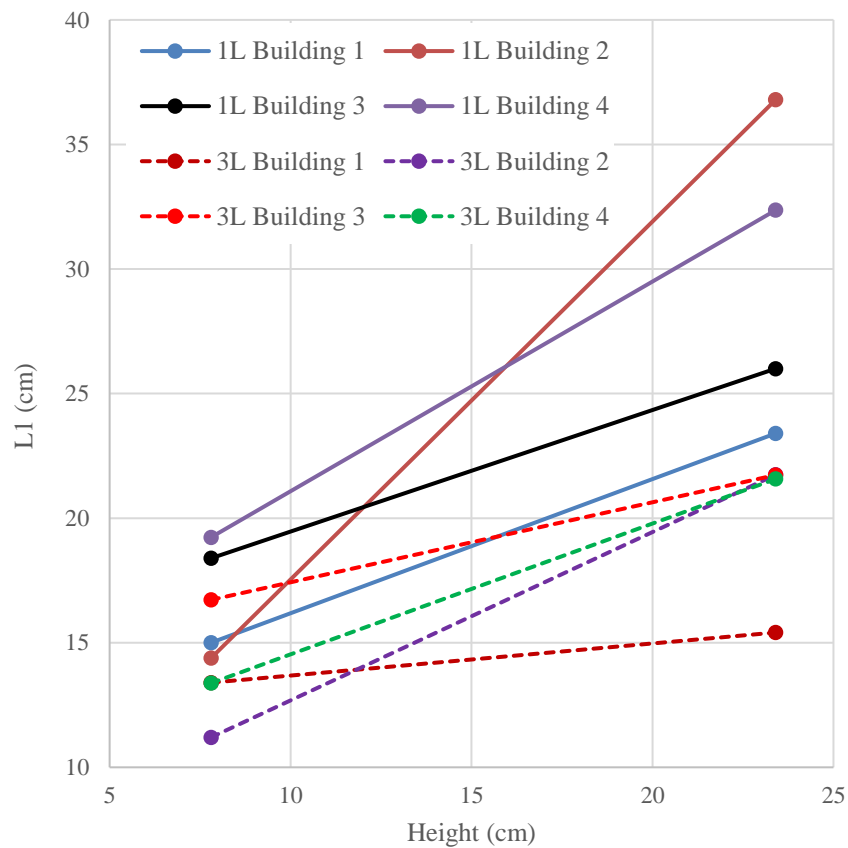


Figure 42: Effect of height on critical wind directions for windward wall of all buildings.

The lengths of the primary axis of the ellipses along the shorter walls for two different heights and 1L and 3L upstream conditions for all models are shown in Figure

43. One can see that the length of the elliptical shape follows an increasing trend for buildings 2 and 3, while it decreases for buildings 1 and 4 from lower to higher heights. This decreasing trend may happen due to mid-rise building effects along the shorter side of both buildings 1 and 4 (same width). That means the length of corner vortices along the shorter wall depends on the building size and the length of shorter wall. As a consequence, it is observed that L2 increases with height for low-rise building, while it decreases for the transmission from low-rise to mid-rise.

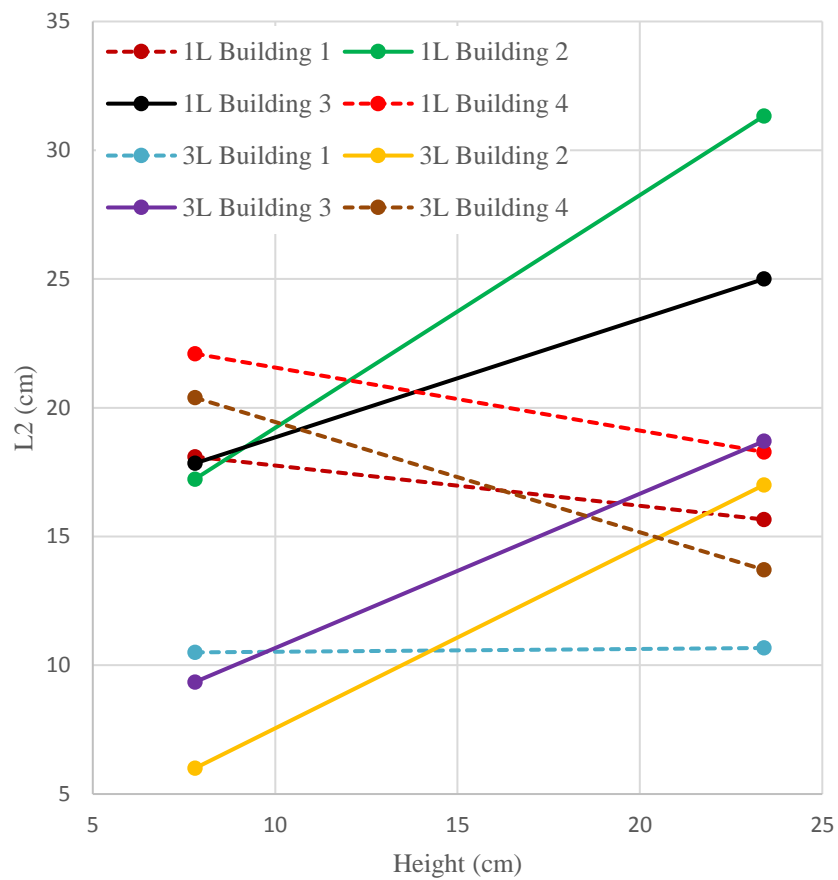


Figure 43: Effect of height on critical wind directions for side wall of all buildings.

3.3 Worst (Enveloped) GCp Values

Figures 44(a) and 44(b) depict the critical wind directions, while Figures 44(c) and 44(d) show the worst area-averaged pressure coefficients (GCp) over the roof surface of B1H1 for both flat (1S) and suburban (3L) terrain. In these figures, white dashed lines are drawn after the corner zones from the edge for 0° and 90°, while red dashed lines are from the corner at an angle of 40° and 60° along longer and shorter wall, respectively. These four angles are chosen from the figures of critical wind direction (44a, and 44b), in which the largest GCp occurs for the edge and corner zones. It is clear that terrain has an impact on the worst GCp. Figure 44(c), and 44(d) indicate that pressure coefficients are larger for suburban terrain compared to flat one, although this is likely an effect of integral scales (Akon, 2017). It should be noted that Kopp and Morrison (2017) found that terrain is not a significant parameter for the pressure coefficients, as both the magnitude of GCp and the spatial distribution were similar for open and suburban terrain although these experiments were conducted at fixed integral scales.

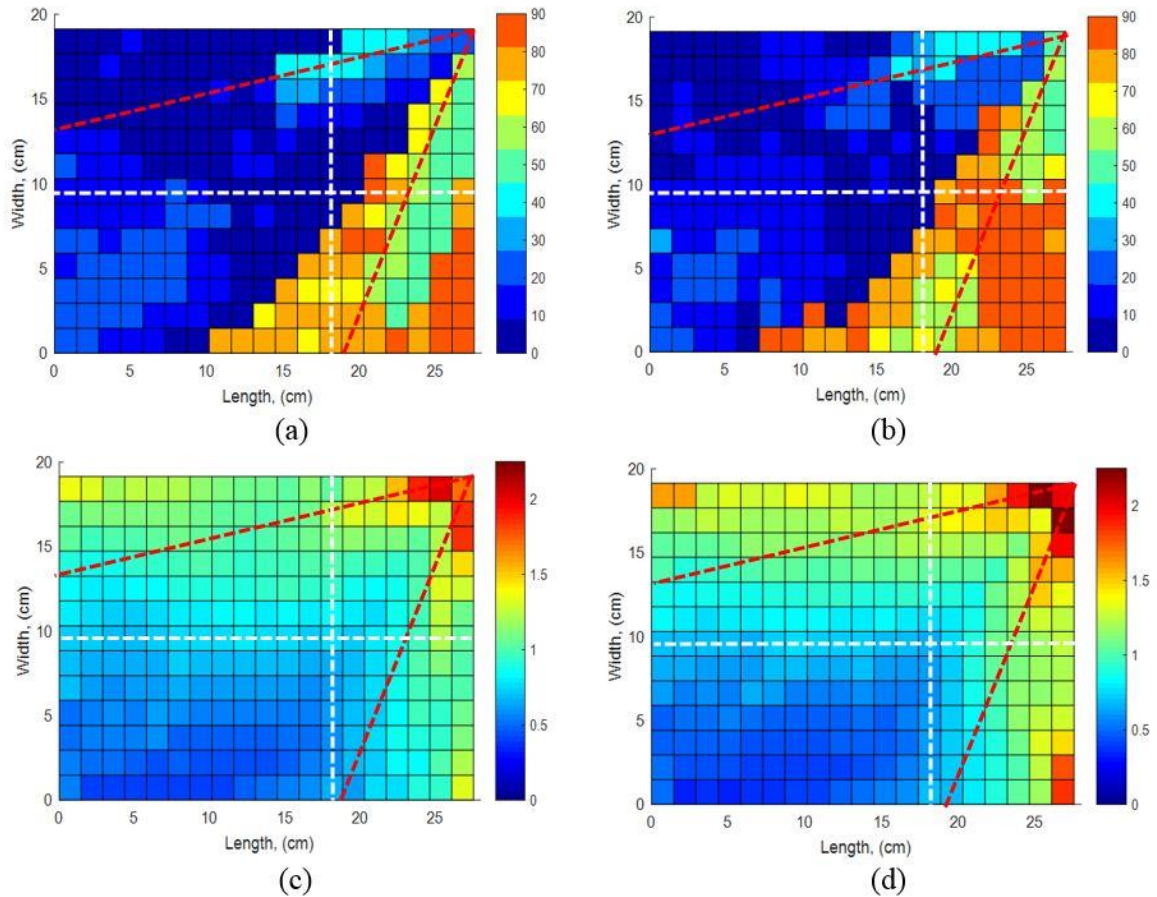


Figure 44: Critical wind directions: (a), and (b), and worst GCp: (c), and (d) over B1H1 for flat (1S), and suburban (3L) terrain, respectively.

To better understand the effects of terrain on worst GCp, comparisons of GCp value between flat (1S) and suburban (3L) terrain with respect to the distance from the edge and corner for particular wind directions (i.e., 0° , 90° , 40° , and 60°), are shown in Figures 45 and 46, respectively. One can see that pressure coefficients vary with these terrains, in both figures. Figure 45 indicates that for normal wind directions (i.e. 0° , 90°), pressure coefficients along the white lines in Figure 44 are larger in suburban terrain compared to flat terrain near the leading edge, while they are smaller at the trailing edge. In addition, for oblique wind directions (i.e. 40° , 60°), it is seen that higher GCp values

occur in suburban terrain than in flat terrain from Figure 46. Based on this, it can be concluded that surface pressure coefficients depends on the terrain condition and suburban (3L) terrain corresponds to higher suction G_{Cp} than flat terrain (1S) near the leading edge for both normal and oblique wind directions.

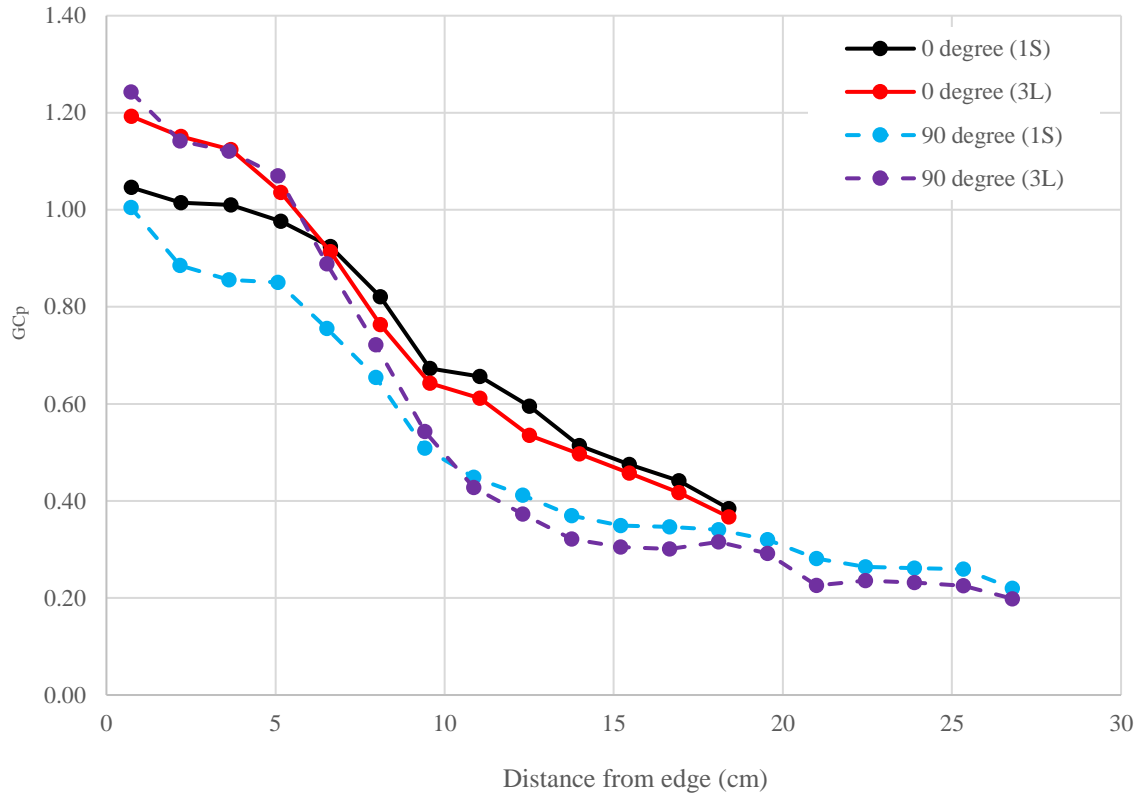


Figure 45: Comparison of worst G_{Cp} over B1H1 vs. distance from the edge for 0° and 90° between flat and suburban terrain.

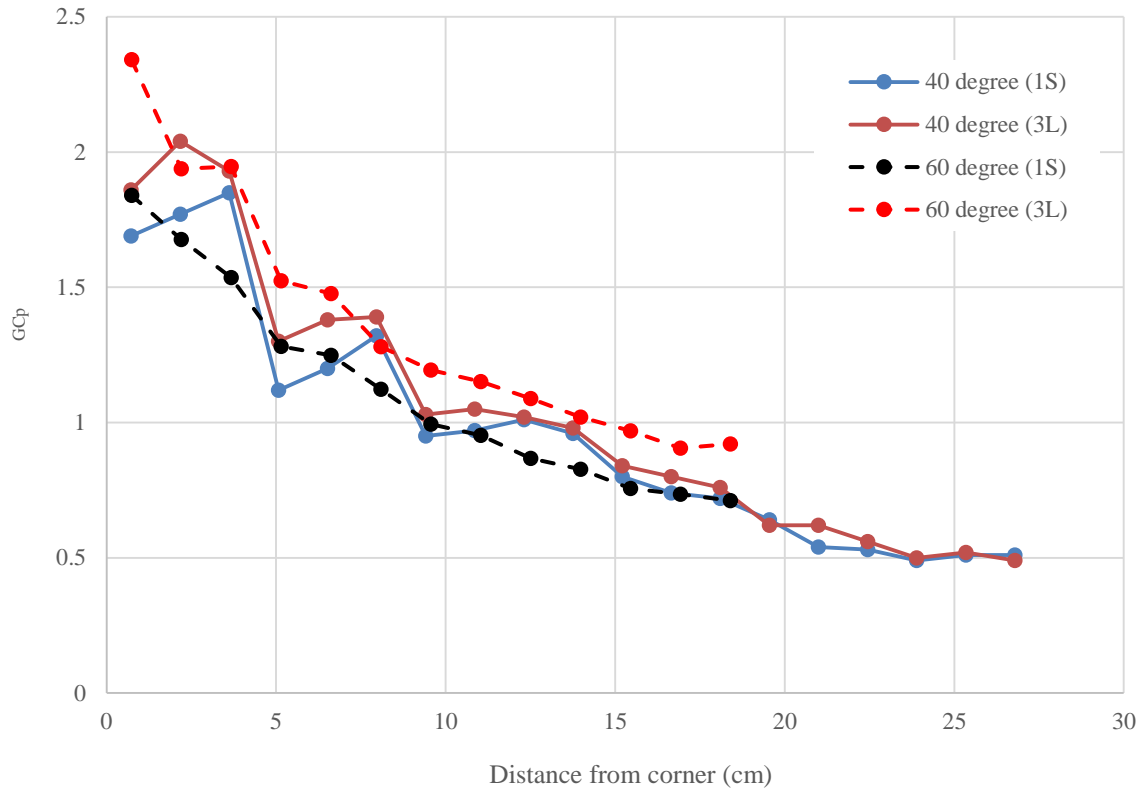


Figure 46: Comparison of worst GCP over B1H1 vs. distance from the corner for 40° and 60° between flat and suburban terrain.

Now, the suction pressure coefficients are compared for two different plan dimensions. A non-overlapping square pattern 2x2 was selected for all configurations that means each area-averaged GCP corresponds to four pressure taps in every square on the roof surface. In order to compare all the building models, a range from 0 to 3.9 is chosen for the suction GCP on the same scale.

Figure 47 indicates the worst suction GCP values enveloped over all wind directions on the roof surfaces of B1H1 and B2H2 model for 1S and 1L upstream boundary layer conditions. One can see that the area-averaged pressure coefficients are dependent on turbulence length scales. The magnitude of suction GCP is higher in case of

1L than 1S for both building models. It also depicts that peak pressure coefficients vary not only in the magnitude but also in the spatial patterns with respect to turbulence length scale. These can be concluded for all other building models which are shown in the Appendix B.

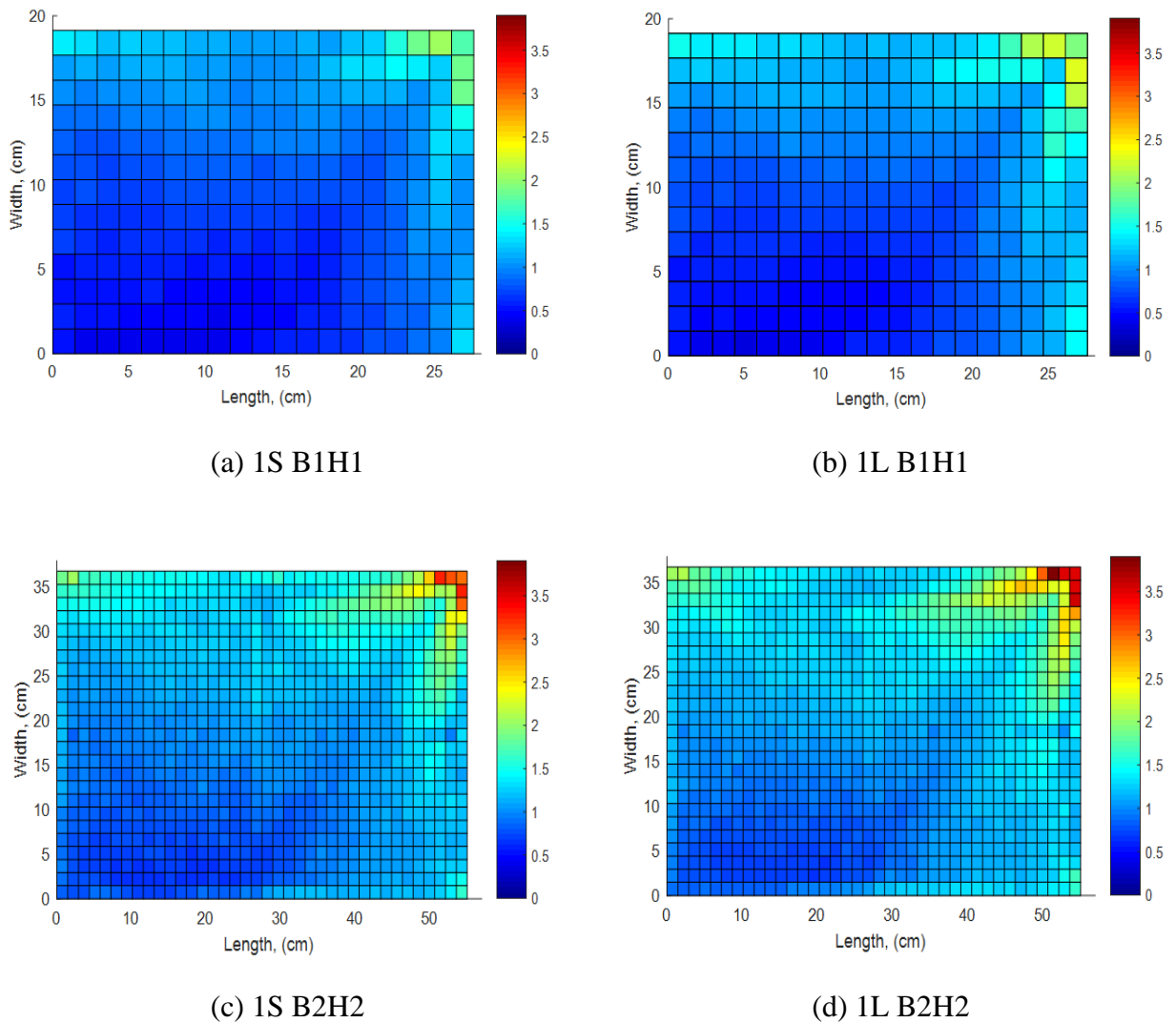


Figure 47: Comparison of worst suction GC_p over B1H1 and B2H2 models for different length scales.

Figure 48 shows the suction pressure coefficients, GC_p on the roof of B1H1 and B2H2 buildings for suburban terrain (3L). Here, the magnitude of suction pressures are

compared between lower and higher buildings from figure 47(a) and 47(c), and 48(a) and 48(b) for both flat (1S) and suburban (3L) terrain, respectively. It can easily be concluded that the areas of the roof surface having larger suction pressure coefficients are larger for higher buildings than that of lower ones for both flat and suburban terrains. This conclusion is also consistent with the result shown by Kopp and Morrison (2017). Moreover, if the value of suction G_{Cp} is compared between figure 47(a) and 48(a), and 47(c) and 48(b) for same plan dimension B1H1 and B2H2, respectively, pressure coefficients increase from flat (1S) to suburban (3L) terrain for lower buildings, while they decrease for higher buildings. This is true for all other plan shapes which are given in the Appendix B.

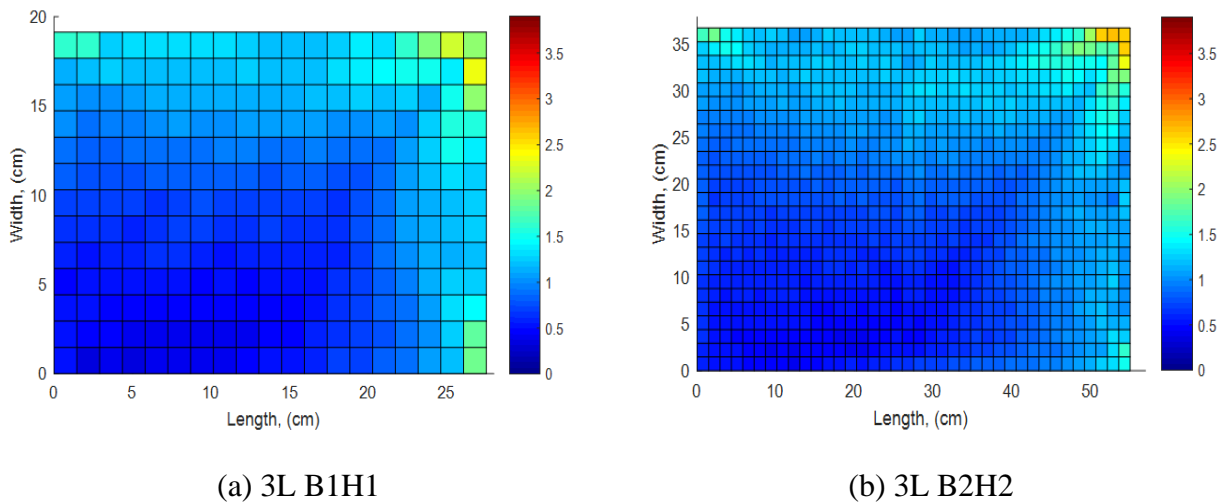


Figure 48: Comparison of worst suction G_{Cp} over B1H1 and B2H2 models for the same terrain.

3.4 Discussion

Considering the results described in the earlier sections, it can be concluded that corner vortices on the roof surface of three-dimensional bluff bodies depend on upstream boundary layer flows as well as building height. The results indicate that corner vortex has larger area on the roof surface in flat terrain, while this impact decreases in suburban terrain for all plan shapes. In addition, it is observed that except the corner vortices, worst GC_p occurs along the longer wall at windward direction and it happens along the shorter wall at wind direction normal to the shorter one.

From the figures of the section 3.2.1, one can see that critical wind directions vary with upstream boundary layer conditions. In addition, height plays a vital role on the size of roof zones for the critical wind directions. Figures provides that larger corner zones are found for the higher buildings compared to the smaller ones. It is also seen that plan dimension has a limited effect on the size of roof zones. For smaller tributary areas, the critical wind directions for the corner zones belong to the oblique wind directions, while the edge and interior zones primarily depend on the normal wind directions. Moreover, critical wind directions for the larger tributary areas are observed for normal wind directions.

In this analysis, the lengths of corner vortices for both longer and shorter wall were normalized by the corresponding wall area and height in the section 3.2.2. When the figures of these two cases with respect to turbulence intensity were compared, it is observed that wall area is more correlated than height. Therefore, wall area is a significant parameter in the formation of corner vortices.

In addition, from these figures of the length of critical wind directions versus turbulence intensity, one can see that the length of L1 along the longer wall increases with height for all the building models, i.e., low-rise and mid-rise buildings. However, the length of L2 along the shorter wall increases with height for low-rise buildings, while it decreases for mid-rise buildings.

From section 3.3, it can be seen that area-averaged surface pressure coefficients (GC_p) depend on the terrain condition (i.e., turbulence level). Near the leading edge, higher values of the enveloped suction coefficients, GC_p , are observed in suburban terrain (3L) compared to the flat (1S) one for both oblique and normal wind directions. Here, larger integral length scales tend to lead to larger values of peak pressure, GC_p than smaller integral length scales. In addition, GC_p values changes in the magnitude and spatial pattern for different integral length scales. Moreover, from all configurations, it can be concluded that larger peak suctions are observed for higher buildings compared to smaller ones.

Chapter 4

4 Conclusions and Recommendations

4.1 Conclusions

Surface pressure coefficients and wind speed data were taken to obtain the effects of turbulence levels in the terrain simulations on the pressure coefficients of low-rise building roofs. Area-averaged pressure coefficients were examined from high-resolution pressure measurements in a boundary layer wind tunnel for eight building geometries. Based on the results shown in the earlier chapters, the following conclusions can be made:

- In lower turbulence levels, corner vortices have larger area over the roof surface among all angles of attack, whereas this effect is shortened in higher turbulence levels, irrespective of the plan dimensions and building heights. Outside of the regions where corner vortices dominate, worst pressure coefficients GC_p occur for the wind directions normal to the wall.
- Terrain condition or turbulence level plays a vital role on the critical wind directions over the roof surface. In addition, the size of corner zones on the roof surface increase with height, while plan dimension has a limited effect on the zone size. The critical wind directions for the corner zones are oblique angles, while they are normal wind directions for the edge and interior zones in case of smaller tributary areas. However, normal wind directions dominate for larger tributary areas over the entire roof surface.

- The size of corner vortex along the longer wall increases with building height for both low-rise and mid-rise buildings. The size of the corner vortex also increases with building height along the shorter wall for low-rise buildings, while it decreases in size for mid-rise buildings. By normalizing the length of the corner vortices by wall area and height, it is found that wall area is a better scaling parameter than the height.
- Area-averaged peak pressure coefficient, GC_p is more sensitive to turbulence length scale than the turbulence intensity. In addition, GC_p varies not only in the magnitude but also in the spatial patterns with respect to turbulence length scale. Moreover, higher buildings have larger area of higher suction pressure coefficients than that of lower ones, which is well captured by the recent modified zone sizes in ASCE 7 – 16 (2017).

4.2 Recommendations

According to the results obtained from this analysis, several recommendations can be made which are given in the following:

- For some cases, the length of corner vortices exceeded from the main block to the dummy block, especially for building models B3 and B4 in this study. Therefore, the entire range of wind direction should be chosen carefully so that the corner vortex can be measured properly.

- The geometric effects obtained from the current building models were somewhat unexplained. To resolve the effects of aspect ratio, geometric scale of the models should be same.
- If the tributary area is varied, then its impact on corner vortices could be analyzed, which might be important for determining the roof zones.
- Based on the results of the spectra and worst suction GC_p from this study, the scaling parameter can be obtained to resolve the issue of matching turbulence intensity and spectra between the model-scale and full-scale.

References

- Akon, A. F., & Kopp, G. A. (2016). Mean pressure distributions and reattachment lengths for roof-separation bubbles on low-rise buildings. *Journal of Wind Engineering and Industrial Aerodynamics*, *155*, 115–125.
- Akon, A. F. (2017). Effects of turbulence on the separating-reattaching flow above surface-mounted, three-dimensional bluff bodies. PhD Thesis, The University of Western Ontario, London, Ontario, Canada.
- Alrawashdeh, H., & Stathopoulos, T. (2015). Wind pressures on large roofs of low buildings and wind codes and standards. *Journal of Wind Engineering and Industrial Aerodynamics*, *147*, 212–225.
- ASCE. (2010). Minimum design loads for buildings and other structures. ASCE 7-10, Reston, VA.
- ASCE. (2017). Minimum design loads for buildings and other structures. ASCE 7-16, Reston, VA.
- Asghari-Mooneghi, M., Irwin, P., & Chowdhury, A. G. (2016). Partial turbulence simulation method for predicting peak wind loads on small structures and building appurtenances. *Journal of Wind Engineering and Industrial Aerodynamics*, *157*, 47–62.
- Banks, D., Meroney, R. N., Sarkar, P. P., Zhao, Z., & Wu, F. (2000). Flow visualization of conical vortices on flat roofs with simultaneous surface pressure measurement. *Journal of Wind Engineering and Industrial Aerodynamics*, *84*, 65–85.
- Banks, D., & Meroney, R. N. (2001b). A model of roof-top surface pressures produced by conical vortices: Model development. *Wind and Structures*, *4*(3).
- Banks, D. (2013). The role of corner vortices in dictating peak wind loads on tilted flat solar panels mounted on large, flat roofs. *Journal of Wind Engineering and Industrial Aerodynamics*, *123*, 192–201.
- Banks, D. (2017). Personal communication.
- Bienkiewicz, B., & Sun, Y. (1992). Local wind loading on the roof of a low-rise building. *Journal of Wind Engineering and Industrial Aerodynamics*, *45*(1), 11–24.
- Browne, M. T. L., Gibbons, M. P. M., Gamble, S., & Galsworthy, J. (2013). Wind loading on tilted roof-top solar arrays: The parapet effect. *Journal of Wind Engineering and Industrial Aerodynamics*, *123*, 202–213.
- Case, P. C., & Isyumov, N. (1998). Wind loads on low buildings with 4:12 gable roofs in open country and suburban exposures. *Journal of Wind Engineering and Industrial Aerodynamics*, *77–78*, 107–118.

- Castro, I. P., & Robins, A. G. (1977). The flow around a surface-mounted cube in uniform and turbulent streams. *Journal of Fluid Mechanics*, 79, 307–335.
- Cook, N. J., & Mayne, J. R. (1979). A novel working approach to the assessment of wind loads for equivalent static design. *Journal of Wind Engineering and Industrial Aerodynamics*, 4(2), 149–164.
- Hillier, R., & Cherry, N. J. (1981). The effects of stream turbulence on separation bubbles. *Journal of Wind Engineering and Industrial Aerodynamics*, 8(1–2), 49–58.
- Holmes, J. D., & Carpenter, P. (1990). The effects of Jensen number variations on the wind loads on a low-rise building. *Journal of Wind Engineering and Industrial Aerodynamics*, 36, 1279–1288.
- Ho, T.C.E., Surry, D., Morrish, D., & Kopp, G.A. (2005). The UWO contribution to the NIST aerodynamic database for wind loads on low buildings: Part 1. Archiving format and basic aerodynamic data. *Journal of Wind Engineering and Industrial Aerodynamics*, 93, 1–30.
- Irwin, P. A. (2008). Bluff body aerodynamics in wind engineering. *Journal of Wind Engineering and Industrial Aerodynamics*. 96, 701-712.
- IntraRisk: Applied Research Associates, Inc. Development of Loss Relativities for Wind Resistive Features of Residential Structures. North Carolina, March 2002.
- Kim, K. C., Ji, H. S., & Seong, S. H. (2003). Flow structure around a 3-D rectangular prism in a turbulent boundary layer. *Journal of Wind Engineering and Industrial Aerodynamics*, 91(5), 653–669.
- Kopp, G. A., Mans, C., & Surry, D. (2005). Wind effects of parapets on low buildings: Part 4. Mitigation of corner loads with alternative geometries. *Journal of Wind Engineering and Industrial Aerodynamics*, 93, 873–888.
- Kopp, G. A., & Morrison, M. J. (2017). Component and cladding wind loads for low-Slope roofs on low-rise buildings. *Journal of Structural Engineering*. (under review).
- Kopp, G. A. (2014). Wind loads on low-profile, tilted, solar arrays placed on large, flat, low-rise building roofs. *Journal of Structural Engineering*, 140, 2–11.
- Krishna, P. (1995). Wind loads on low rise buildings - A review. *Journal of Wind Engineering and Industrial Aerodynamics*, 54/55, 383-396.
- Lee, K. H., & Rosowsky, D. V. (2005). Fragility assessment for roof sheathing failure in high wind regions. *Engineering Structures*, 27, 857–868.
- Levitan, M. L., & Mehta, K. C. (1992a). Texas Tech field experiments for wind loads part 1: building and pressure measuring system. *Journal of Wind Engineering and*

Industrial Aerodynamics, 43(1), 1565–1576.

- Levitan, M. L., & Mehta, K. C. (1992b). Texas tech field experiments for wind loads part II: meteorological instrumentation and terrain parameters. *Journal of Wind Engineering and Industrial Aerodynamics*, 43(1–3), 1577–1588.
- Lieblein, J. (1974). Efficient Methods of Extreme-Value Methodology. NBSIR 74-602, Washington D.C., 1–24.
- Lin, J. X., Surry, D., & Tieleman, H. W. (1995). The distribution of pressure near roof corners of flat roof low buildings. *Journal of Wind Engineering and Industrial Aerodynamics*, 56(2–3), 235–265.
- Mahmood, M. (2011). Experiments to study turbulence and flow past a low-rise building at oblique incidence. *Journal of Wind Engineering and Industrial Aerodynamics*, 99(5), 560–572.
- Melbourne, W. (1979). Turbulence effects on maximum surface pressures—a mechanism and possibility of reduction. *Proceedings of the Fifth International Conference on Wind Engineering*. Fort Collins, CO, 541-551.
- Minor, J. E. (1994). Windborne debris and the building envelope. *Journal of Wind Engineering and Industrial Aerodynamics*, 53, 207–227.
- Pratt, R. N., & Kopp, G. A. (2014). Velocity field measurements above the roof of a low-rise building during peak suctions. *Journal of Wind Engineering and Industrial Aerodynamics*, 133, 234–241.
- Quiroga Diaz, P. S. (2006). Uncertainty analysis of surface pressure measurements on low-rise buildings. Master's Thesis, The University of Western Ontario, Canada.
- Richards, P. J., & Hoxey, R. P. (2008). Wind loads on the roof of a 6 m cube. *Journal of Wind Engineering and Industrial Aerodynamics*, 96(6–7), 984–993.
- Saathoff, P. J., & Melbourne, W. H. (1989). The generation of peak pressures in separated/reattaching flows. *Journal of Wind Engineering and Industrial Aerodynamics*, 32(1–2), 121–134.
- Saathoff, P. J., & Melbourne, W. H. (1997). Effects of free-stream turbulence on surface pressure fluctuations in a separation bubble. *Journal of Fluid Mechanics*, 337, 1–24.
- SEAOC. (2012). Wind loads on low-profile solar photovoltaic arrays on flat roofs. SEAOC-PV2. Structural Engineers Association of California, Sacramento, California.
- St. Pierre, L. M., Kopp, G. A., Surry, D., & Ho, T. C. E. (2005). The UWO contribution to the NIST aerodynamic database for wind loads on low buildings: Part 2. Comparison of data with wind load provisions, *Journal of Wind Engineering and*

Industrial Aerodynamics, 93 (2), 31-59.

Tieleman, H. W. (2003). Wind tunnel simulation of wind loading on low-rise structures: A review. *Journal of Wind Engineering and Industrial Aerodynamics*, 91(12-15), 1627-1649.

Tieleman, H. W., Ge, Z., Hajj, M. R., & Reinhold, T. A. (2003). Pressures on a surface-mounted rectangular prism under varying incident turbulence. *Journal of Wind Engineering and Industrial Aerodynamics*, 91(9), 1095-1115.

Uematsu, Y., & Isyumov, N. (1999). Wind pressures acting on low-rise buildings. *Journal of Wind Engineering and Industrial Aerodynamics*, 82, 1-25.

Uematsu, Y., Miyoshi, T., Sasaki, K., & Yamada, M. (1998). Wind damage to cladding of residential houses due to typhoon in the Tohoku District, Japan, Tohoku. *Journal of Natural Disaster Science*, 34, 155-164 (in Japanese).

Wu, C.-H., & Kopp, G. A. (2016). Estimation of wind-induced pressures on a low-rise building using quasi-steady theory. *Frontiers in Building Environment*, 2, 00005.

Appendices

Appendix A: Critical Wind Directions

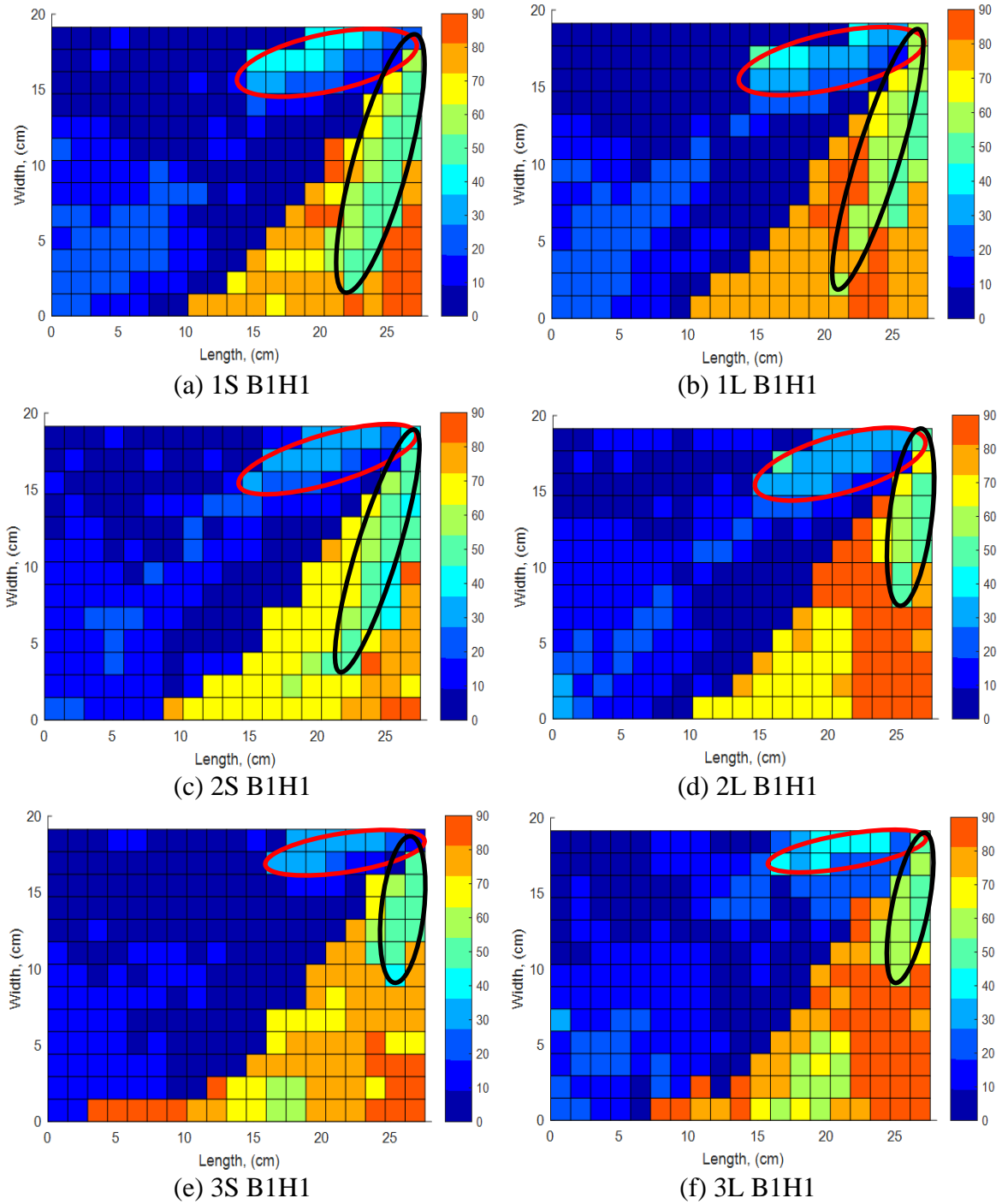


Figure A. 1: Critical wind directions over B1H1 from 0 to 90 degree.

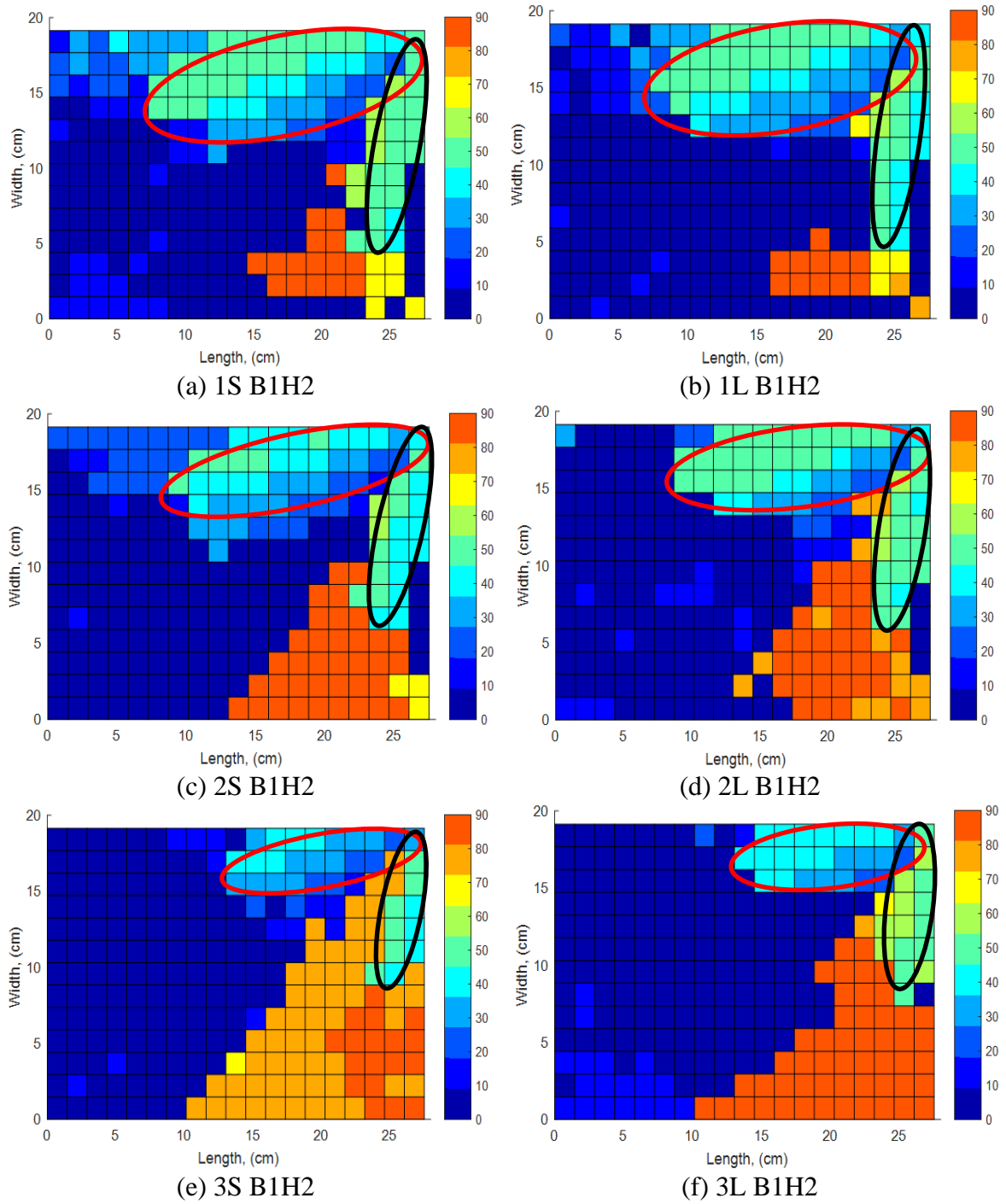


Figure A. 2: Critical wind directions over B1H2 from 0 to 90 degree.

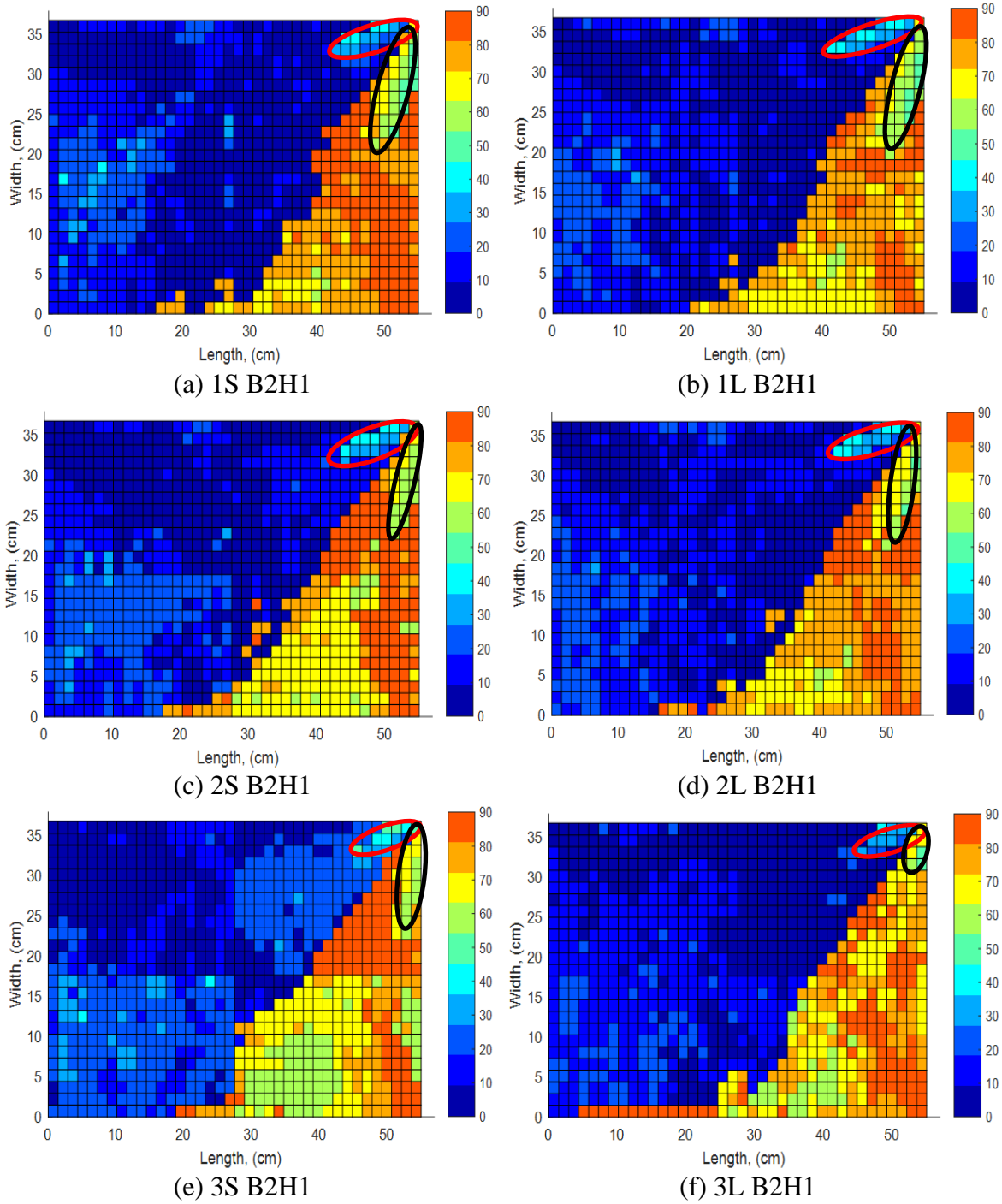


Figure A. 3: Critical wind directions over B2H1 from 0 to 90 degree.

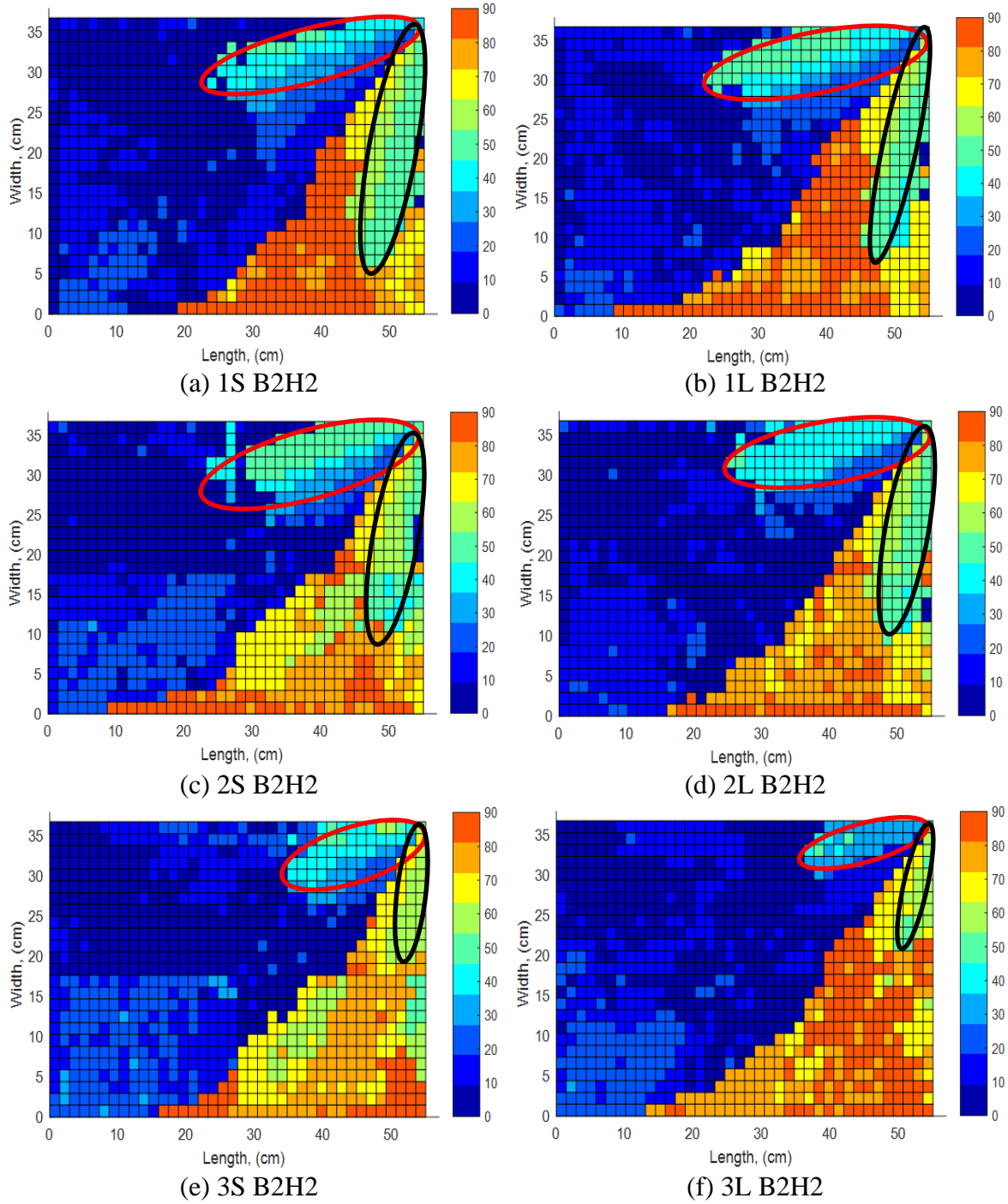


Figure A. 4: Critical wind directions over B2H2 from 0 to 90 degree.

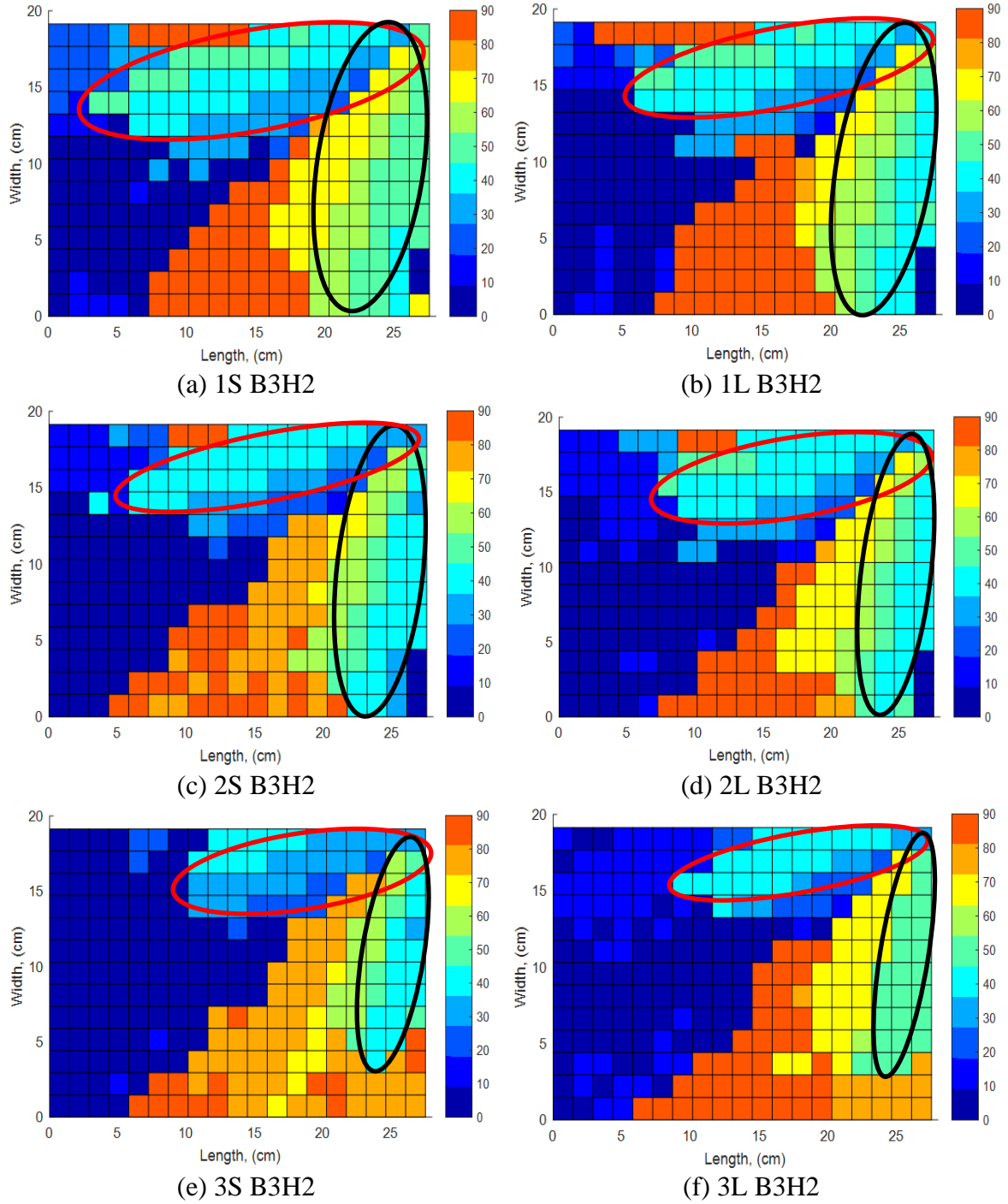


Figure A. 5: Critical wind directions over B3H2 from 0 to 90 degree.

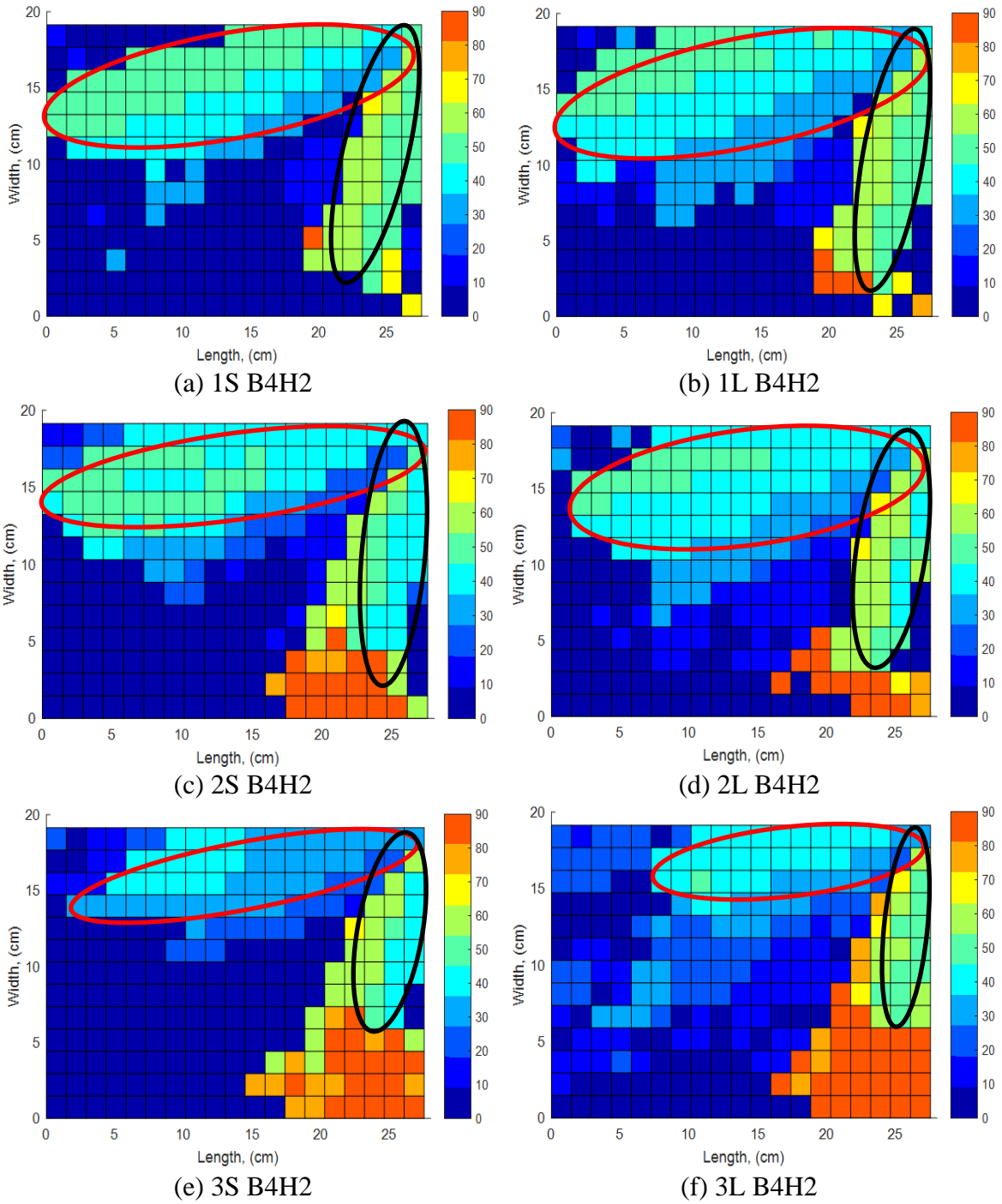


Figure A. 6: Critical wind directions over B4H2 from 0 to 90 degree.

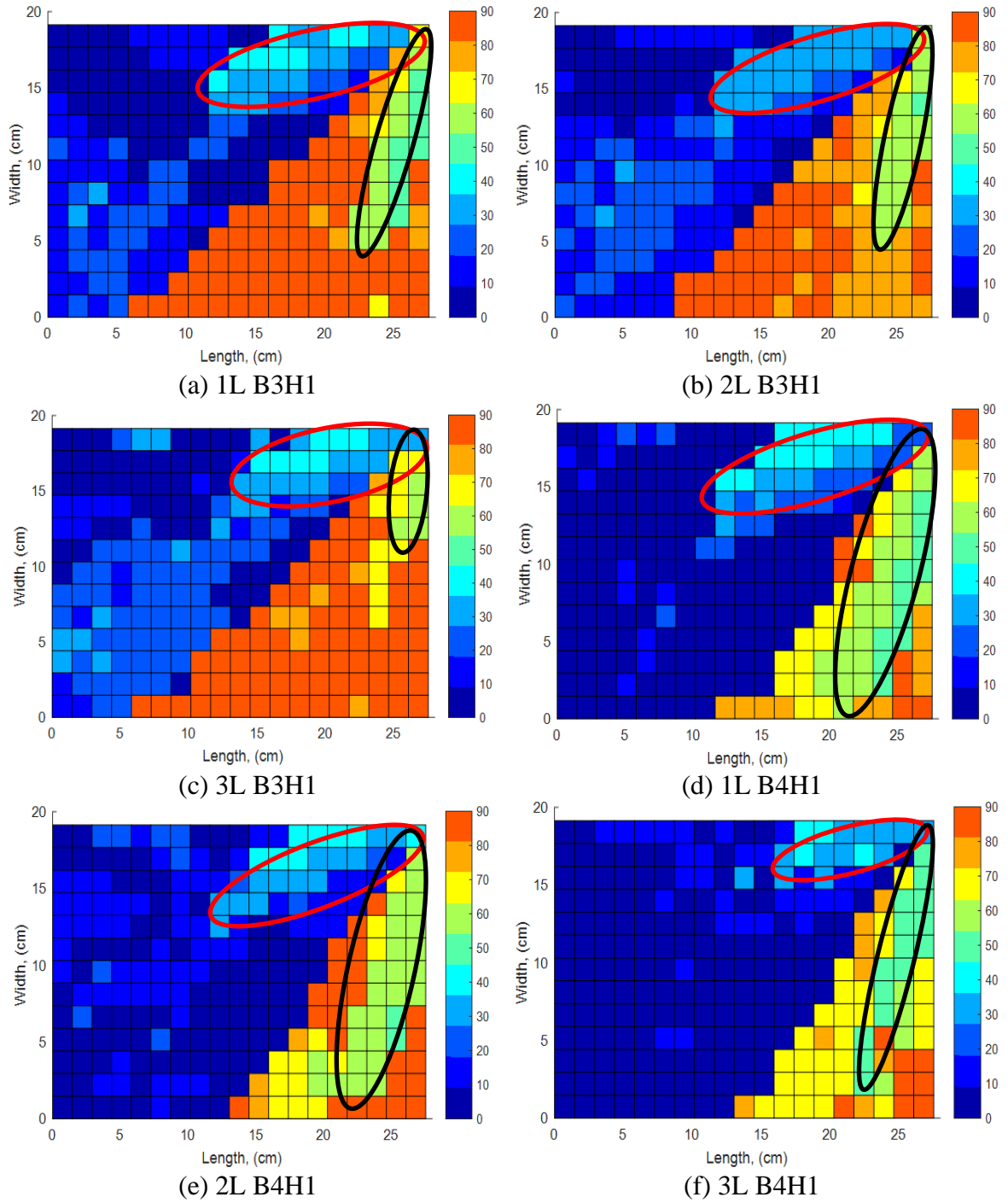
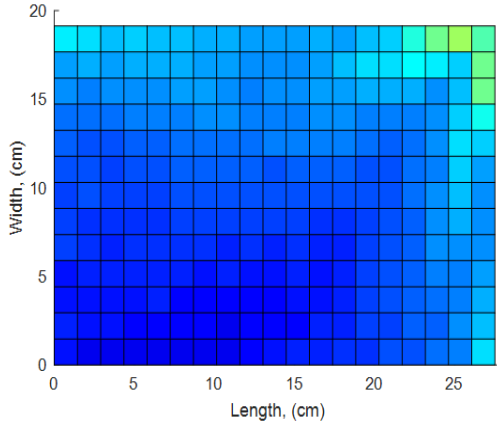
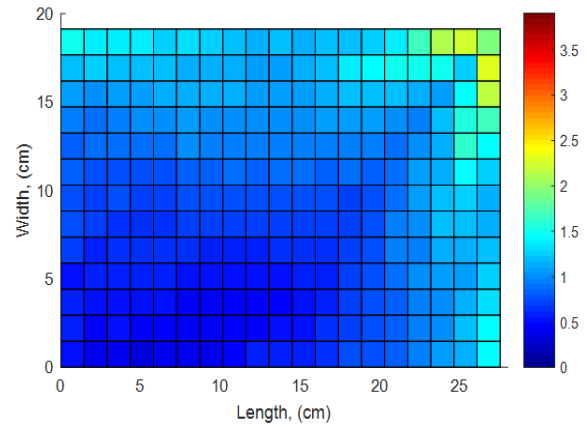


Figure A. 7: Critical wind directions over B3H1 and B4H1 from 0 to 90 degree.

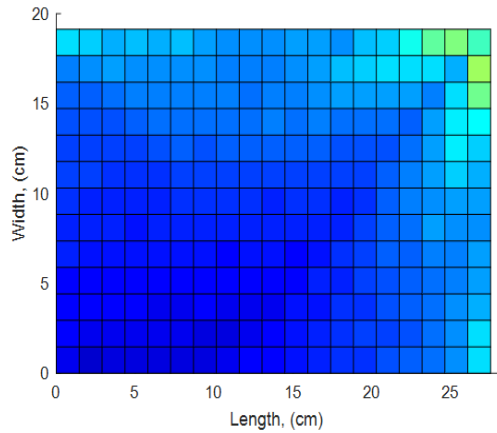
Appendix B: Worst GCp



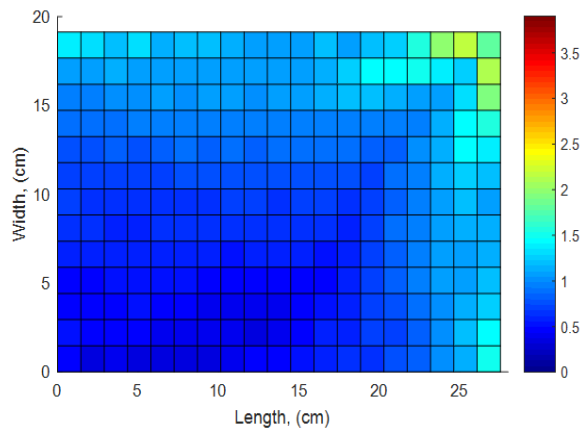
(a) 1S B1H1



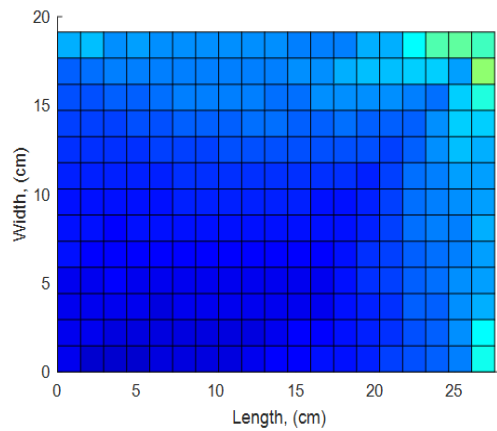
(b) 1L B1H1



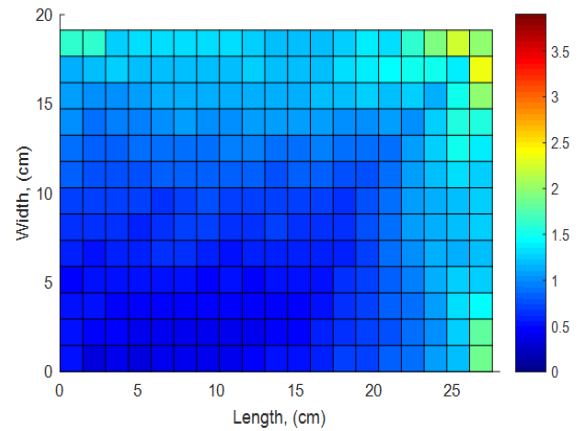
(c) 2S B1H1



(d) 2L B1H1



(e) 3S B1H1



(f) 3L B1H1

Figure B. 1: Worst Suction GCp over B1H1 from 0 to 90 degree.

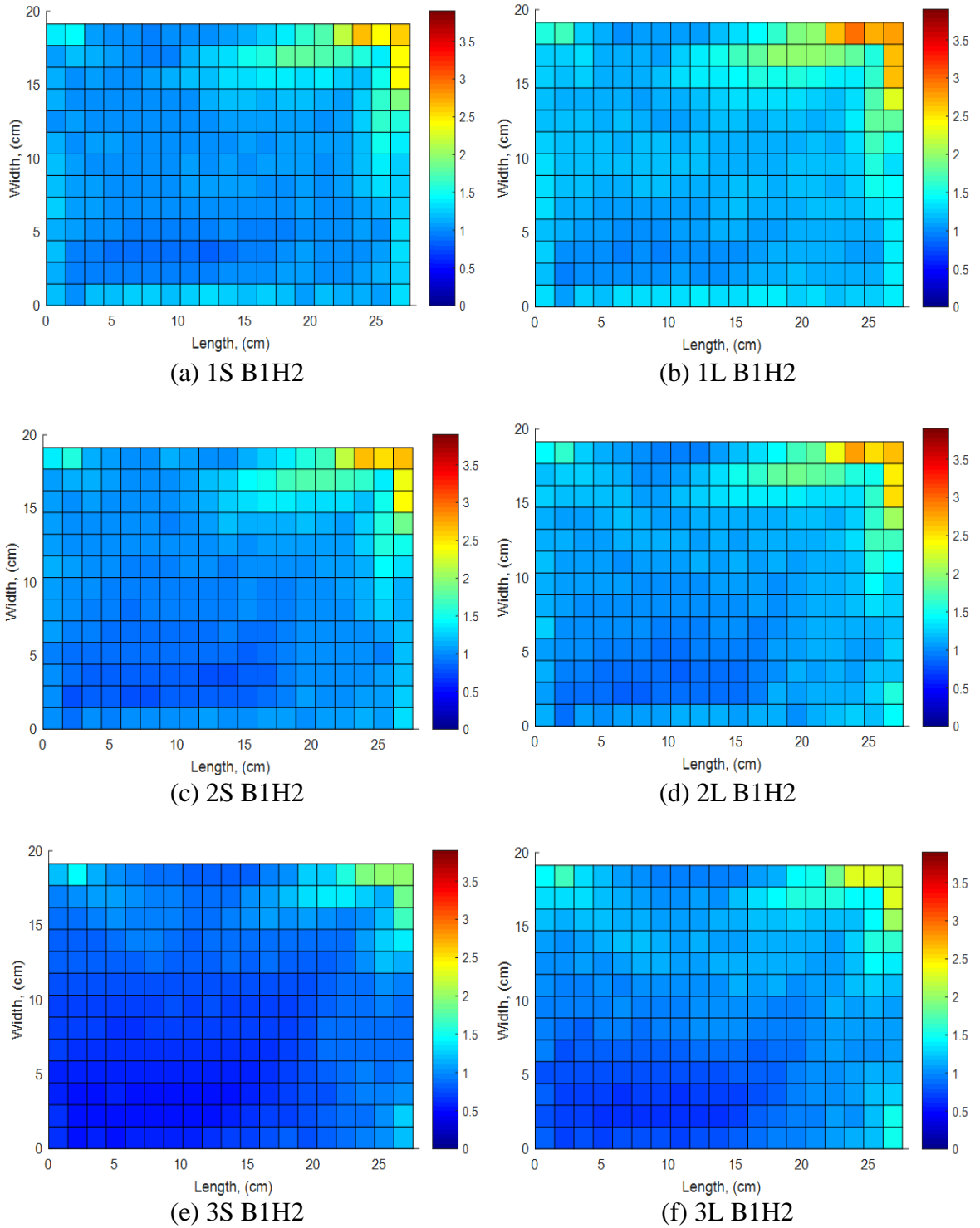


Figure B. 2: Worst Suction GcP over B1H2 from 0 to 90 degree.

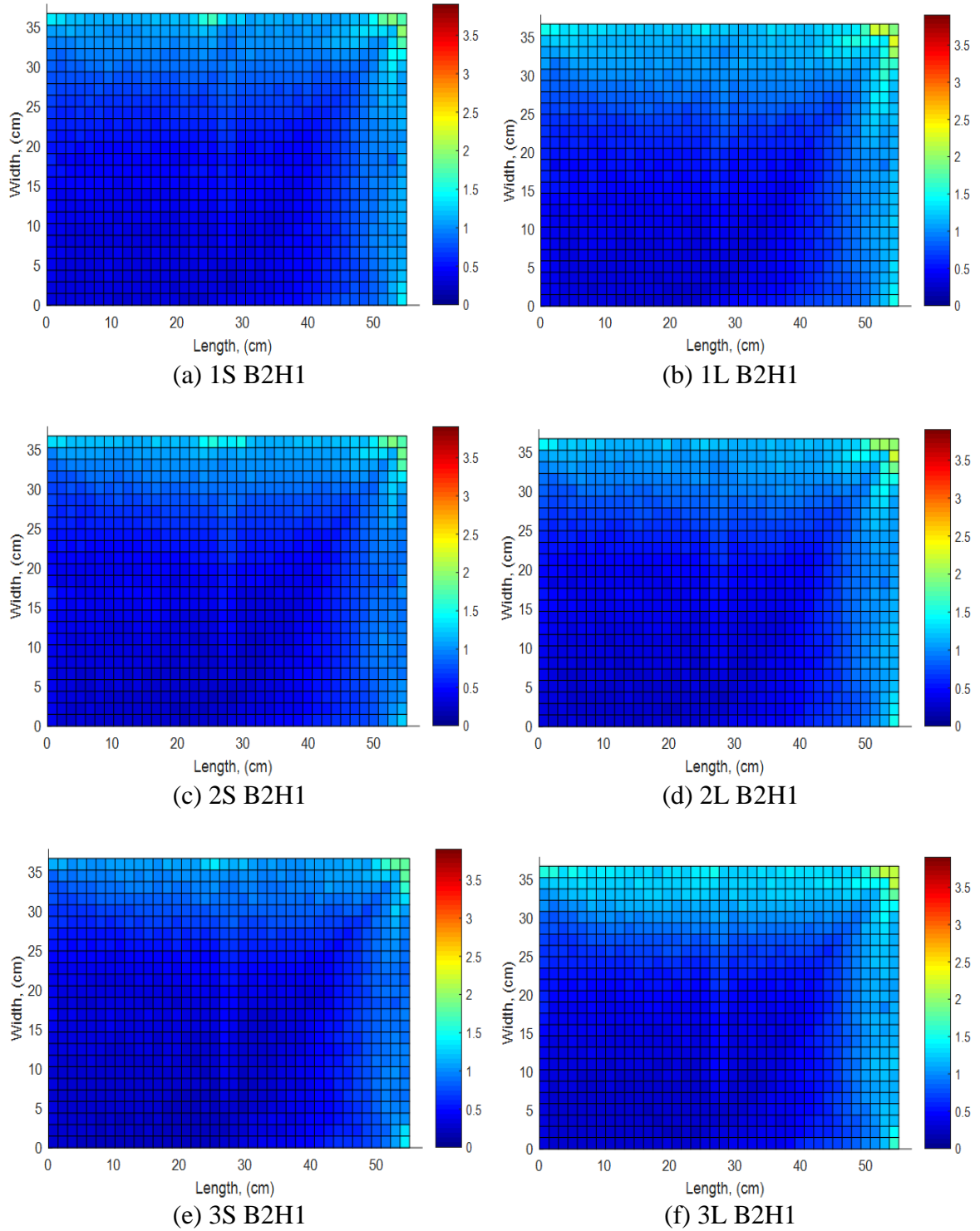


Figure B. 3: Worst Suction GcP over B2H1 from 0 to 90 degree.

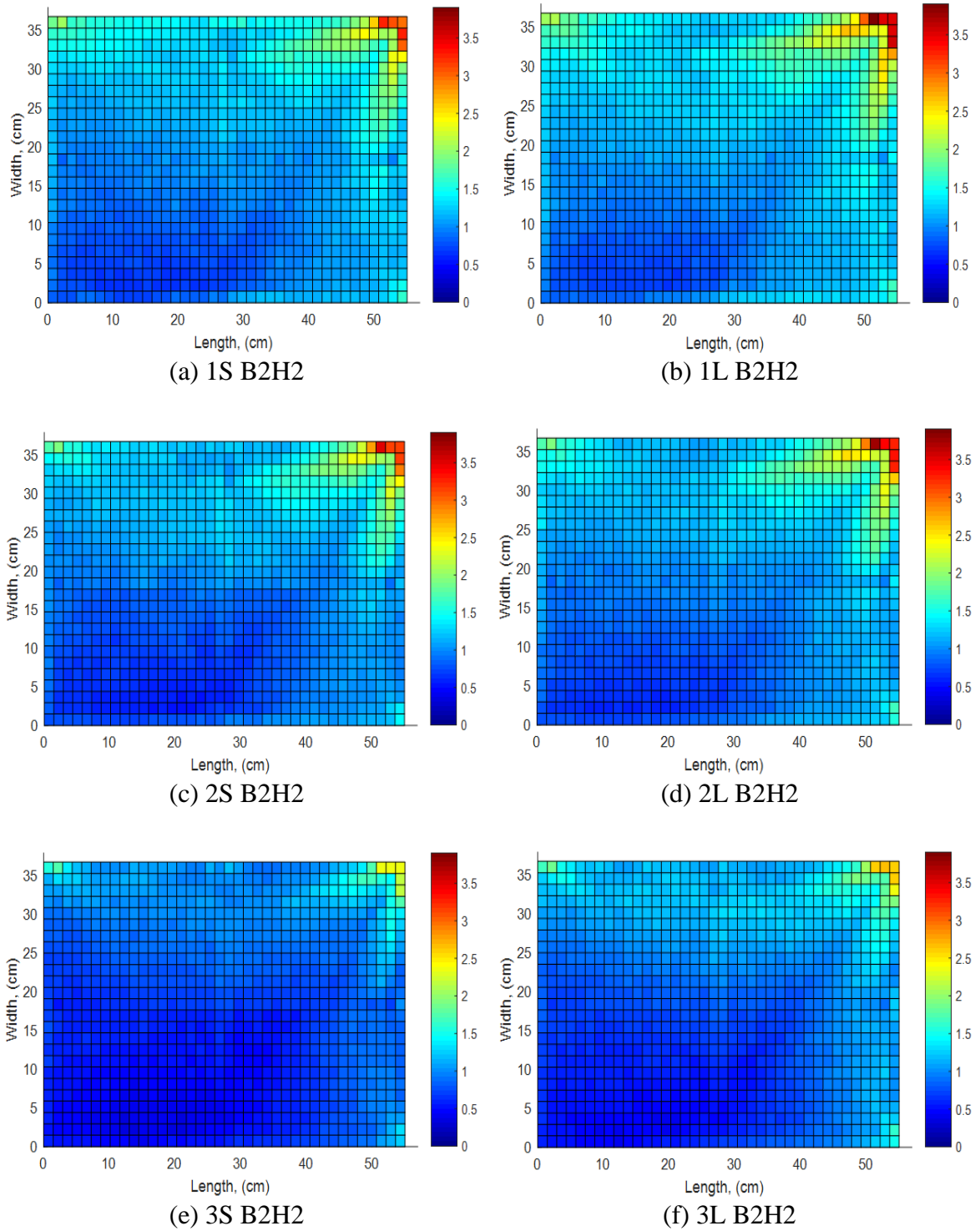


Figure B. 4: Worst Suction GcP over B2H2 from 0 to 90 degree.

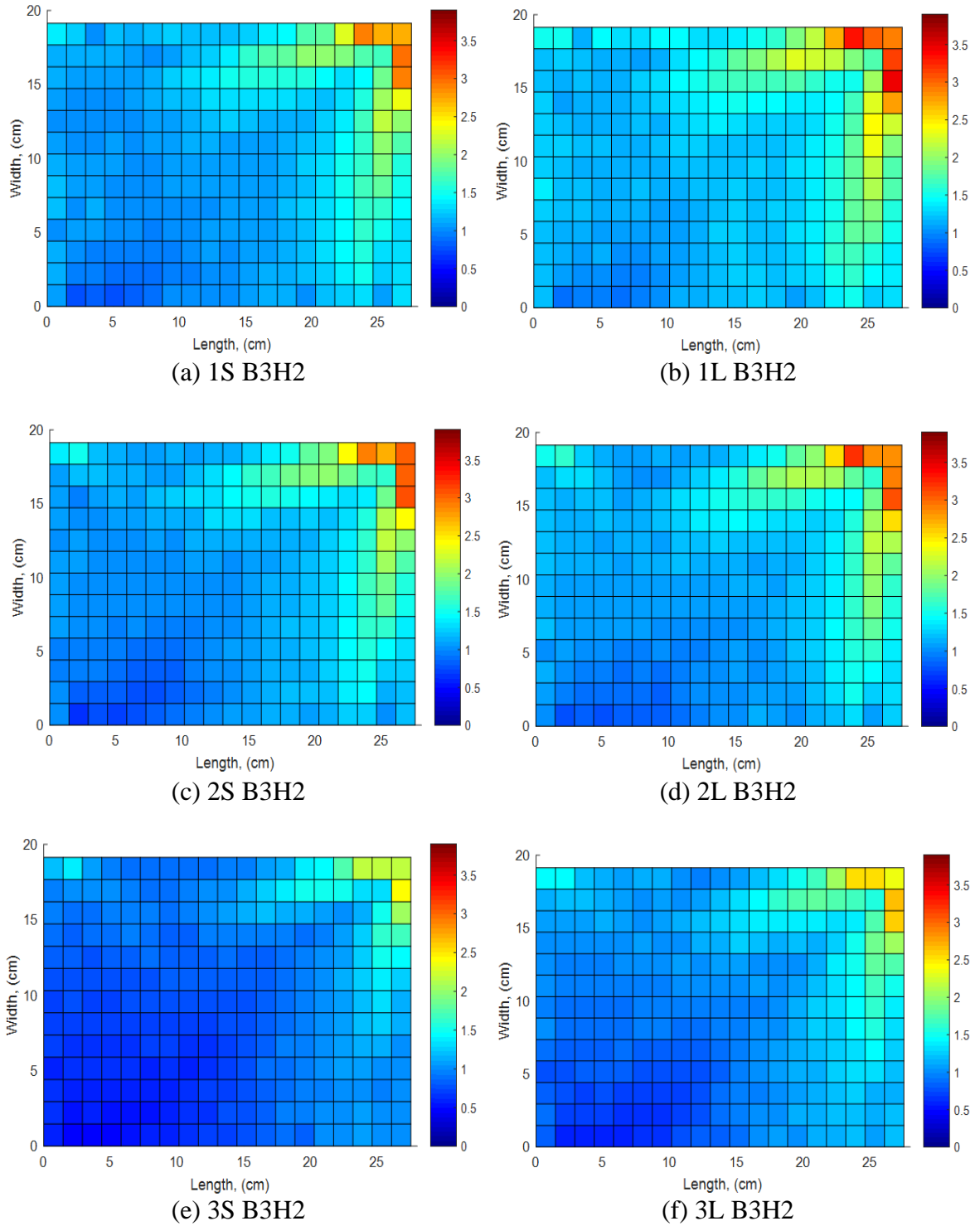


Figure B. 5: Worst Suction GcP over B3H2 from 0 to 90 degree.

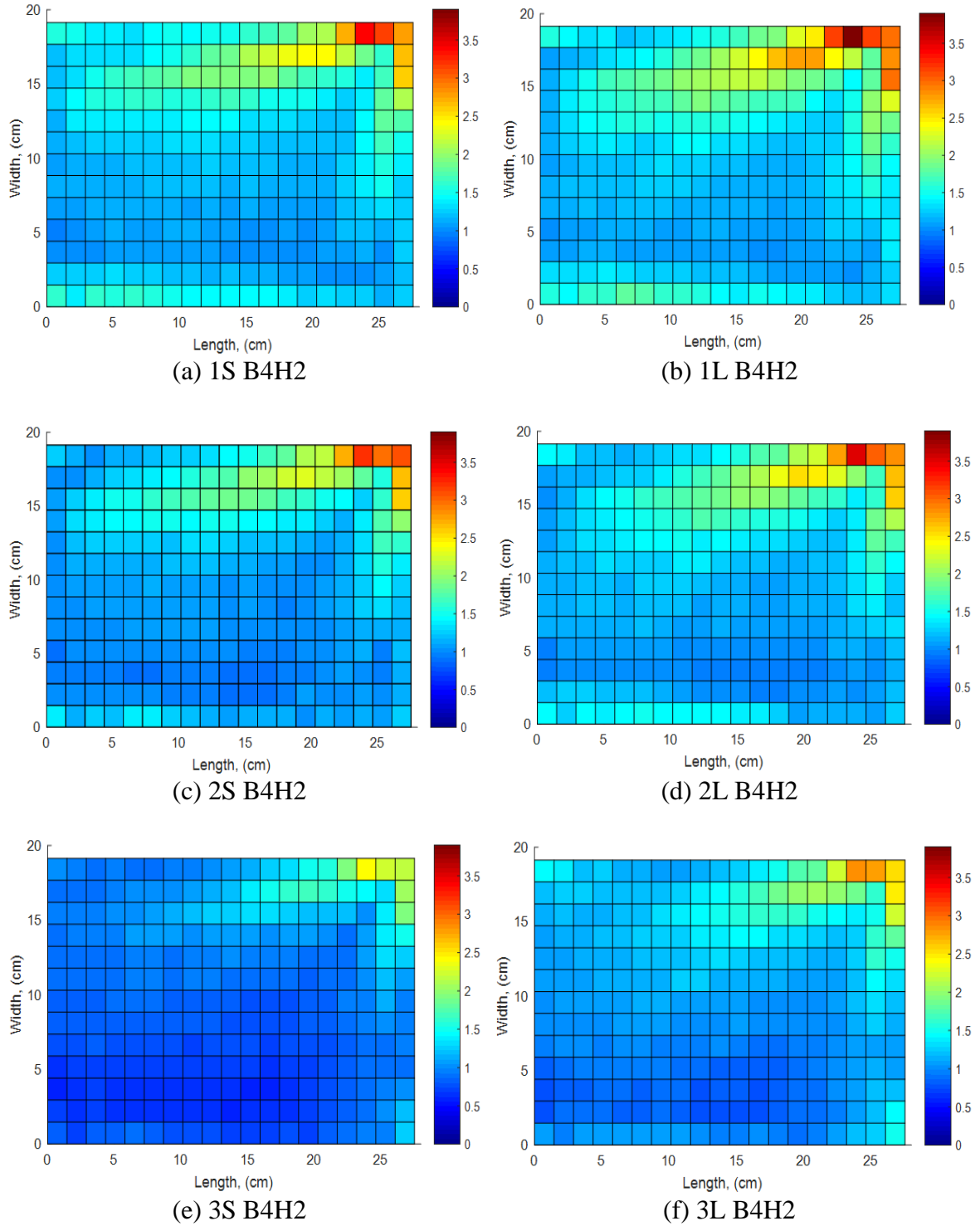
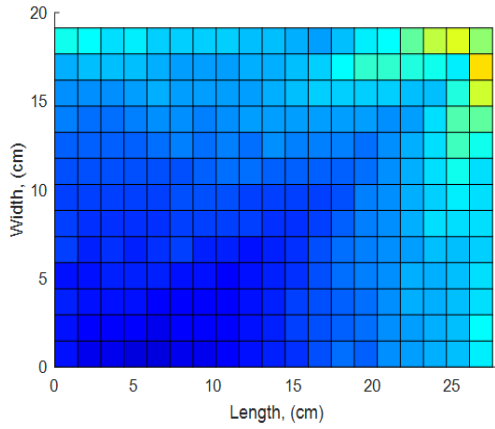
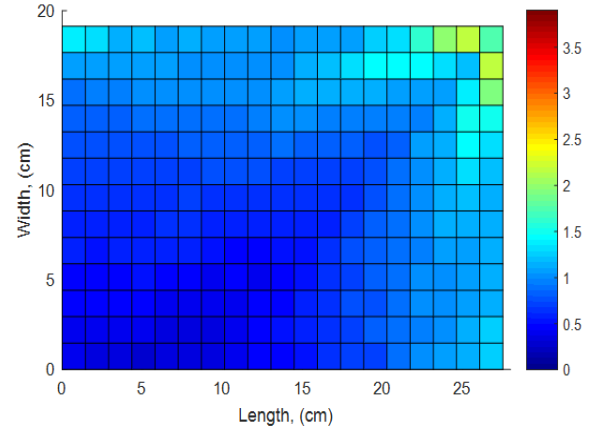


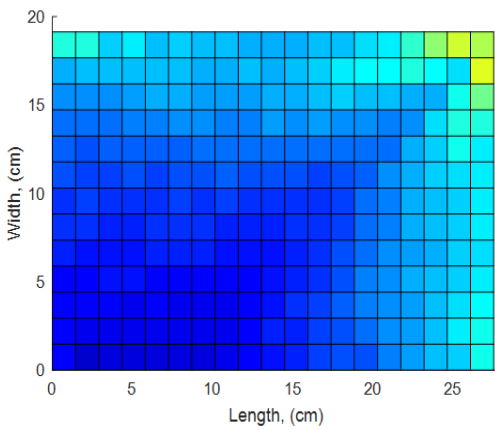
Figure B. 6: Worst Suction GcP over B4H2 from 0 to 90 degree.



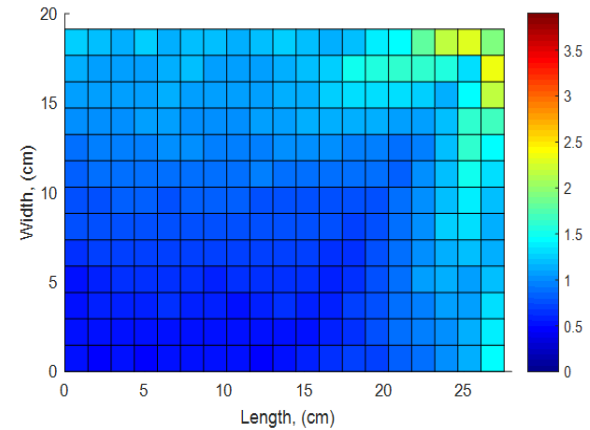
(a) 1L B3H1



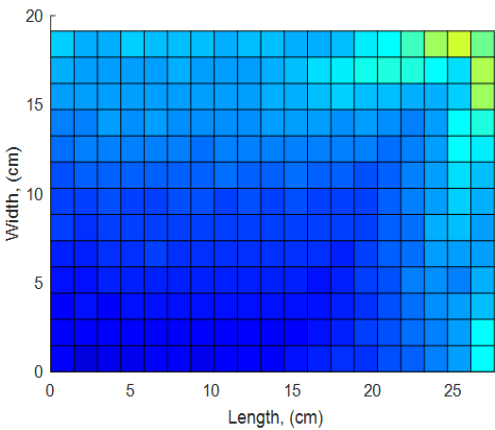
(b) 2L B3H1



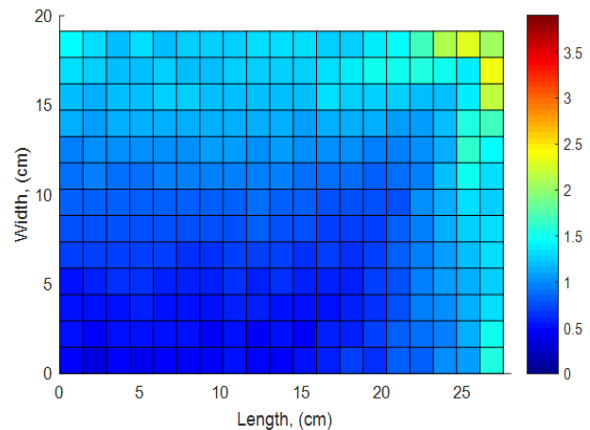
(c) 3L B3H1



(d) 1L B4H1



(e) 2L B4H1



(f) 3L B4H1

Figure B. 7: Worst Suction G_{Cp} over B3H1 and B4H1 from 0 to 90 degree.

Curriculum Vitae

Name: Fakhruzzaman Arif

Post-secondary Education and Degrees: Bangladesh University of Engineering and Technology
Dhaka, Bangladesh
2009-2014 B. Sc.

The University of Western Ontario
London, Ontario, Canada
2015-2017 M. Sc.

Honors and Awards: Bangladesh Technical Scholarship
2009-2014

Western Graduate Research Scholarship
2015-2017

Related Work Experience Teaching Assistant
University of Western Ontario
2016-2017

Research Assistant
University of Western Ontario
2015-2017

Publications:

1. Arif, F., Kopp, G. A. (2017). "Influence of terrain on the uplift loads on low-rise building roofs." *13th Americas Conference on Wind Engineering*, 2017.
2. Ismail, M. F., Arif, F., Amin, M. E., Mojumdar, J. & Sarkar, M. A. R. (2012). "Fabrication of a stair climbing vehicle for industrial and rescue application using appropriate technology." *International Conference on Electrical and Computer Engineering (ICECE)*, pp. 121-124. IEEE, 2012.
3. Arif, F., Ismail, M. F., Alam, M. S. & Sarkar, M. A. R. (2012). "Development and implementation of automated guided vehicles using locally available materials". *6th International Mechanical Engineering Conference & 14th Annual Paper Meet*, 2012.